

IMPROVING THE EFFICIENCY OF THE HYDROGEN ENGINE

by

Matthew A. Younkins

A dissertation submitted in partial fulfillment
of the requirements for the degree of
Doctor of Philosophy
(Mechanical Engineering)
in the University of Michigan
2012

Doctoral Committee:

Professor Margaret Wooldridge, Chair
Professor Claus Borgnakke
Professor Hong Im
Professor Ilya Kolmanovsky

© Matthew Younkens 2012

Acknowledgements

For the work presented here, I have had the good fortune to receive advice from and collaborate with many skilled and dedicated professionals at several facilities.

At the University of Michigan, I would of course like to thank my advisor, Margaret Wooldridge, for her support, guidance, and patience. Thank you, as well, to my dissertation committee: Claus Borgnakke, Hong Im, and Ilya Kolmanovsky; I appreciate your effort, support, and guidance.

Most of the experiments presented in this document were conducted at Ford Motor Company. First and foremost, I would like to thank Brad Boyer, my supervisor, colleague, and co-inventor. Without him the 3+3 injector would never have been designed.

Over the years, the management at Ford has been supportive of both hydrogen work and my scholarly pursuits. In particular, Eric Curtis, Thomas McCarthy, William Clay Ford, Jr., Andreas Schamel, Robert Natkin, William Stockhausen, Vance Zanardelli and John Lapetz have given support and guidance. The test department at Ford was well staffed; Erik Cross, James Larcom, Jason Cardinal, Mark Hattie, Mark Oleszkowicz, Lewis Tripp, Todd Culp, Daniel Perry, John Quoziente, Frank Wong, Curtis Potts, Joe Schim, Carl Cramer and Bob Armstrong all provided assistance and ensured the facility and engine were running appropriately.

Of course, the research was only possible with a durable, well designed fuel injector, which was provided by Westport Innovations. Many thanks go to Alan Welch, David Wager, and Charles Loo for the assistance and the superb hardware that they provided.

The optical engine work reported in Chapter 7 was conducted at Sandia National Laboratories. These experiments were done in collaboration with Victor Salazar, without whom this dissertation would be sorely lacking. Thanks also to Sebastian Kaiser, who supported the hydrogen work at that facility. The experiments conducted there were approved and supervised by Dennis Siebers and Richard Steeper. I am grateful for their help and supervision.

I would also like to thank the staff at Argonne National Laboratories for making their facility available for hydrogen engine tests. Specifically, I would like to thank Thomas Wallner, Nicholas Matthias, and Riccardo Scarcelli for their collaboration that has now stretched over many years.

I owe thanks to my family, friends, and former instructors for their assistance and patience over the past decades. Many thanks to Mick Younkins, Terry Younkins, Leah Younkins, Priya Ghose, Alex Mychkovsky, Eric Weber, Jonathan Speicher, Gary Stowasser, Bernard Vogler, Terry Nicastro, and Li-Chun Chien.

And finally, I need to thank you, the reader. I am humbled that you found this work important enough to review. I hope that someday, in the not-too-distant-future, they find a permanent cure for your chronic insomnia.

Table of Contents

Acknowledgements	ii
List of Figures	viii
List of Tables	xvi
List of Symbols and Abbreviations	xviii
Abstract	xx
Chapter 1 Introduction	1
<i>1.1 Scientific Background</i>	<i>1</i>
<i>1.2 Hydrogen Engine Studies External to Ford/University of Michigan</i>	<i>8</i>
1.2.1 Jet Development	8
1.2.2 Nozzle Pattern Development	9
1.2.3 Dilution Strategies	12
1.2.4 Vehicle-level Efficiency	14
<i>1.3 Studies at Ford Motor Company</i>	<i>15</i>
1.3.1 H ₂ DI studies not conducted by the author	15
1.3.2 H ₂ DI studies done at Ford Motor Company by the author	17
<i>1.4 Research Objectives and Summary of Dissertation</i>	<i>20</i>
Chapter 2 Experimental Setup: Metal Engine	22
<i>2.1 Dynamometer</i>	<i>22</i>

2.2 Safety Measures	23
2.3 Instrumentation	24
2.4 Hydrogen	27
2.5 Engine Design	27
2.6 Experimental Procedure	28
2.7 Mean Effective Pressure Calculations	29
2.8 Burn Rate Calculations	30
Chapter 3 Performance of Conventional PI and DI Hydrogen Engines	32
3.1 Introduction	32
3.2 PI Engine Efficiency as a Function of Engine Speed and Bore/Stroke Ratio	32
3.3 PI Engine Efficiency as a function of Compression Ratio	41
3.4 DI Engine Efficiency of as a function of Intake Manifold Pressure	47
3.5 Theoretical Potential for Pneumatic Recovery in a DI Hydrogen Engine	51
3.6 Overview of the Effects of Nozzle Design on DI Engine Efficiency	54
3.7 Summary	58
Chapter 4 Direct In-cylinder Injection of Water into a PI Hydrogen Engine	60
4.1 Introduction	60
4.2 Overview of Experiments	61
4.2.1 Injectors	61
4.2.3 Experimental Procedure	64
4.3 Experimental Results	65
4.4 Analysis and Normalization	68

4.5 Conclusion	79
Chapter 5 Water Injection into the Intake Port of a DI Hydrogen Engine	81
5.1 Introduction	81
5.2 Experimental Approach	82
5.3 Experimental Results: Fuel Consumption and NO _x Emissions	84
5.4 Analysis of Fuel Consumption/NO _x /IMEP Compromise	87
5.5 Conclusion	92
Chapter 6 Dual Zone Combustion System: Metal Engine Experimental Results	94
6.1 Introduction	94
6.2 Experimental Setup	94
6.3 Experimental Results and Discussion	96
6.3.1 Comparison of 5H and 3+3H Injectors operated with central ignition and dual-side-ignition spark plugs for fixed engine speed	96
6.3.2 Effects of Engine Speed and Fuel Injector Orientation	109
6.4 Summary and Conclusions	114
Chapter 7 Optical Characterization of Fuel Distribution in the Dual Zone Combustion System	116
7.1 Introduction	116
7.2 Optical Engine Experimental Setup	116
7.2.1 Engine Hardware	117
7.2.2 Fuel Distribution Characterization	119
7.2.3 Imaging Procedure	123
7.3 Test Matrix	124

<i>7.4 Experimental Results</i>	127
7.4.1 Injection Direction (β) = 0°	127
7.4.2 Injection Direction (β) = 90°	133
7.4.3 Comparison of Fuel Distribution at Best Ignition Timing	137
7.4.4 Fuel Penetration	138
7.4.5 Vertical Imaging: β = 0° and β = 90°	140
7.4.6 RMS and Mean Molar Fraction, Highest Horizontal Plane	145
7.4.7 RMS and Mean Mole Fraction near the ignition location	147
7.4.8 Repeatability	151
<i>7.5 Conclusions</i>	152
Chapter 8 Summary, Conclusions, and Future Work	155
<i>8.1 Summary</i>	155
<i>8.2 Conclusions</i>	156
<i>8.3 Future Work</i>	159
Appendix A Injectors/Combustion Chamber/Tests Conducted Matrix	162
Bibliography	168

List of Figures

Figure 1.1: Comparison of laminar flame speeds of hydrogen, methane, and iso-octane as a function of lambda. _____	3
Figure 1.2: Laminar flame speed and laminar burning flux for hydrogen as a function of pressure and equivalence ratio. _____	4
Figure 1.3: Laminar flame speed and adiabatic flame temperature for hydrogen as a function of equivalence ratio at atmospheric pressure. _____	5
Figure 1.4: Minimum ignition energy for hydrogen, methane, and heptane mixtures as a function of equivalence ratio at atmospheric pressure. _____	7
Figure 1.5: Change in Flammability Limits for H ₂ and Air with Respect to Temperature at 1 atm. _____	7
Figure 1.6: Four Nozzles Tested by Kim et al. _____	9
Figure 1.7: Two nozzle tested by Wallner et al. _____	10
Figure 1.8: Single nozzle injector tested by Wallner et al. _____	11
Figure 1.9: Four Injectors tested by Wallner, et al. and Matthias, et al. _____	11
Figure 1.10: Typical NMEP, ISFC, NO _x , H ₂ , and pressure rise rate performance of an unthrottled PI engine at 3000 RPM (work conducted as part of this dissertation study). _____	13
Figure 1.11. Comparison of projected H ₂ DI IC engine fuel consumption with H ₂ PEM fuel cell consumption. _____	15
Figure 2.1: The H ₂ IC engine dynamometer test cell at Ford Motor Company used for this study. _____	23

Figure 2.2: Net IMEP change resulting from a change in crankshaft angle determination of ± 1 degree, shown as a function of maximum pressure rise rate in the cycle.	26
Figure 3.1: Gross ITE as a function of equivalence ratio for several engine speeds and two crankshaft strokes.	34
Figure 3.2: Net ITE as a function of equivalence ratio for several engines speeds and two crankshaft strokes.	35
Figure 3.3: Comparison of gross and net indicated thermal efficiency as a function of engine speed for $\Phi = 0.4$.	35
Figure 3.4: Burn duration as a function of equivalence ratio.	36
Figure 3.5: Increase in coolant temperature as a function of equivalence ratio.	37
Figure 3.6: PMEP as a function of equivalence ratio.	38
Figure 3.7: Total mass flow rate into engine as a function of equivalence ratio.	38
Figure 3.8: PMEP as a function of total mass flow rate into engine.	39
Figure 3.9: FMEP as a function of equivalence ratio.	39
Figure 3.10: NO_x as a function of equivalence ratio.	40
Figure 3.11: Efficiency of theoretical Otto-cycle engine with varying equivalence ratios and compression ratios.	41
Figure 3.12: Comparison of ideal and actual data for thermal efficiency gains with increasing compression ratio as a function of equivalence ratio.	43
Figure 3.13: Crank angle of 50% burn as a function of equivalence ratio.	44
Figure 3.14: 10-90% burn duration as a function of equivalence ratio.	44
Figure 3.15: Gross and Net Indicated Thermal Efficiency as a function of Equivalence Ratio.	45
Figure 3.16: Brake thermal efficiency as a function of equivalence ratio.	46
Figure 3. 17: FMEP as a function of equivalence ratio.	46
Figure 3.18: Pressure schedule used in boosting studies of DI hydrogen engine.	48
Figure 3.19: Gross and net ITE as a function of IMEP.	49

Figure 3.20: Burn duration as a function of IMEP. _____	50
Figure 3.21: Peak pressure as a function of IMEP. _____	50
Figure 3.22: pV diagrams for theoretical constant volume combustion with direct injection of hydrogen at different injection timings. _____	52
Figure 3.23: Efficiency of a modified fuel-air Otto-cycle that accounts for post-IVC injection of hydrogen fuel. _____	53
Figure 3.24: Net ITE as a function of start of injection for different H ₂ fuel injector designs. _____	56
Figure 3.25: Net ITE as a function of piston distance from TDC for different H ₂ fuel injector designs. _____	56
Figure 3.26: Combustion stability as a function of injection timing. _____	57
Figure 4.1: Efficiency tradeoff for PI H ₂ operation: no water injection. _____	63
Figure 4.2: NO _x produced during PI H ₂ operation: no water injection. _____	63
Figure 4.3: Net IMEP as a function of Equivalence Ratio: no water injection. _____	64
Figure 4.4: NO _x production and net indicated specific fuel consumption as a function of water injection timing. _____	66
Figure 4.5: Net ITE as a function of H ₂ O injection angle. _____	66
Figure 4.6: CA50 as a function of water injection timing. _____	67
Figure 4.7: Burn duration as a function of water injection timing. _____	67
Figure 4.8: Net ITE vs. Net IMEP, comparison of Water Injection and Non-Water Injection. _____	68
Figure 4.9: NO _x emissions as a function of IMEP for water injection conditions and baseline conditions with no water injection (labeled Phi Sweep). _____	69
Figure 4.10: NO _x as a function of IMEP for conditions without the use of water injection (logarithmic scale). Symbols are experimental data. Solid line is the fit of Equation 4.1. _____	70

Figure 4.9: NO _x as a function of IMEP for conditions without the use of water injection (linear scale). Symbols are experimental data. Solid line is the fit of Equation 4.1. ___	70
Figure 4.12: Predicted and Actual NO _x levels, with and without water injection. ____	71
Figure 4.13: Net ISFC as a function of Net IMEP. _____	72
Figure 4.14: Estimated effects of water injection on NO _x and fuel consumption. ____	73
Figure 4.15: Normalized fuel consumption as a function of injection timing. ____	73
Figure 4.16: Normalized NO _x as a function of injection timing. _____	74
Figure 4.17: Peak pressure as a function of water injection phasing. _____	75
Figure 4.18: Timing of peak pressure (relative to TDC = 0°) as a function of water injection phasing. _____	76
Figure 4.19: Peak pressure as a function of net IMEP. _____	77
Figure 4.20: Time in CAD of peak pressure as a function of net IMEP. _____	77
Figure 4.21: Pressure as a function of crank angle. _____	78
Figure 4.22: pV Diagram. _____	79
Figure 5.1: Tradeoff between NO _x and ISFC for $\phi = 0.6$ single and split injection strategies. _____	83
Figure 5.2: NO _x as a function of ISFC for PI water injection and DI H ₂ injection. ____	85
Figure 5.3: NO _x as a function of ISFC, fixed injection time. _____	85
Figure 5.4: Tradeoff between NO _x and ISFC, summary of best points among all points tested. _____	86
Figure 5.5: Comparison of NO _x production as a function of IMEP for water injection and baseline (no water injection) conditions. _____	88
Figure 5.6: Comparison of ISFC as a function of IMEP for water injection and baseline (no water injection) conditions. _____	89
Figure 5.7: Normalized NO _x mitigation as a function of fuel consumption penalty. ____	90
Figure 5.8: Peak pressure as a function of IMEP. _____	91
Figure 5.9: Maximum pressure rise rate as a function of IMEP. _____	92

Figure 6.1: Indicated specific fuel consumption and NO _x emissions as a function of SOI.	96
Figure 6.2: NO _x production as a function of fuel consumption for the different cylinder head and fuel injector combinations.	99
Figure 6.3: 10-90% burn duration as a function of end of injection timing for the different cylinder head and fuel injector combinations.	100
Figure 6.4: 0-10% burn duration as a function of end of injection timing for the different cylinder head and fuel injector combinations.	100
Figure 6.5: Correlation between 0-10% burn rate and efficiency; dual-side-ignition cylinder head (left) and single-central-ignition cylinder head (right).	102
Figure 6.6: Correlation between 10-90% burn rate and efficiency.	102
Figure 6.7: Combustion stability as a function of injection timing.	103
Figure 6.8: Summary of combustion statistics and NO _x production for five injection timings for the 3+3H injector with dual-side-ignition cylinder head.	104
Figure 6.9: Pressure data as a function of crank angle for the EOI timings of Figure 6.8 (listed in degrees BTDC) for the dual-side-ignition/3+3H engine configuration.	105
Figure 6.10: Pressure/volume time histories of selected EOI timings (listed in degrees BTDC) for the dual-side-ignition/3+3H engine configuration. The data correspond to the results presented in Figure 6.9.	106
Figure 6.11: Pressure/volume time histories comparing earliest injection to latest injection for the dual-side-ignition/3+3H engine configuration.	107
Figure 6.12: Comparison of pV diagrams for EOI = 120 degrees (near-homogeneous) and EOI = 60 degrees (best observed efficiency).	108
Figure 6.13: Comparison of pV diagrams for EOI = 60 degrees (best observed efficiency) and EOI = 18 degrees (highly stratified).	108
Figure 6.14: Thermal efficiency as a function of start of injection for different engine speeds and fuel injector orientations.	110

Figure 6.15: 0-10% burn duration as a function of SOI. _____	111
Figure 6.16: 10-90% burn duration as a function of SOI. _____	111
Figure 6.17: Combustion stability (COV of IMEP, % basis) as a function of SOI. _____	112
Figure 6.18: Exhaust runner temperature as a function of start of injection. _____	113
Figure 6.19: Increase in coolant temperature as a function of start of injection. _____	114
Figure 7.1: Test Engine at Sandia National Lab and Schematic, Courtesy Victor Salazar. _____	118
Figure 7.2: Injector used in experiments. _____	118
Figure 7.3: Schematic of Laser Setup for Imaging. _____	121
Figure 7.4: Test Setup Schematics and example vertical (left) and horizontal (right) images. Figure courtesy Victor Salazar. _____	121
Figure 7.5: Location of spark plugs in Dual-Side Ignition Cylinder Head. _____	122
Figure 7.6: Relative Positions of Vertical and Horizontal images. _____	123
Figure 7.7: Timeline for 2 sets of four images taken. Process was repeated until a total of 200 images were taken. _____	124
Figure 7.8: Efficiency as a function of Injection Phasing. _____	125
Figure 7.9: Equivalence Ratio as a function of Molar Fraction. _____	127
Figure 7.10: Fuel Distribution for $SOI = 90^\circ$ and $\beta = 0^\circ$, Vertical planes only. Images taken at 75, 60, 45, 30, 20, and 11 deg BTDC. MBT Timing was found to be 11° BTDC for equivalent metal engine experiment. On the metal engine, this condition was found to be a local maxima of efficiency. _____	128
Figure 7.11: Fuel Distribution for $SOI = 90^\circ$ and $\beta = 0^\circ$, vertical and horizontal planes. Images taken at 75, 60, 45, 30, 20, and 11 deg BTDC. MBT Timing was found to be 11° BTDC for equivalent metal engine experiment. On the metal engine, this condition was found to be a local maxima of efficiency. _____	129

Figure 7.12: Fuel Distribution for $SOI = 63^\circ$ and $\beta = 0^\circ$, horizontal planes only. Images taken at 60, 45, 30, 25, 20, 15, and 11 deg BTDC. MBT Timing was found to be 11° BTDC for equivalent metal engine experiment. On the metal engine, this condition was a local minima of efficiency. _____ 130

Figure 7.13: Fuel Distribution for $SOI = 63^\circ$ BTDC and $\beta = 0^\circ$, horizontal and vertical planes. Images taken at 60, 45, 30, 25, 20, 15, and 11 deg BTDC. MBT Timing was found to be 11° BTDC for equivalent metal engine experiment. On the metal engine, this condition condition was found to be a local minima of efficiency. _____ 130

Figure 7.14: Fuel Distribution for $SOI = 38^\circ$ BTDC and $\beta = 0^\circ$, horizontal planes only. Images taken at 35, 30, 25, 20, 15, 11, 4 deg BTDC and 1 deg ATDC. MBT Timing was found to be 1° ATDC for equivalent metal engine experiment. On the metal engine, this condition was found to have the highest efficiency of all points tested. _____ 131

Figure 7.15: Fuel Distribution for $SOI = 38^\circ$ BTDC and $\beta = 0^\circ$, horizontal and vertical planes. Images taken at 35, 30, 25, 20, 15, 11, 4 deg BTDC and 1 deg ATDC. MBT Timing was found to be 1° ATDC for equivalent metal engine experiment. On the metal engine, this condition was found to have the highest efficiency of all points tested. _____ 131

Figure 7.16: Fuel Distribution for $SOI = 28^\circ$ BTDC and $\beta = 0^\circ$, horizontal planes only. Images taken at 25, 20, 15, 11, 4 deg BTDC and 1 deg ATDC. MBT Timing was found to be 1° ATDC for equivalent metal engine experiment. On the metal engine, this condition was found to have poor efficiency. _____ 132

Figure 7.17: Fuel Distribution for $SOI = 28^\circ$ BTDC and $\beta = 0^\circ$, horizontal and vertical planes. Images taken at 25, 20, 15, 11, 4 deg BTDC and 1 deg ATDC. MBT Timing was found to be 1° ATDC for equivalent metal engine experiment. On the metal engine, this condition was found to have poor efficiency. _____ 132

Figure 7.18: Fuel Distribution for $SOI = 90^\circ$ BTDC and $\beta = 90^\circ$, horizontal planes only. Images taken at 75, 60, 45, 30, 20 and 11 deg BTDC. Metal engine testing completed outside the scope of this work indicated this point would be less efficient than $SOI = 63^\circ$. _____ 133

Figure 7.19: Fuel Distribution for $\text{SOI} = 90^\circ$ BTDC and $\beta = 90^\circ$, horizontal planes only. Images taken at 75, 60, 45, 30, 20 and 11 deg BTDC. Metal engine testing done outside the scope of this work indicated this point would be less efficient than $\text{SOI} = 63^\circ$. _____	134
Figure 7.20: Fuel Distribution for $\text{SOI} = 63^\circ$ BTDC and $\beta = 90^\circ$, horizontal planes only. Images taken at 60, 45, 30, 20 and 11 deg BTDC. Metal engine testing done outside the scope of this work indicated this condition is close to the peak efficiency point of $\text{SOI} = 70^\circ$. _____	135
Figure 7.21: Fuel Distribution for $\text{SOI} = 63^\circ$ BTDC and $\beta = 90^\circ$, horizontal and vertical planes. Images taken at 60, 45, 30, 20 and 11 deg BTDC. Metal engine testing done outside the scope of this work indicated this condition is close to the peak efficiency point of $\text{SOI} = 70^\circ$. _____	136
Figure 7.22: Fuel Distribution for $\text{SOI} = 38^\circ$ BTDC and $\beta = 90^\circ$, horizontal planes only. Images taken at 35, 30, 25, 20, 15, 11, and 4 deg BTDC. Metal engine testing done outside the scope of this work indicated this condition has poor efficiency. _____	136
Figure 7.23: Fuel Distribution for $\text{SOI} = 38^\circ$ BTDC and $\beta = 90^\circ$, horizontal and vertical planes. Images taken at 35, 30, 25, 20, 15, 11, and 4 deg BTDC. Metal engine testing done outside the scope of this work indicated this condition has poor efficiency. _____	136
Figure 7.24: Fuel distribution for different injection timing (SOI) and best ignition timing (ST), $\beta = 0^\circ$. _____	137
Figure 7.25: Fuel Distribution at best ignition timing, $\beta = 90^\circ$. _____	138
Figure 7.26: Fuel Distribution Immediately following Injection, Four Injection Timings. _____	139
<hr/>	
Figure A.1: Injectors/Combustion Chamber/Tests Conducted, part 1. _____	162
Figure A.2: Injectors/Combustion Chamber/Tests Conducted, part 2. _____	163
Figure A.3: Injectors/Combustion Chamber/Tests Conducted, part 3. _____	165
Figure A.4: Injectors/Combustion Chamber/Tests Conducted, part 4. _____	166
Figure A.5: Injectors/Combustion Chamber/Tests Conducted, part 5. _____	167

List of Tables

Table 1.1: Comparison of the combustion properties of hydrogen, methane and iso-octane _____	6
Table 1.2: Various cylinder heads tested at Ford _____	16
Table 1.3: Various pistons tested at Ford _____	16
Table 1.4: Various injectors tested at Ford _____	17
Table 2.1: H ₂ IC engine instrumentation. _____	24
Table 2.2: Engine dimensions and specifications _____	28
Table 3.1: Engine Design and Operating Parameters for PI Engine Speed and Stroke Studies _____	33
Table 3.2: Engine Design and Operating Parameters for PI Compression Ratio Studies	42
Table 3.3: Engine Design and Operating Parameters for DI Boosting Studies _____	47
Table 3.4: Engine design and operating parameters for DI studies of the effects of hydrogen injector nozzle design _____	54
Table 3.5: Key Features of the Fuel Injector Nozzles Tested _____	55
Table 4.1: Fuel and Water Injectors Used _____	62
Table 5.1: Fuel and Water Injection Hardware _____	82
Table 5.2: Water Injection Parameters used _____	84

Table 6.1: Cylinder heads and injectors tested _____	95
Table 6.2: Fuel injector nozzle designs tested _____	95
Table 7.1: Comparison of Metal Engine and Optical Engine _____	117
Table 7.2: Comparison of Possible Fuel Tracers[19] _____	119
Table 7.3: Matrix of Tests Conducted for optical imaging studies _____	126

List of Symbols and Abbreviations

β	Injector orientation angle
ϕ	Equivalence Ratio
ATDC	After Top Dead Center
ANL	Argonne National Laboratory
BMEP	Brake Mean Effective Pressure
BP	BackPressure
B/S	Bore to Stroke ratio
BTDC	Before Top Dead Center
BTE	Brake Thermal Efficiency
CA50	Crank Angle at which 50% of mass fraction is burned
CFD	Computational Fluid Dynamics
COV	Coefficient Of Variation
DI	Direct Injection
EGR	Exhaust Gas Residual
EOI	End of Injection
ER	Expansion Ratio

FMEP	Friction Mean Effective Pressure
GIMEP or IMEP ₃₆₀	Gross Indicated Mean Effective Pressure
IC	Internal Combustion
LES	Large Eddy Simulation
LHV	Lower Heating Value
MFB	Mass Fraction Burned
NMEP or IMEP ₇₂₀	Net Indicated Mean Effective Pressure
NO _x	Nitrogen Oxides
PI	Port Injection
PIV	Particle Image Velocimetry
PLIF	Planar Laser Induced Fluorescence
PMEP	Pumping Mean Effective Pressure
pV	Pressure-Volume
RANS	Reynolds Averaged Navier-Stokes
RON	Research Octane Number
SNL	Sandia National Laboratory
SOI	Start of Injection
STP	Standard Temperature and Pressure
TDC	Top Dead Center

Abstract

Internal combustion (IC) engines fueled by hydrogen are among the most efficient means of converting chemical energy to mechanical work. The exhaust has near-zero carbon-based emissions, and the engines can be operated in a manner in which pollutants are minimal. In addition, hydrogen engines have potential for efficiencies higher than fuel cells and are likely to have a small increase in engine costs compared to conventionally fueled engines. However, there are challenges to using hydrogen in IC engines. In particular, efficient combustion of hydrogen in engines produces nitrogen oxides (NO_x) that generally cannot be treated with conventional three-way catalysts.

This work presents the results of numerous experiments which consider changes in hydrogen engine design and/or operating strategy to improve engine performance, consisting primarily of engine efficiency and NO_x emissions. Several piston and cylinder head configurations were considered. Engine speeds, equivalence ratios, intake pressures, compression ratios, and injector nozzle designs were evaluated for some of the hardware configurations. A gain of 2% of lower heating value (LHV) was found in increasing stroke from 79 mm to 95 mm. A gain of 1.2% of LHV was found in increasing compression ratio from 12.0 to 13.7:1. Gains of (simulated) turbocharging were found, yielding about 0.2% of LHV per bar of NMEP.

Three research areas were considered in greater detail to reduce NO_x emissions and improve hydrogen engine efficiencies. The first effort focused on injecting liquid water into the cylinder filled with a premixed fuel-air charge. The

amount of water injected was varied, as was the phasing of the water injected. The results were compared against expectations for a conventionally operated hydrogen engine. Using this approach of direct injection of water into the cylinder, NO_x emissions were reduced by 95% with an 8% fuel consumption penalty, and NO_x emissions were reduced by 85% without any fuel consumption penalty. At a threshold of 100 ppm of NO_x, peak load possible increased by 17.3%.

The second research area considered injecting water into the intake air charge. The hydrogen fuel was directly injected into the cylinder. The amount of water injected into the intake charge, the amount of fuel injected, the phasing of the fuel injection, the number of fuel injection events, and the ignition timing were all varied. Again, the results were compared with expectations for a conventionally operated hydrogen engine. With water injection into the intake air charge, the NO_x emissions were reduced by 87% with a 2% penalty in fuel consumption. At a threshold of 90 ppm of NO_x, peak load possible increased by 23.9%.

Finally, experimental data were generated and analyzed for a combustion chamber with two spark plugs. An injector was designed to preferentially stratify the fuel towards the ignition sites. Results from a metal engine and an optically accessible engine are presented. Based on the metal engine data, the new cylinder head design produced a remarkable 47.7% net indicated thermal efficiency (ITE) while producing only 51 ppm of NO_x. For the experiments conducted on the optically accessible engine, the fuel was seeded with acetone and laser induced fluorescence was used to visualize the fuel distribution during non-firing operation. The most optimal injection conditions (based on the metal engine results) showed a fuel distribution of approximately $\Phi = 0.65$ near the ignition locations.

Chapter 1

Introduction

When used in internal combustion (IC) engines, hydrogen has inherent advantages over hydrocarbon fuels – fast burn rates, low radiation losses, high knock resistance, low fuel weight, and zero fuel-based carbon emissions [1]. The fast burn rate, low radiation loss, and high knock resistance allow engine designs that have high mechanical energy output relative to fuel energy content. The low fuel mass combined with high mechanical conversion efficiency results in low brake specific fuel consumption.

However, there are several challenges that have prevented large scale usage of hydrogen in IC engines. Hydrogen is expensive compared to conventional fuels. The fuel storage occupies a large volume relative to hydrocarbon fuels. Efficient combustion of hydrogen in engines produces nitrogen oxides (NO_x) that generally cannot be treated with conventional three-way catalysts. Nevertheless, the readily available technology and high efficiency, which may be able to exceed that of fuel cells, makes hydrogen engine research a worthwhile effort[2].

The majority of hydrogen engine research conducted to date has attempted to increase engine efficiency while maintaining acceptable engine output and emissions compliance. This work focuses on the same goals.

1.1 Scientific Background

Hydrogen has properties that vary widely from conventional fuels, see for example Figure 1.1 [1]. Some of the key characteristics and differences are

shown in Table 1 [1], [3]. Of particular note are the low quench distance, wide flammability limits, extremely low ignition energy, and high diffusivity of H₂. The flammability limits, shown with respect to temperature in Figure 1.2, are generally quoted as 4-75% at standard temperature and pressure (STP), and the limits expand even further at high temperatures [3][4]. The autoignition temperature, 585 °C, is higher than most other fuels. The empirical "research octane number" (RON) is commonly reported to be greater than 130 [3].

When compared to more conventional fuels, the wide flammability limits of H₂ allow operation at leaner equivalence ratios, which can eliminate throttling losses. Specifically, IC engine operation below $\phi = 0.2$ is possible, and operation at $\phi = 0.08$ has been observed by the author in limited circumstances. Operation below $\phi = 0.2-0.3$ is problematic, however, with burn rates slowing dramatically. Figure 1.1 compares the laminar flame speeds of hydrogen, iso-octane, and methane as a function of the inverse equivalence ratio, $\lambda = 1/\phi$, in the range of $\phi = 0.5 - 1.25$ ($\lambda = 2 - 0.8$). At stoichiometric conditions, hydrogen burns over 5 times faster than the hydrocarbon fuels. At lean conditions, $\lambda = 2$ ($\phi = 0.5$), the H₂ flame speed is still 50% faster than iso-octane at stoichiometric conditions. The fast laminar flame speed can mitigate losses due to combustion delays. Since low global equivalence ratios will reduce pumping losses, and high local equivalence ratios will reduce combustion losses, a good combustion system design will target relatively-rich pockets of fuel localized in the combustion chamber generally near the spark plug during the start of combustion.

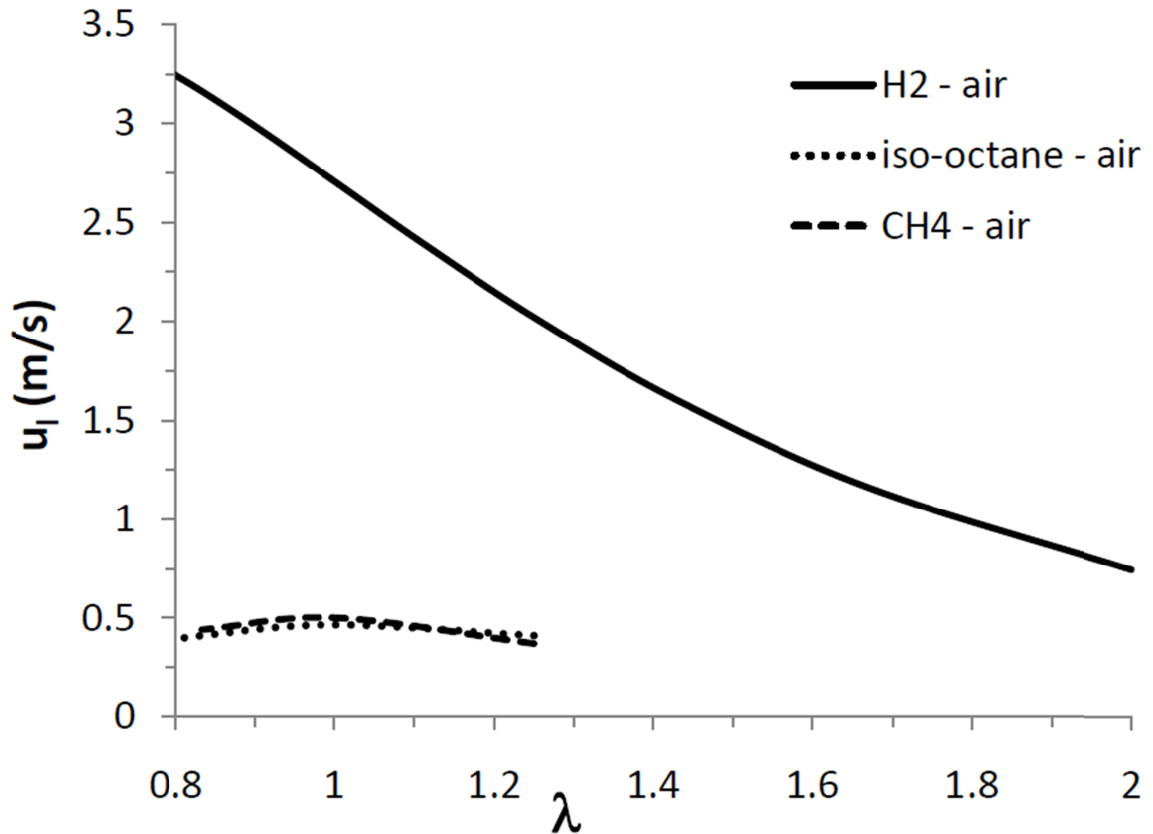


Figure 1.1: Comparison of laminar flame speeds of hydrogen, methane, and iso-octane as a function of lambda [1].

The laminar flame speed and laminar burning flux for hydrogen are shown as a function of equivalence ratio for a variety of pressures in Figure 1.2. At an equivalence ratio of $\phi = 0.75$, the laminar flame speed at 20 bar is roughly twice that seen at 50 bar. This fundamental reduction in flame speed will negatively impact burn durations when engines are turbocharged or compression ratios are increased.

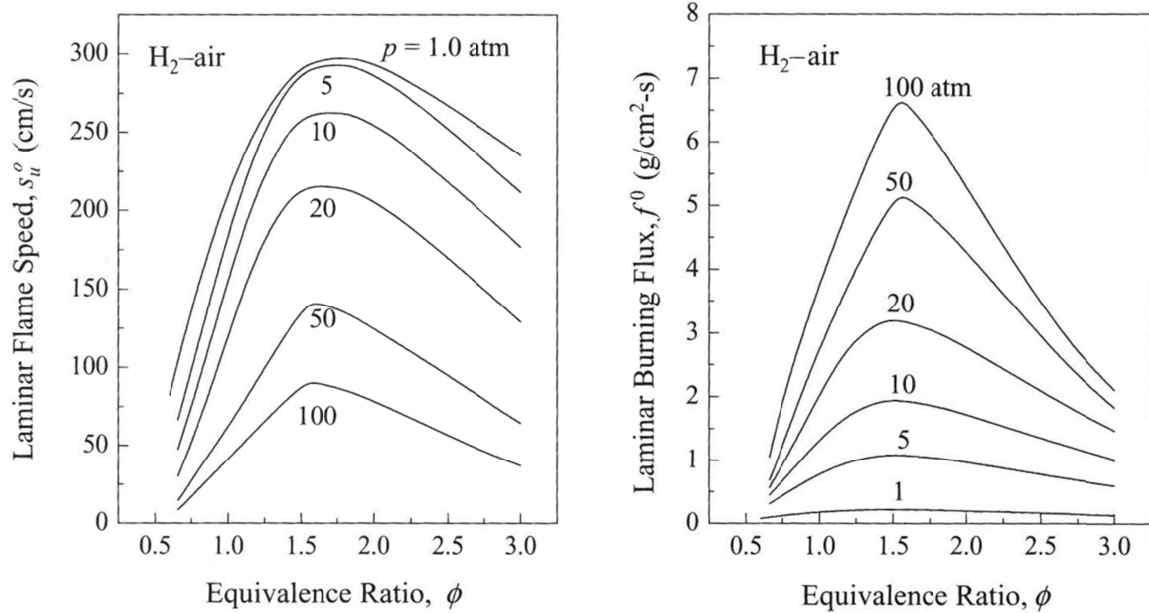


Figure 1.2: Laminar flame speed and laminar burning flux for hydrogen as a function of pressure and equivalence ratio [5].

The adiabatic flame temperature and the laminar flame speed for hydrogen are presented in Figure 1.3 as a function of equivalence ratio. The adiabatic flame temperature is above 2300 K in the range of $\phi = 1.2$ to $\phi = 2.7$. At stoichiometric conditions, the flame temperature is about 1800 K, and at $\phi = 0.6$, the flame temperature is reduced to under 1100 K. The strong sensitivity of flame temperature to equivalence ratio indicates reducing the local equivalence ratio should dramatically improve NO_x emissions and reduce heat losses to the cylinder wall.

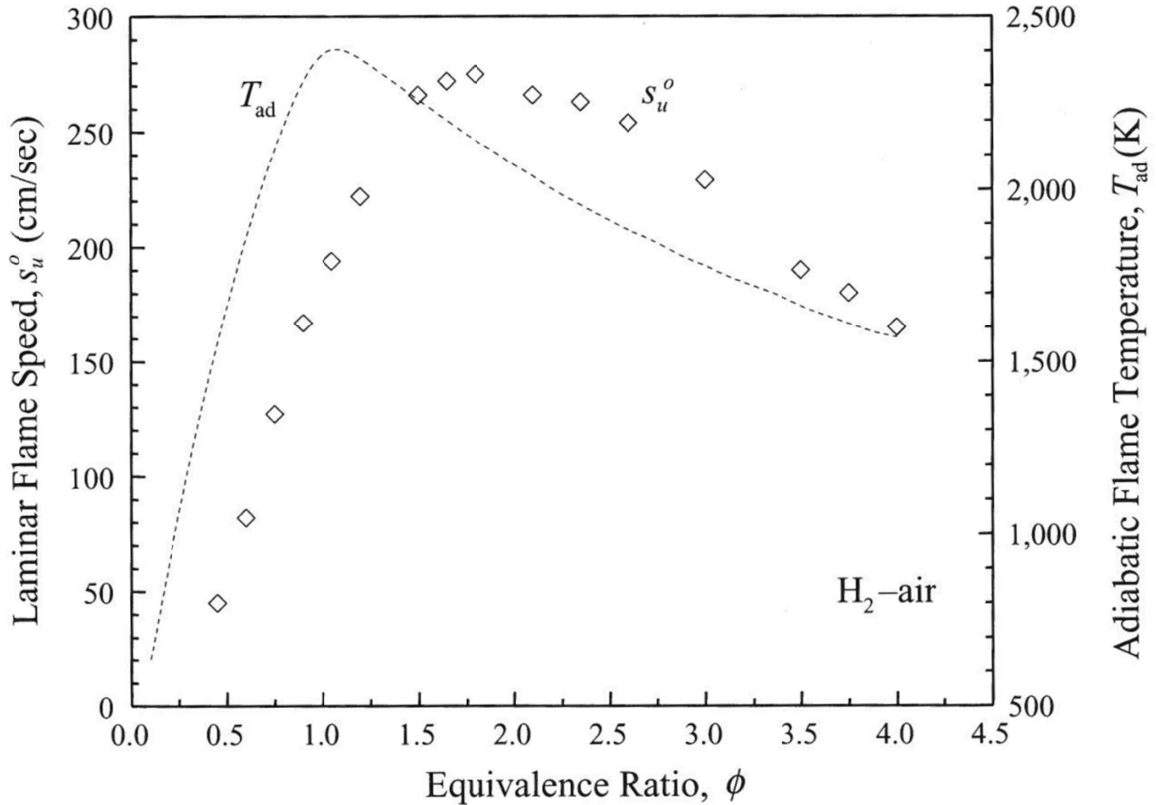


Figure 1.3: Laminar flame speed and adiabatic flame temperature for hydrogen as a function of equivalence ratio at atmospheric pressure [5].

Unfortunately, several fundamental properties of hydrogen have inherent disadvantages when compared to conventional fuels. Above equivalence ratios of approximately $\phi = 0.4$, homogeneous H_2 combustion in engines reaches temperatures at which NO_x production becomes subject to vehicle-level regulation. Because the equivalence ratio is still quite lean, the reduction of NO_x with conventional three way catalysts is impracticable. Methods to increase engine efficiency further, such as increasing compression ratio or stratifying the engine charge during combustion, increase local or global temperatures during combustion and exacerbate NO_x generation. If emissions compliance is desired, strategies to improve H_2 engine efficiency must be coupled with strategies to minimize NO_x emissions.

	Hydrogen	Methane	Iso-Octane
Molecular Weight (g/mol)	2.016	16.043	114.236
Density, STP	0.08	0.655	692
Minimum Ignition Energy (mJ)	0.02	0.28	0.28
Quenching Distance (mm)	0.64	2.03	3.5
Flammability Limits in air, STP (vol%)	4-75	5-15	1.1-6
Flammability limits (λ)	10-0.14	2-0.6	1.51-0.26
Flammability limits (Φ)	0.1-7.1	0.5-1.67	0.66-3.85
Lower Heating Value (MJ/kg)	120	50	44.3
Higher Heating Value (MJ/kg)	142	55.5	47.8
Stoichiometric air to fuel ratio (kg/kg)	34.2	17.1	15
Stoichiometric air to fuel ratio (kmol/kmol)	2.387	9.547	59.666
Autoignition Temperature ($^{\circ}$ C)	585	540	396
Research Octane Number	≥ 130	≥ 120	100
Kinematic viscosity (m ² /s)	$110 \cdot 10^{-6}$	$17.2 \cdot 10^{-6}$	$1.2 \cdot 10^{-6}$
Thermal Conductivity	0.182	0.034	0.0112
Diffusion Coefficient in Air	$0.61 \cdot 10^{-6}$	$0.16 \cdot 10^{-6}$	$0.07 \cdot 10^{-6}$
Laminar Flame speed at $\Phi = 1$	2	0.4	0.5
Specific Heat Capacity (J/g-K)	14.30	2.22	1.66

Table 1.1: Comparison of the combustion properties of hydrogen, methane and iso-octane [1] [3].

In addition, combustion control can be problematic for hydrogen engines. Figure 1.4 compares the ignition energy for hydrogen, as a function of equivalence ratio, to methane and heptane; the values shown for hydrogen are quite low. The low minimum ignition energy, when combined with wide flammability limits, shown in Figure 1.5, make uncontrolled ignition and aberrant combustion possible. High temperatures in cylinder, whether on the combustion chamber surface or in the post-exhaust residual charge of the cylinder, can initiate combustion when H₂ and air are introduced to the chamber [6], [7].

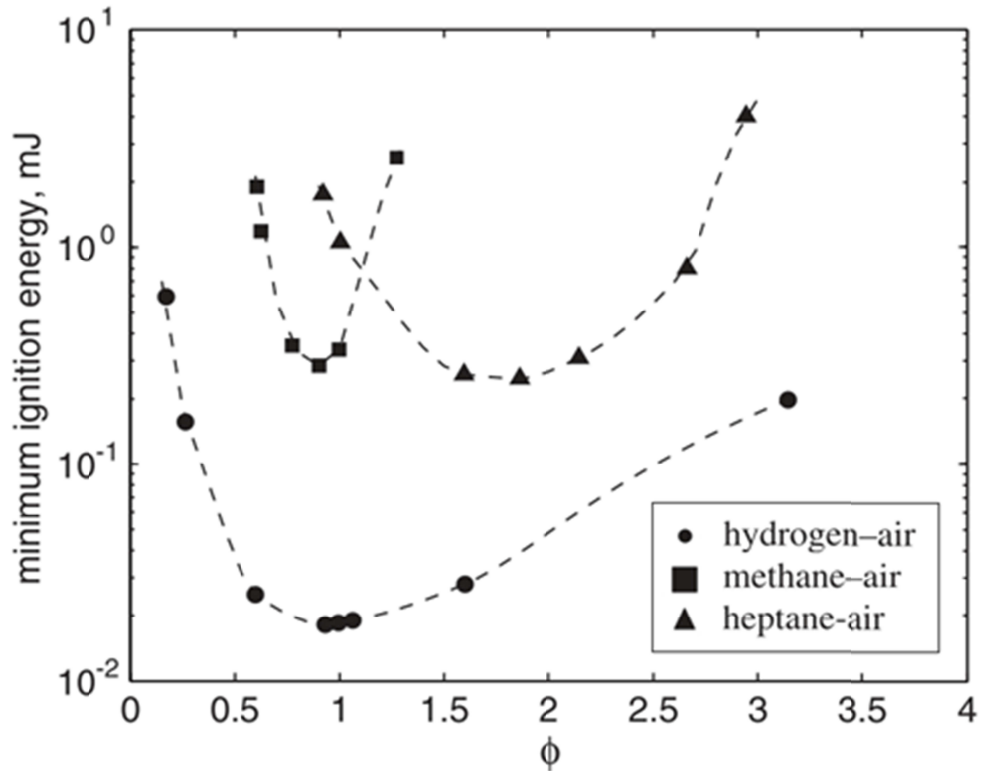


Figure 1.4: Minimum ignition energy for hydrogen, methane, and heptane mixtures as a function of equivalence ratio at atmospheric pressure [8][9].

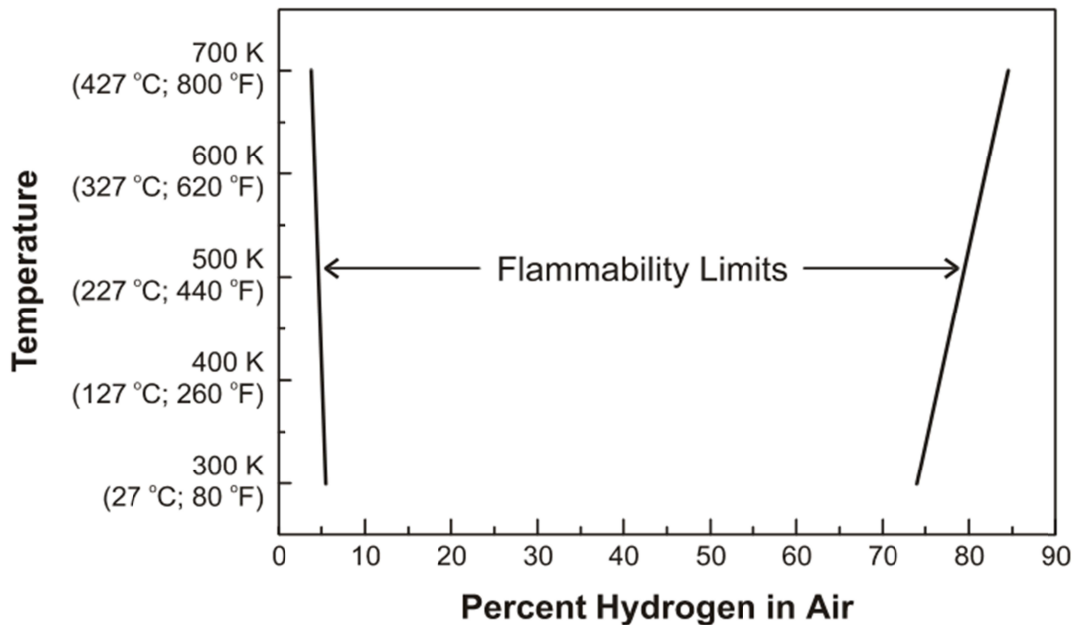


Figure 1.5: Change in Flammability Limits for H₂ and Air with Respect to Temperature at 1 atm [4].

Heat transfer can be problematic as well. The low quench distance and high temperatures possible can result in higher heat transfer to the walls of the combustion chamber, which can reduce engine efficiency. Owston *et al.* concluded that heat transfer from a stoichiometric hydrogen flame into the engine was roughly twice that of gasoline engines [10].

The net result is that hydrogen-fueled engines can tolerate very high compression ratios; but a great deal of care must be taken in order to control the temperatures in the chamber. Additionally, imperfections from the cylinder manufacturing process should be corrected, and oil ingress into the chamber should be minimized.

1.2 Hydrogen Engine Studies External to Ford/University of Michigan

1.2.1 Jet Development

Although port-injection (PI) H₂ engines have been shown to be quite efficient, a large amount of research has been conducted over the past decade to understand and improve the combustion in the cylinder through the use of direct in-cylinder fuel injection.

Some of the research that has been conducted has improved the understanding of jets sprayed into a chamber under conditions similar to those experienced in direct-injection (DI) engines. Roy *et al.* [11] tested spray through a single 1.0 mm orifice into a constant chamber volume, while varying fuel pressure and ambient pressure. As expected, the penetration increased when fuel pressure increased, and decreased when chamber pressure increased. In addition, ambient pressure was found to have an effect on the structure of the fuel jet. Similarly, Petersen *et al.* [12], [13] conducted Schlieren work

characterizing the nozzle spray angle and penetration of four injectors into static high pressure nitrogen.

1.2.2 Nozzle Pattern Development

Many nozzle designs have been tested on various engines, as well, see [14–16]. A few of these designs are reviewed here. Kim et al. [16] tested four nozzles, including one nozzle intended to induce swirl in the chamber. These nozzles are shown in Figure 1.6 [17]. Both metal engine tests and optical Schlieren tests were conducted. The full-open nozzle was shown to have superior efficiency and combustion stability.

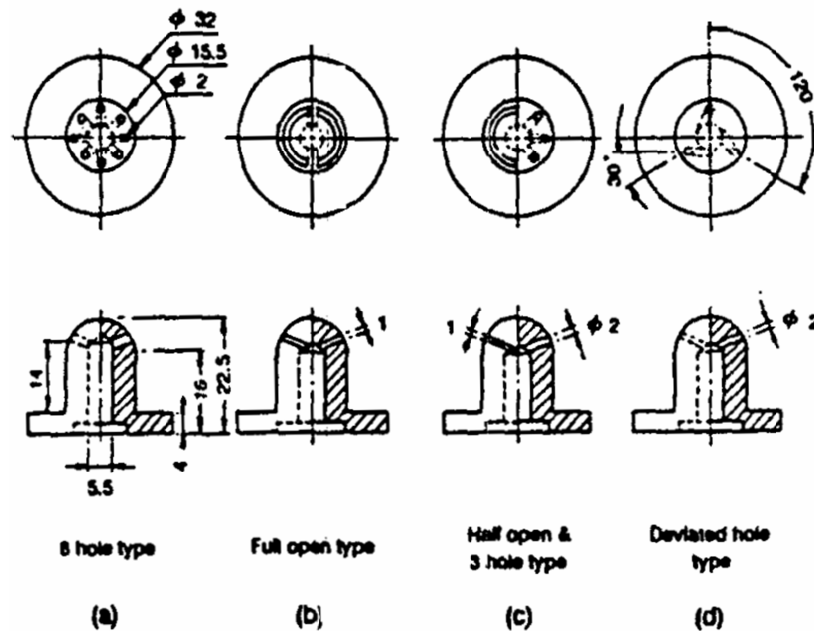


Figure 1.6: Four Nozzles Tested by Kim et al [17].

Wallner et al. [17] at Argonne National Laboratory (ANL) tested two nozzles in central and side locations. The nozzles are shown in Figure 1.7. The best efficiency was seen with the 5 hole injector when located in the side of the combustion chamber with the nozzles oriented towards the spark plug ("up"). Unfortunately, at those conditions, NO_x emissions exceeded 150 ppm. This would likely require aftertreatment to comply with emissions regulations.

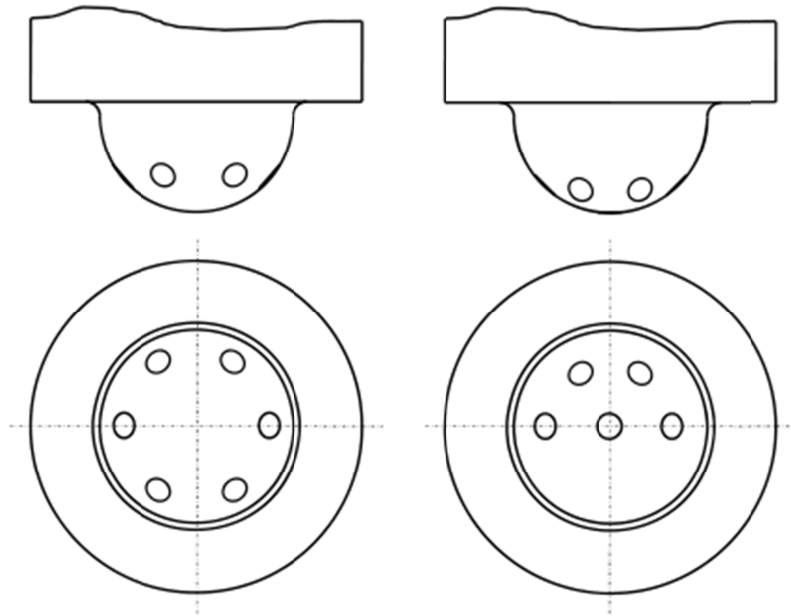


Figure 1.7: Two nozzle tested by Wallner et al [18].

Some work combined a broad scope of optical engine tests, metal engine tests, and computational fluid dynamic (CFD) simulations, starting with the simple case of a single jet, shown in Figure 1.8. The research was the result of a cooperative effort between ANL and Sandia National Laboratories (SNL) with the express intent of calibrating CFD tools for H₂ IC engines using metal and optical engine results. Work at ANL generally concentrated on metal engine and/or large-scale CFD modeling (using a Reynolds averaged Navier Stokes (RANS) approach). The ANL work complemented the studies at SNL, which focused on optical engine experiments and some CFD studies based on large eddy simulations (LES) to better understand the physics of hydrogen fuel sprays and engine performance. Planar laser induced fluorescence (PLIF) and particle image velocimetry (PIV) experiments were conducted at SNL by Salazar and Verhelst et al. [19–23]. The results were used by Scarcelli et al. at ANL to calibrate a RANS-level CFD code [21,23,24]. After the calibration was complete, there was good agreement between experiment and simulation. The same model was then used

to help understand several multi-hole injectors, including at least two Ford injectors that will be described later in this dissertation [25].

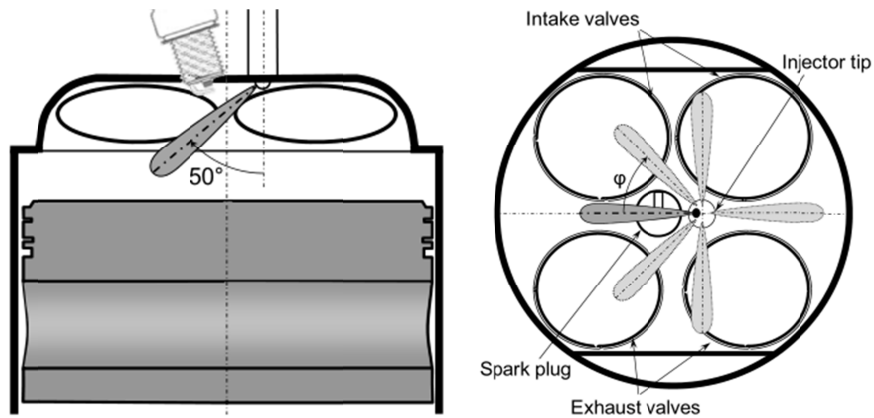


Figure 1.8: Single nozzle injector tested by Wallner et al [15].

The tests conducted at ANL to optimize spray geometry were later expanded to include the four nozzle designs shown in Figure 1.9. Note that the Ford-designed 5-hole (5H) and 13-hole (13H) injectors were tested by ANL. The results of the studies of the 5H and 13H injectors at Ford Motor Company are presented in Chapter 3. At ANL, the 5H injector had good efficiency; eventually reaching 45.3% brake thermal efficiency (BTE) based on the lower heating value (LHV) of hydrogen with estimated friction losses and simulated turbocharging. The 4-hole injector also yielded excellent performance with 45.4% BTE.

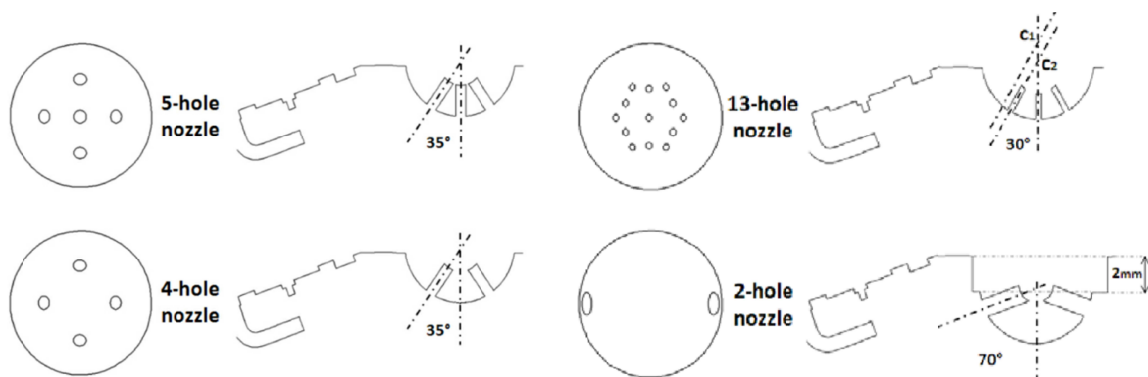


Figure 1.9: Four Injectors tested by Wallner, et al. and Matthias, et al.[14], [16]

1.2.3 Dilution Strategies

Stoichiometric operation of hydrogen engines is desirable, as it enables the use of conventional 3-way catalysts and increases the maximum power density of the engine. However there are fundamental limitations that restrict the maximum equivalence ratio that can be practically used in an H₂ IC engine. The fast combustion speed of hydrogen can result in a rate of pressure rise that exceeds the limits of conventional engine design. The quench distance of hydrogen flames is small, and the adiabatic flame temperature of hydrogen at stoichiometric conditions and atmospheric pressure (2383 K) is higher than that of iso-octane (2210 K). As a result, hydrogen engines operating at near stoichiometric conditions can produce large amounts of NO_x, transfer a large amount of energy to chamber walls, and can impact engine durability negatively.

In order to reduce the severity of these problems, most hydrogen engines are designed to operate with the combustion charge diluted with excess air. Some typical results are shown in Figure 1.10, where the equivalence ratio varies from 0.22 to 0.72 and excess air ranges from 355% to 38%.

Unfortunately, the threshold of NO_x level that is acceptable for automotive applications is generally reached between $\phi = 0.4$ and 0.5. Most proposed strategies have suggested a maximum equivalence ratio of approximately $\phi = 0.45$. These strategies will indirectly increase friction losses when the engine size is increased to meet peak power requirements.

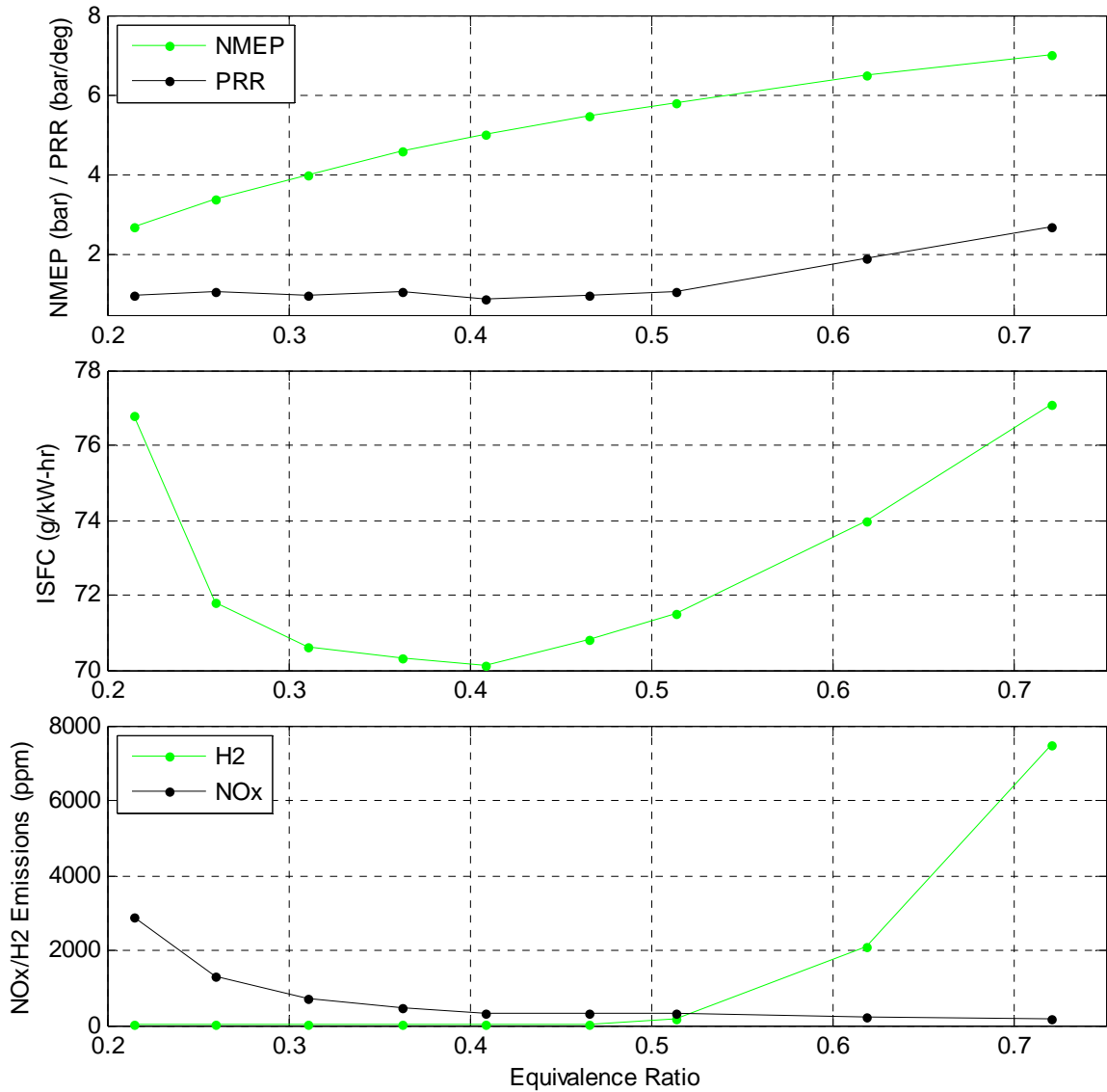


Figure 1.10: Typical NMEP, ISFC, NO_x, H₂, and pressure rise rate performance of an unthrottled PI engine at 3000 RPM (work conducted as part of this dissertation study).

To mitigate the NO_x problem while maintaining power density, alternative approaches to diluting the combustion charge have been attempted. For example, this research effort includes the results of water injection (presented in Chapter 4) as a means to increase the maximum power density achieved while

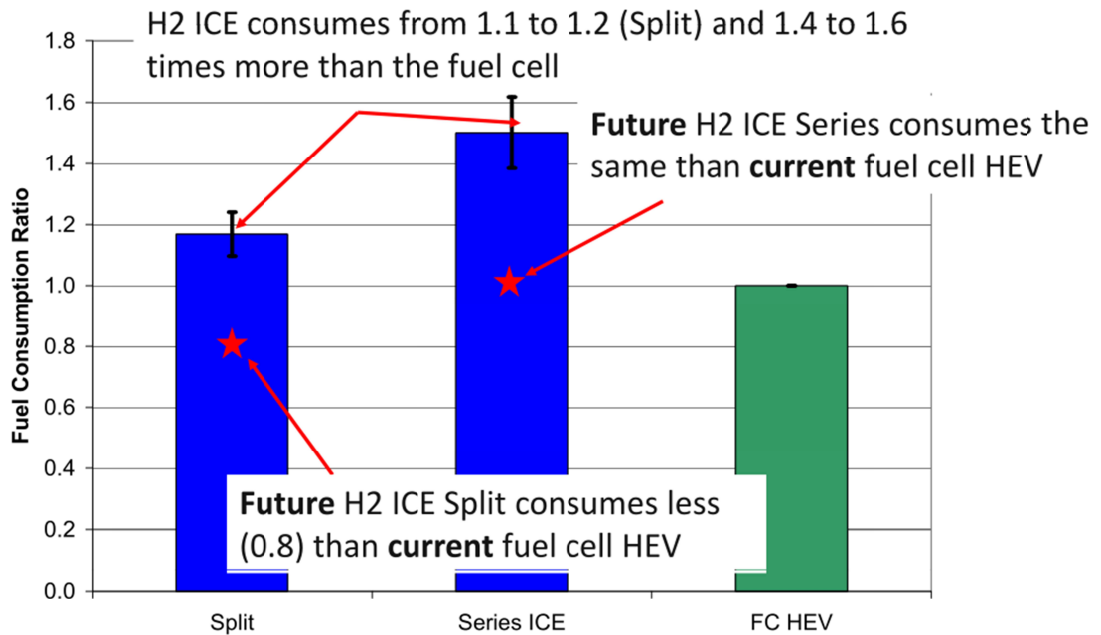
maintaining acceptable NO_x emissions. Nande et al. [26] at ANL expanded the water injection research using the same water injectors and similar hardware to the equipment used in this study. Nande et al. [26] investigated the tradeoff between NO_x and engine output while injecting smaller amounts of water than used in this study. In the work by Nande et al. [26], injecting water resulted in a 27% reduction in NO_x with a 1% reduction in efficiency, which was over 11 times more effective than a similar attempt to reduce NO_x through retarding spark (for the conditions tested).

In addition to excess air dilution and water dilution, dilution via exhaust gas recirculation (EGR) and valve timing strategies to trap more internal exhaust residual have also been attempted. For example, Blechmore et al. [27] compared a water injection strategy with both uncooled EGR and cooled EGR at stoichiometric conditions. When compared to a baseline strategy of operation at $\phi = 0.4$, efficiency was reduced for all strategies tested. Compared to $\phi = 0.4$, fuel consumption was increased by 9% for cold EGR and 12% for hot EGR. For water injection, fuel consumption increased by about 15% in the study by Blechmore et al. [27].

1.2.4 Vehicle-level Efficiency

Cumulatively, the advantages of H₂ combustion result in vehicle-level efficiencies that approach and perhaps improve upon fuel cell efficiencies in automotive applications. As seen in Figure 1.11, the results of the analysis by Rosseau et al. show fuel consumption of PI H₂ engines (circa 2008) is approximately 1.24 times that of current fuel cells [27,28]. With improvements to the combustion system, in particular DI mixture formation, turbocharging, slightly improved friction, and split hybrid operation, the H₂ DI 'future' engine was projected to use approximately 20% less fuel than current fuel cells. These improvements were believed to be achievable with additional research to

understand the spray and combustion properties of H₂ in an internal combustion engine.



Current vs. current -> H2 ICE Split will consume 1.24 more than fuel cell
 Future vs. future -> H2 ICE Split will consume 1.1 more than fuel cell
 Current fuel cell vs. future ICE -> H2 ICE Split will consume **0.8 less** than fuel cell

Figure 1.11. Comparison of projected H₂ DI IC engine fuel consumption with H₂ PEM fuel cell consumption.[28]

1.3 Studies at Ford Motor Company

1.3.1 H₂ DI studies not conducted by the author

Prior to the author's research, Ford Motor Company completed many studies on several iterations of H₂ hardware. Some of the hardware that was tested is shown in Tables 1.2-1.4.

In the first generation cylinder head design, the spark plug was located at the side of the head, between the intake valves. The injector was located in the center of the head. In the second generation the positions of the injector and spark plug were switched. The third generation located both the injector and the spark plug in the center of the cylinder head. Due to the small quench distance

of hydrogen, heat losses were anticipated to be large, and the cylinder heads were designed to minimize charge motion. In general, each successive iteration of cylinder head design improved the overall efficiency of the engine. Auxiliary holes in the combustion chamber provided access for pressure measurement and optical access.

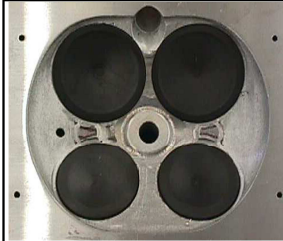


			
Name	Gen I	Gen II	Gen III
Injector Location	Central	Side	Central
Spark Plug Location	Single Side	Central	Central
Designer	Haghgoei	Production	Boyer/Stockhausen/ Pappianou

Table 1.2: Various cylinder heads tested at Ford.

Table 1.3 shows some of the piston designs that were evaluated. In general, efficiency was shown to be better with higher compression ratios, lower surface area, and lower crevice volumes.







						
Name	12.2	16	14	10.2	11.8	mod 10.4
Letter	A	B	C	D	E	F
Configurations #'s	1-3, 9-14	4-6	7	8	15, 16	17
Engine Stroke	79 mm					
Comp. Ratios Tested	12, 12.2	12, 14, 16	14	10.2	10.8, 11.8, 12	12
Cyl. Heads Tested with	All Three	Gen III: Cen/Cen	Gen III: Cen/Cen	Gen III: Cen/Cen	Gen III: Cen/Cen	Gen III: Cen/Cen

Table 1.3: Various pistons tested at Ford.

Table 1.4 shows some of the hydrogen DI fuel injectors designed and tested at Ford. The 13H injector showed superior efficiency in many pertinent situations and was chosen by the author for further testing. The results of the 13H injector study are presented in Chapter 3. In general, at the start of the

author's research, designs were chosen to concentrate hydrogen in the center of the chamber in order to avoid large heat losses to the chamber walls.

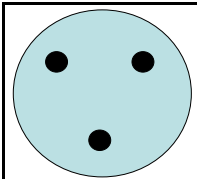
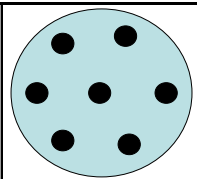
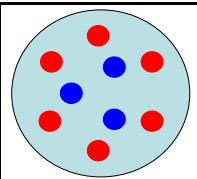
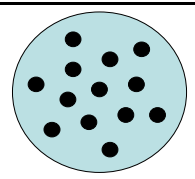
				
Pattern	3H	7H	9H	13H
Hole Angle wrt Cyl Axis	45	0/60	30/60	0/30
Nozzle Diameter (mm)	0.798	0.522	0.461	0.383
Nozzle Area (mm ²)	0.500	0.214	0.167	0.115
Total Flow Area (mm ²)	1.500			

Table 1.4: Various injectors tested at Ford.

1.3.2 H₂ DI studies done at Ford Motor Company by the author

Upon reviewing the DI hydrogen literature and prior studies conducted at Ford Motor Company, the author found that key parameters for controlling the efficiencies of H₂ IC engines (as with gasoline DI engines) are the fuel injector design, including the nozzle geometry and injector orientation in the combustion chamber, coupled with the combustion chamber geometry, which includes the piston and cylinder head design.

The cylinder heads tested by the author are shown in Table 1.5. The cylinder heads have identical valvetrains and very similar ports. In order to improve burn rate, two spark plugs were located on the outside of the cylinder chamber.


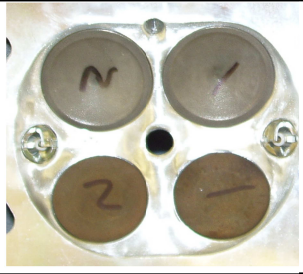
		
Name	Gen III	Gen IV
Injector Location	Central	Central
Spark Plug Location	Central	Dual Side
Designer	Boyer/Stockhausen/ Papaionnou	Younkins/Boyer

Table 1.5: Comparison of cylinder heads tested by the author.

Some pistons that have been tested by the author are shown in Table 1.6. Based on prior experience, attempts were made to minimize surface area and crevice volume to the largest extent possible. Pistons "F", "G", and "J" have small to moderate domes, piston "I" is a flat top with minor valve reliefs, and pistons "H" and "H-" were shaped in an attempt to create locally rich zones near the spark plugs.







						
Name	mod 10.4	mod 12.2	H	Modified H	Flat Top	Wendy
Letter	F	G	H	H+	I	J
Configurations #'s	18, 19	20	22	25, 26	21, 23, 27, 29, 30	24, 30-36
Engine Stroke	79	95 mm				
Comp. Ratios Tested	11.7, 10.4	12.6	13.9	11.4, 13.4	11.6, 12.5	12, 12.5, 13.7, 15.7
Cyl. Heads Tested with	Central Ign	Dual Side Ign	Dual Side Ign	Dual Side Ign	Central, Dual Side	Dual Side Ign
Designer	Boyer/Jung	Boyer/Younkins	Boyer/Younkins	Boyer/Younkins	Boyer/Younkins	Boyer/Younkins

Table 1.6: Summary of piston designs tested by the author.

Some of the injector nozzle geometries that the author selected and designed to test are shown in Tables 1.7-1.9. Performance metrics of the 12H, 13H, 5H and 3+3H are described in Chapters 3, 4, 6, and 7. The nozzle designs were created at Ford Motor Company. The injectors were developed by Westport Innovations.[29]




			
Pattern	5H	3+3	13H
Hole Angle wrt Cyl Axis	0/35	45/70	30
Nozzle Diameter (mm)	0.597	0.545	0.313
Total Flow Area (mm ²)	1.4	1.4	1.0
Designer	Boyer	Younkins/ Boyer	Haghooei/ Han/Boyer

Table 1.7: Summary of injector designs tested by the author, Part 1.

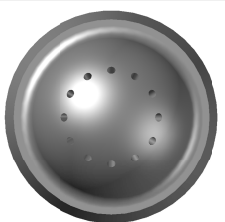
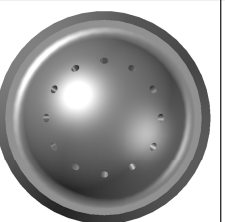
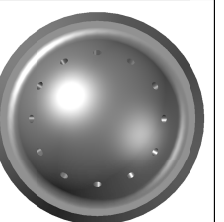
			
Pattern	12H		
Hole Angle wrt Cyl Axis	40	50	60
Nozzle Diameter (mm)	0.326		
Nozzle Area (mm ²)	0.083	0.083	
Total Flow Area (mm ²)	1.0		
Designer	Boyer/Younkins		

Table 1.8: Summary of injector designs tested by the author, Part 2.

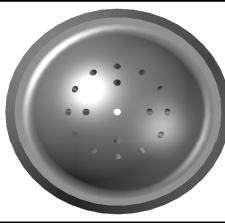
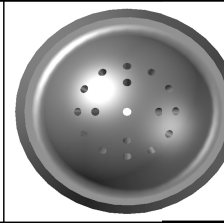
		
Pattern	17H	
Hole Angle wrt Cyl Axis	0/25/40	
Hole Diameter (mm)	0.274	0.324
Total Flow Area (mm ²)	1.0	1.4
Designer	Boyer/Younkins	

Table 1.9: Summary of injector designs tested by the author, Part 3.

Of course, with 2 cylinder heads, 6 pistons, 8 injectors, and several compression ratios, a full factorial design of experiments is daunting, even before considering each configuration was generally tested at 3-5 engine speeds with 8-20 different tests. For this study, 12 combinations of cylinder head, piston and compression ratio were selected for testing. Appendix A presents an abbreviated list of the configurations used and the tests conducted.

1.4 Research Objectives and Summary of Dissertation

The primary objective of this research is to demonstrate improvements in the efficiency and emissions control of a hydrogen-fueled IC automotive engine. Specifically, the intent of this work is to characterize engine performance of various permutations of injectors, cylinder heads, pistons, and compression ratios and interpret the data in terms of fundamental understanding of H₂ mixing, ignition, and combustion phenomena. The effects of varying parameters that impact fuel distribution (namely, injection timing and nozzle design) and engine dilution (via excess air and/or water injection) are documented and analyzed.

In Chapter 2, the experimental setup at Ford Motor Company is described. Details of the single-cylinder research engine and associated instrumentation are presented, and the margin of error of pertinent measurements is reviewed.

In Chapter 3, experimental results for several injector nozzle designs are reviewed for a variety of compression ratios. The NO_x emissions, combustion statistics, and a breakdown of some efficiency losses are compared for a variety of hardware iterations.

In Chapter 4, the performance of the engine operated with auxiliary liquid water introduced into the engine cylinder is reviewed. Fuel is delivered via the intake port. The reduction in emissions is compared against values without water injection.

In Chapter 5, the engine is again operated with water injection, but in contrast to Chapter 4, the water is injected into the intake port. The fuel is delivered directly into the cylinder. The impact of phasing the water injection in relation to combustion is reviewed, and the reduction in emissions is compared to expected and predicted values.

In Chapter 6, experimental results of the dual-side-ignition cylinder head and the dual-zone 3+3H injector are introduced and contrasted with those of the conventional cylinder head and 5H injector.

In Chapter 7, the results of optical engine studies at Sandia National Laboratories are reviewed, including a description of the planar laser induced fluorescence (PLIF) diagnostic used. The PLIF test matrix is defined, and the results of the tests are summarized.

In Chapter 8, a brief summary of the work and conclusions are presented. Areas of future work are also discussed.

Chapter 2

Experimental Setup: Metal Engine

The dynamometer cells at Ford Motor Company's Research and Innovation Center have been designed to test a wide variety of internal combustion engines at all conditions experienced in an automotive drive cycle. The performance metrics measured include the mechanical output of the engine, the amount of fuel consumed, the composition of the exhaust gas emissions, and important temperatures and pressures during operation. In order to minimize measurement variation, all metal-engine tests in this study were conducted in a single dynamometer cell, shown in Figure 2.1.

2.1 Dynamometer

A 300 horsepower A/C dynamometer was used to control engine speed and absorbed torque. The A/C motor floated on an oil film in order to reduce friction; reaction torque from the energy absorbed was transmitted through a load cell and then absorbed by the cell floor. Absorbed power was then calculated through the length of the torque arm, the measured force, and the measured dynamometer speed.

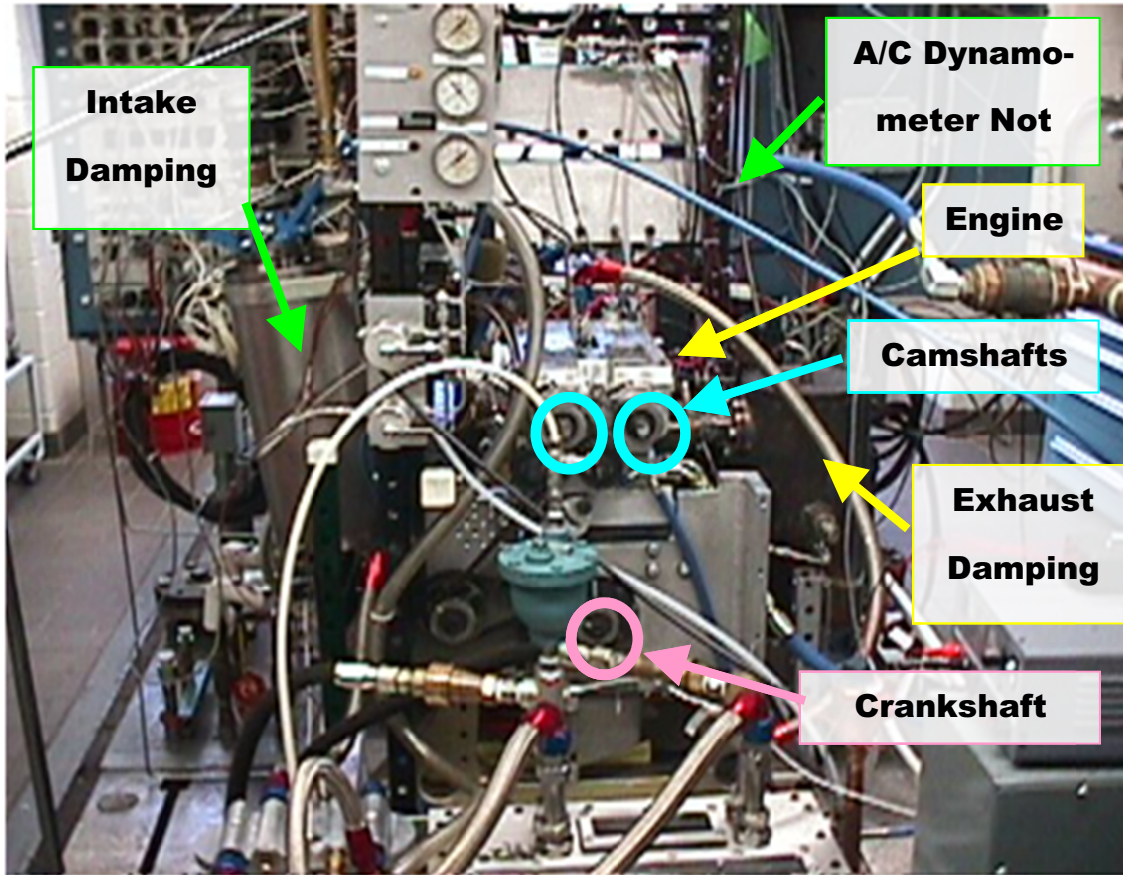


Figure 2.1: The H₂ IC engine dynamometer test cell at Ford Motor Company used for this study.

2.2 Safety Measures

Additional safety measures were specifically implemented for the hydrogen IC engine studies. The dynamometer test cell was heavily ventilated, with complete air turnover in the cell every minute. Hydrogen sensors were placed above the hydrogen supply line and were coupled directly to hydrogen shut-off valves. As hydrogen combustion is not always readily visible, an infrared camera monitored engine operation and provided a diagnostic for potential hydrogen flames. The integrity of the fuel system was checked each day. Hydrogen was introduced in steps of increasing pressure, and the pressure decay was analyzed to determine if leaks were present.

2.3 Instrumentation

Some of the instrumentation used to test the performance of the engine is shown in Table 2.1. Fuel flow was measured with a coriolis flow meter with a specified accuracy of $\pm 0.1\%$ of measurement. Intake air was metered by pressurizing air and directing the flow through choked nozzles. Pulsations resulting from single-cylinder operation were dampened by flowing the intake air through drums of approximately 25 liters each.

		Manuf.	Model	Full Scale	Error
High Speed Pressure Transducers	Cylinder	AVL	GU21C	250 bar	1% IMEP
					0.3% Linearity
					1% Peak Pressure
	Aux. Cylinder	Kistler	6125B	250 bar	2% IMEP
					0.5% Linearity
					1% Peak Pressure
Intake	Kistler	4045	2 bar	0.3% FS	
Exhaust					
Low Speed Pressure Transducers		Druck		2 bar, 5 bar	0.5% FS
Thermocouples	Various		K-type	1250	1.1 degree or 0.4%
Air Flow: Critical Nozzles		Ford Proprietary		1500 kg/hr	0.5% of Meas.
Fuel Flow: Coriolis Meter		Emerson	Micromotion Coriolis	5 kg/hr	1% of Meas.
Water Flow: Coriolis Meter				20 kg/hr	1% of Meas.
Brake Torque Load Cell		Interface	1110CBX-300	300 lbs	0.02% FS
Emissions	CO ₂ *	Horiba	MEXA-7100 EGR		+/- 0.87% FS*
	THC*				+/- 0.87% FS*
	CO (H)*				+/- 0.87% FS*
	CO (L)*				+/- 0.87% FS*
	NO _x (H)			10000 ppm	+/- 0.87% FS*
	NO _x (L)			100 ppm	+/- 0.87% FS*
	O ₂			25%	+/- 0.87% FS*
	H ₂	V & F	H-Sense	>30,000 ppm	+/- 3% FS

Table 2.1: H₂ IC engine instrumentation.

All in-cylinder pressure measurements were acquired using piezoelectric pressure transducers with matched amplifiers (see Table 2.1 for model specifications). The cylinder pressure signal was correlated with a high-speed pressure sensor located in the intake port for every cycle of engine data. With the central ignition/central injection combustion chamber, the cylinder head had enough space to add an auxiliary cylinder pressure sensor to improve measurement accuracy.

Crank angle was measured with a 720 slot rotary encoder and laser mounted at the rear of the engine. The angle corresponding with top dead center (TDC) was initially determined using a capacitive probe and compared to pressure sensor data. Afterward, TDC timing was determined using measured thermodynamic loss angle. As a general rule for gasoline engines, an error of one degree in determining crankshaft angle can result in an error of up to 10% in indicated mean effective pressure (IMEP) [30]. Since hydrogen engines have a wide range of pressure rise rates, the IMEP error introduced from incorrect crankshaft angle determination may vary widely as well. As such, it is instructive to introduce artificial error into test data of crankshaft angle/volume measurements and analyze the resultant change in predicted IMEP.

The results of such an analysis are shown in Figure 2.2. The data were taken from a test conducted at 3000 RPM and an equivalence ratio of $\phi = 0.4$. The IMEP error shown is the average of +1 and -1 degree shifts in the assumed crankshaft angle. The error peaks at a pressure rise rate of approximately 2 bar/degree. At points lower than 2 bar/degree, the burn durations are quite long, with 10-90% taking 40 degrees or more. At these conditions, minor changes in estimated volume have a relatively small effect on IMEP. Conversely, at high pressure rise rates, combustion is near constant-volume, with 10-90% burn taking approximately 6 degrees. As such, with a slider-crank mechanism, the velocity of the piston is low during the entire combustion event, and the

error resulting from incorrect crankshaft angle determination is reduced. It is expected that the error in determining actual crankshaft angle is less than 0.2%. The error in reporting IMEP is expected to be less than 1.4%. The manufacturers of the pressure transducers expect errors in IMEP determination due to inaccurate pressure to be less than 1.0%, and actual errors tend to be less than 0.5% [31]. These combined independent sources of error result in an overall measurement uncertainty in IMEP of 1.7%

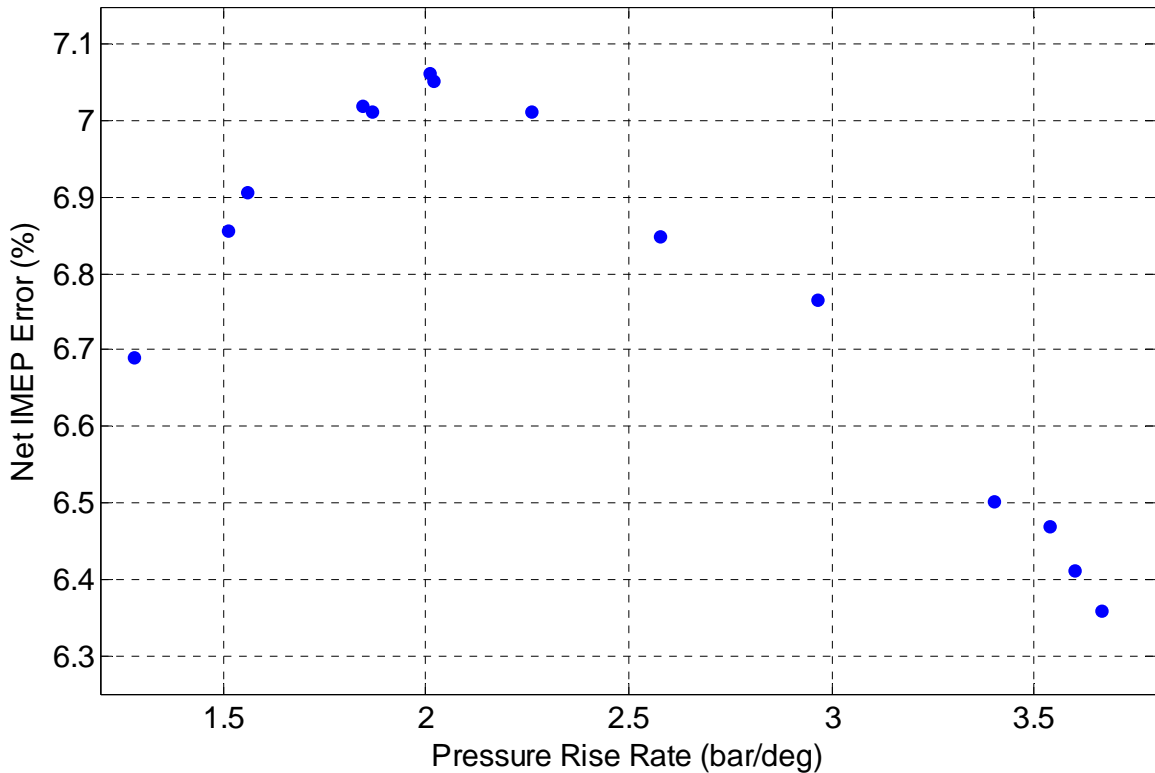


Figure 2.2: Net IMEP change resulting from a change in crankshaft angle determination of ± 1 degree, shown as a function of maximum pressure rise rate in the cycle.

Indicated thermal efficiency (ITE) was determined using the measured fuel consumption and in-cylinder pressure time histories. The inaccuracy in ITE is estimated at $\pm 2.5\%$, where the uncertainty is due to the uncertainty in the volume measurements ($\pm 1.4\%$), the pressure measurements ($\pm 1.0\%$), and the fuel flow measurement ($\pm 0.1\%$).

Emissions were measured with an exhaust gas analyzer (Horiba MEXA-7100 EGR). The emissions bench was calibrated daily, and measurement error is specified by the manufacturer to be less than 0.5%. The maximum drift of both the zero and span in an eight hour time period are both specified as 0.5%; as well. The total expected error is assumed to be under 0.87%. Carbon-based emissions resulting from the burning of oil were measured and recorded. For all tests these emissions levels were quite low and are not reported in this work.

2.4 Hydrogen

The hydrogen used during testing was high purity, as the delivery system was originally designed for fuel cells that specified operation with >99.9% purity H₂. The hydrogen was liquefied, both to reduce volume and eliminate impurities. During operation, the hydrogen was boiled and then compressed, using oil-less compressors specifically designed to minimize impurities for fuel cell usage. The hydrogen was then regulated until pressure reached 115 bar (absolute). The fuel was then allowed to flow to the test cell. For DI experiments, 110 bar (absolute) was maintained at the fuel rail. For PI experiments, the fuel pressure was regulated down to 4 bar (absolute).

2.5 Engine Design

Some of the major engine design specifications are shown in Table 2.2. The single-cylinder engine was designed with the crankcase assembly separate from the cylinder assembly; shims could be inserted between the two in order to vary the deck height and compression ratio of the engine.

Bore	89	mm
Stroke	95	mm
Cylinder Displacement	592	cc
Connecting Rod Length	169.1	mm
Intake Valve Diameter	35	mm
Exhaust Valve Diameter	30	mm
Intake Duration	230	deg
Intake Centerline	100	deg ATDC
Exhaust Duration	230	deg
Exhaust Centerline	105	deg BTDC

Table 2.2: Engine dimensions and specifications.

2.6 Experimental Procedure

In general, the effect of changing the H₂/air mixing time was investigated by incrementally decreasing the mixing time allowed between fuel injection and ignition, which was characterized by the timing of the start of injection (SOI) or the end of injection (EOI). Equivalence ratio was chosen based on prior experience in order to maximize efficiency, minimize NO_x emissions, and maintain reasonable pressure rise rates. For many experiments, the equivalence ratio was set at $\phi = 0.4$.

For each injection timing condition the following procedure was used. Air flow was controlled to establish the desired intake manifold pressure (generally 100 kPa), and torque was monitored in real time. Spark timing was then varied to maximize the observed IMEP. Once optimal ignition timing was determined, the engine was allowed to stabilize for approximately two minutes. After stabilization, slow-speed data (e.g., temperatures, pressures, engine torque, fuel flow, etc.) were recorded for 60 seconds at 10 Hz and then averaged. High speed data (e.g. cylinder pressures, intake manifold and exhaust manifold pressures, and ignition and injection waveforms) were recorded for 300 engine cycles. After acquiring the engine data for the targeted EOI, the mixing time was then reduced by changing the injection phasing incrementally from EOI =

180 degrees before top dead center (BTDC) until combustion was no longer stable.

2.7 Mean Effective Pressure Calculations

The mean effective pressure (MEP) calculations based on experimental cylinder pressure data were calculated using a commercially available program, AdaptCAS. Depending on the intent of the analysis, one of five different MEP values was used. The first, and generally largest value of the five, is commonly called the Gross Indicated Mean Effective Pressure (GIMEP or IMEP 360). This value is calculated by integrating the product of pressure with differential volume and normalizing to torque:

$$IMEP_{360} = 4\pi \frac{\int_{-180^\circ}^{180^\circ} (p \cdot dV)}{V_d} \quad \text{Equation 2.1}$$

The variable p represents the cylinder pressure, dV represents the differential volume, and V_d represents the cylinder displacement. The integral is calculated from BDC of compression (-180°) to BDC of the power stroke (180°) of the engine.

Because several losses are not considered in the IMEP 360, this overestimates the output of the engine. One of the losses is the work required to pump the fluid into and out of the cylinder, commonly known as the pumping mean effective pressure (PMEP). PMEP is calculated in a similar manner as the IMEP 360:

$$PMEP = -4\pi \frac{\int_{180^\circ}^{540^\circ} (p \cdot dV)}{V_d} \quad \text{Equation 2.2}$$

However, the integral is evaluated over the exhaust and intake strokes (180° to 540°) rather than the compression and power strokes. The negative sign is

included to ensure that larger amounts of pumping work are larger numerically; i.e. higher numbers are worse for engine efficiency.

The Net Indicated Mean Effective Pressure (NIMEP or IMEP 720) includes the effect of the pumping losses:

$$IMEP_{720} = IMEP_{360} + PMEP \quad \text{Equation 2.3}$$

The previous three MEP values are all generally calculated from cylinder pressure measurements. An equivalent value can be found by using measured engine brake torque; the result is commonly called the brake mean effective pressure (BMEP):

$$BMEP = \frac{T \cdot 4\pi}{V_d} \quad \text{Equation 2.4}$$

The difference between the output expected from cylinder pressure measurement and the output measured is assumed to be the engine friction; commonly called the friction mean effective pressure (FMEP):

$$FMEP = IMEP_{720} - BMEP \quad \text{Equation 2.5}$$

2.8 Burn Rate Calculations

Burn rates were calculated using the Rassweiler and Withrow procedure and the AdaptCAS software. An analysis of the method is given in [32] and is summarized here. The primary assumption using this method is that the pressure rise can be divided into two separate factors, the pressure change due to combustion (Δp_c) and the pressure change due to volume change (Δp_v).

$$\Delta p = \Delta p_c + \Delta p_v \quad \text{Equation 2.6 [32]}$$

The change in pressure due to volume change is assumed to be a polytropic process:

$$\Delta p_v = p_{i+1} - p_i \quad \text{Equation 2.7 [32]}$$

$$\Delta p_v = p_i \left[\left(\frac{V_{i+1}}{V_i} \right)^n - 1 \right] \quad \text{Equation 2.8 [32]}$$

The mass fraction burned (MFB) is then approximated as being proportional to the pressure increase due to combustion:

$$MFB = \frac{m_b(i)}{m_b(total)} \quad \text{Equation 2.9 [32]}$$

$$MFB = \frac{\sum_0^i \Delta p_c}{\sum_0^N \Delta p_c} \quad \text{Equation 2.10 [32]}$$

For each experiment, the relation between MFB and crank angle was recorded. The crank angle at which MFB = 50% (CA50) and the change in angle between 10% MFB and 90% MFB are commonly accepted as standard for combustion phasing and combustion duration. These values are reported in Chapters 3-6.

Chapter 3

Performance of Conventional PI and DI Hydrogen Engines

3.1 Introduction

Most recent hydrogen research has focused on optimizing fuel distribution through direct in-cylinder injection for improved combustion. However, obtaining optimal efficiency, in general, is a tradeoff of many design and operating parameters. Both port injection (PI) and direct injection (DI) engines can be optimized in terms of the bore/stroke ratio, the compression ratio, the intake manifold pressure, the equivalence ratio, and the engine speed. The efficiency of DI engines is also strongly a function of the parameters used to influence fuel distribution, such as nozzle design and injection timing. To that end, several experiments were conducted and the results are described in this chapter. The efficiency, burn characteristics, and NO_x emissions are compared across a range of engine design parameters and operating parameters.

3.2 PI Engine Efficiency as a Function of Engine Speed and Bore/Stroke Ratio

In general, as engine speeds increase, engine friction, flow losses, and combustion losses will disproportionately increase. Conversely, as engine speeds decrease, heat losses to the cylinder walls will disproportionately increase. Similarly, as bore/stroke ratio increases, friction will decrease, but the reduction

in friction will often be accompanied by poor combustion chamber geometry and heat losses.

It is clear that both bore/stroke ratio and engine speed must be optimized in a system-level design that considers the constraints of friction, heat losses, and combustion losses. This type of optimization is heavily dependent upon the application in which it would be used, and is therefore outside the scope of this work. Nevertheless, some of the general trends of efficiency and combustion statistics are presented here to provide insight into such an optimization.

The specifications for engine design and operation for these tests are shown in Table 3.1. Engine speed was varied from 800 to 4000 RPM, and equivalence ratio varied between $\phi = 0.2$ and 0.7. Tests were conducted at crankshaft strokes of 79 mm and 95 mm. The same cylinder head was used throughout these tests; the compression ratio remained roughly constant by changing the deck height of the engine.

	Value		Unit
Engine Speed	800-4000		RPM
Intake Manifold Pressure	100		kPa
Exhaust Manifold Pressure	100		kPa
Equivalence Ratio	0.2-0.7		Phi
Bore	89.04		mm
Stroke	79	95	mm
Bore/Stroke	1.127	0.937	
Compression Ratio	11.7	11.6	
Ignition	Central		
Injection	Intake Runner		

Table 3.1: Engine Design and Operating Parameters for PI Engine Speed and Stroke Studies.

The indicated thermal efficiency (ITE) is shown in Figures 3.1 through 3.3. Figure 3.1 shows gross ITE as a function of equivalence ratio for the different stroke and engine speeds studied. It is clear that higher engine speeds, and presumably lower heat transfer into the cylinder walls, result in progressively

higher gross ITE. With an engine stroke of 79 mm, peak efficiency increased from 40.8% at 800 RPM and $\phi = 0.37$ to 43.7% at 4000 RPM and $\phi = 0.4$. With an engine stroke of 95 mm, peak efficiency increased from 45.0% at 2000 RPM and $\phi = 0.3$ to 45.6% at 3000 RPM and $\phi = 0.3$.

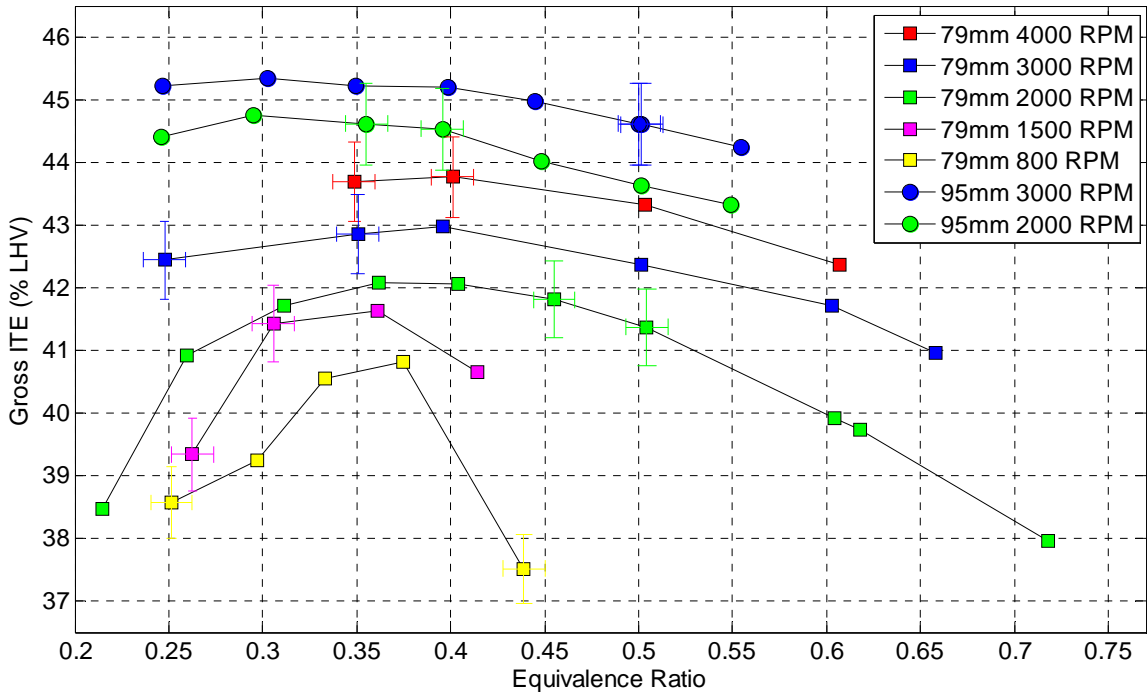


Figure 3.1: Gross ITE as a function of equivalence ratio for several engine speeds and two crankshaft strokes.

Figure 3.2 shows the indicated thermal efficiency including the effects of pumping losses. As engine speed increased, pumping losses from flow restrictions became a greater portion of the total energy loss, which negated some of the advantage in increasing engine speed. This is demonstrated in Figure 3.3, where the results are shown for an equivalence ratio of $\phi = 0.4$ (interpolated from the results shown in Figures 3.1 and 3.2). The improvement in gross ITE above 2000 RPM was approximately 0.8% per 1000 RPM for both the 79 mm stroke and the 95 mm stroke. Below 2000 RPM, the improvement was approximately 2.1% per 1000 RPM. When the effects of pumping losses

were incorporated, the efficiency gain above 2000 RPM was reduced to approximately 0.3% per 1000 RPM.

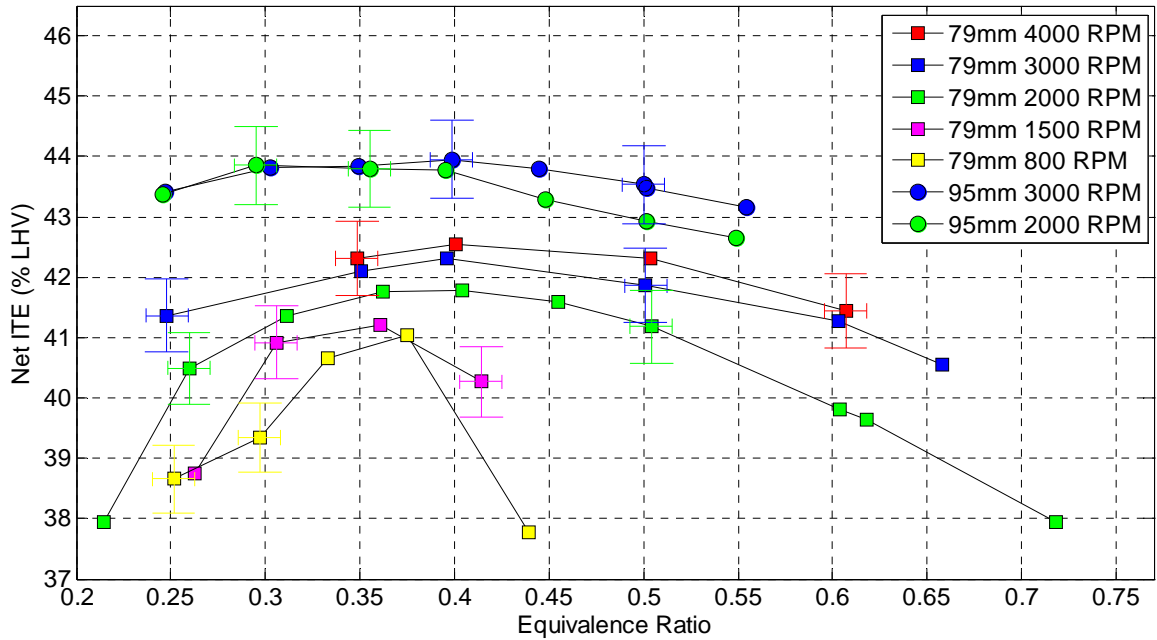


Figure 3.2: Net ITE as a function of equivalence ratio for several engines speeds and two crankshaft strokes.

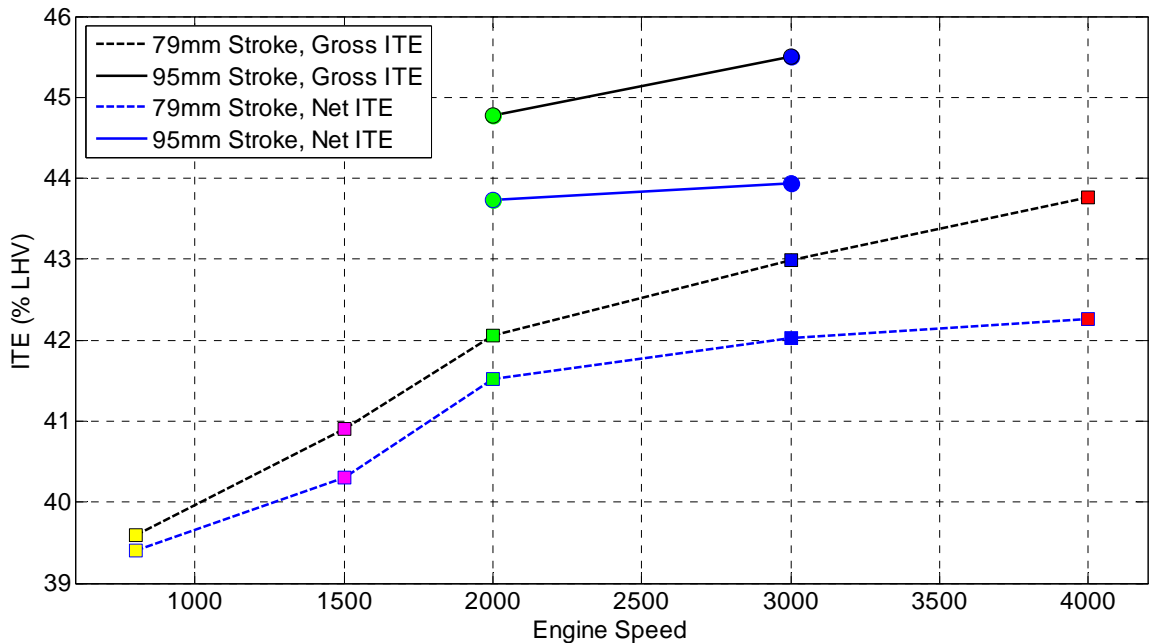


Figure 3.3: Comparison of gross and net indicated thermal efficiency as a function of engine speed for $\Phi = 0.4$.

Figure 3.4 shows the 10-90% burn duration for the speed and stroke data. Combustion durations were dramatically shorter for higher equivalence ratios, and were somewhat smaller for lower engine speeds. The results correlate with expectations based on laminar flame speeds, where higher equivalence ratios will yield higher flame speeds. Higher engine speeds are also associated with higher turbulence levels which may further increase flame speeds.

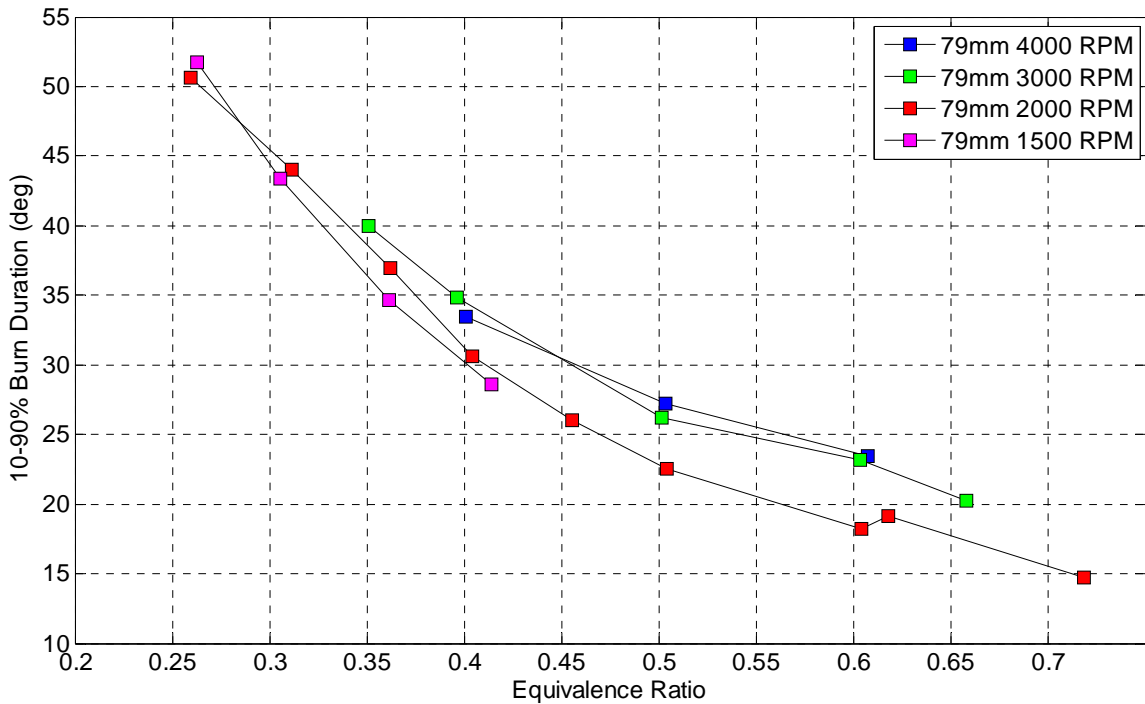


Figure 3.4: Burn duration as a function of equivalence ratio.

Although the coolant flow rate was not recorded, pump settings for each experiment were fixed at constant values throughout testing, and coolant flow rates were not expected to vary dramatically. As a consequence, the temperature change of the coolant flow in and out of the engine can be informative about the heat transfer for the different engine operating conditions. The increase in coolant temperature is shown in Figure 3.5. The temperature

rise across the engine increased dramatically with higher equivalence ratios and engine speed.

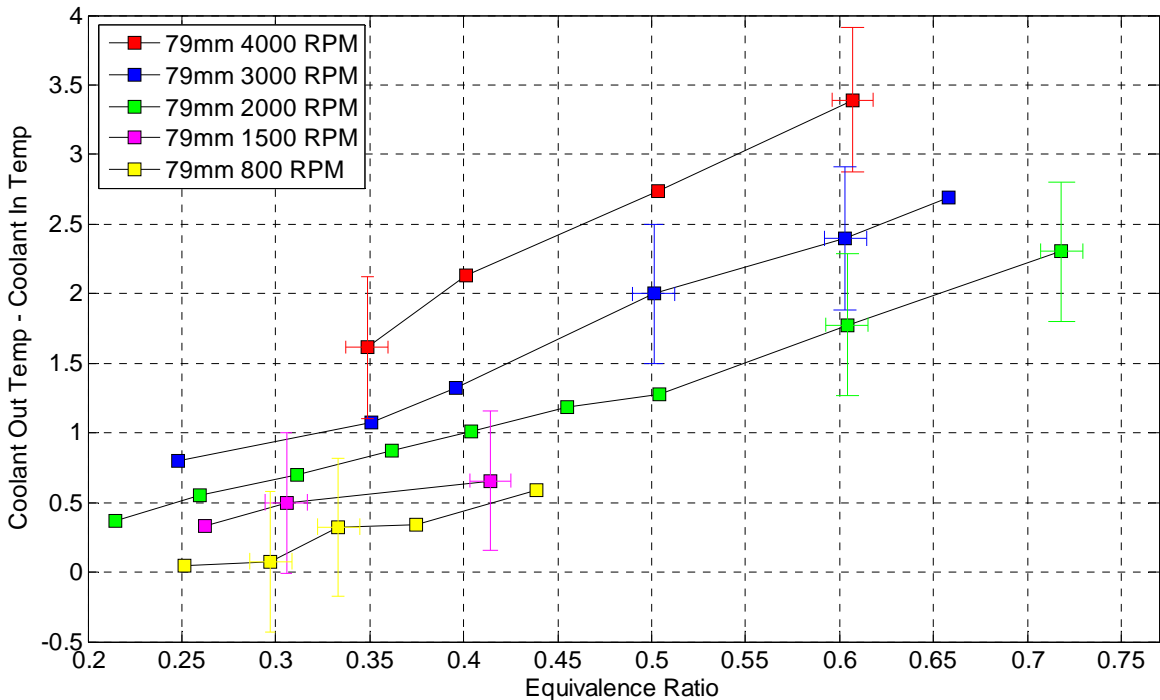


Figure 3.5: Increase in coolant temperature as a function of equivalence ratio.

The pumping losses (presented as the pumping mean effective pressure, PMEP) for the engine speed and stroke tests are shown in Figure 3.6. PMEP was determined using the in-cylinder pressure time histories in the manner described in Section 2.7. The total mass flow rate into the engine of air and hydrogen for the corresponding data is presented in Figure 3.7. The pumping losses increased dramatically with engine speed and showed a slight dependence on equivalence ratio. This dependence is anticipated to be primarily due to the slightly lower total mass flow rates at higher equivalence ratios, as seen in Figure 3.8.

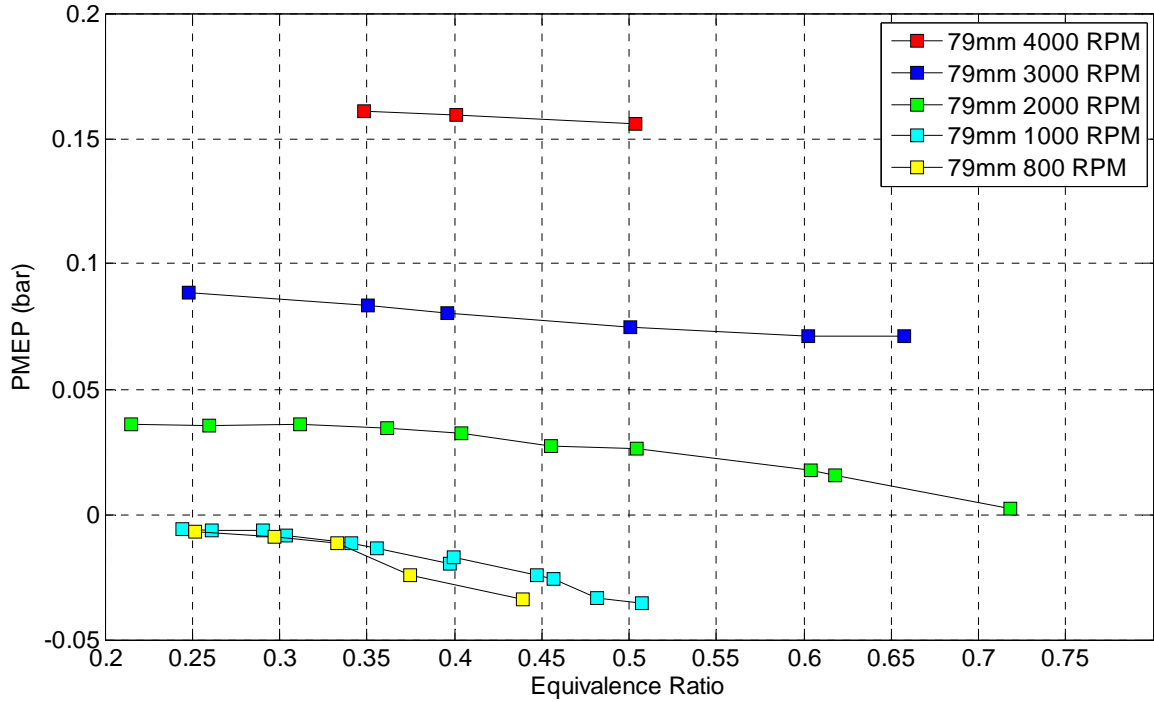


Figure 3.6: PMEP as a function of equivalence ratio.

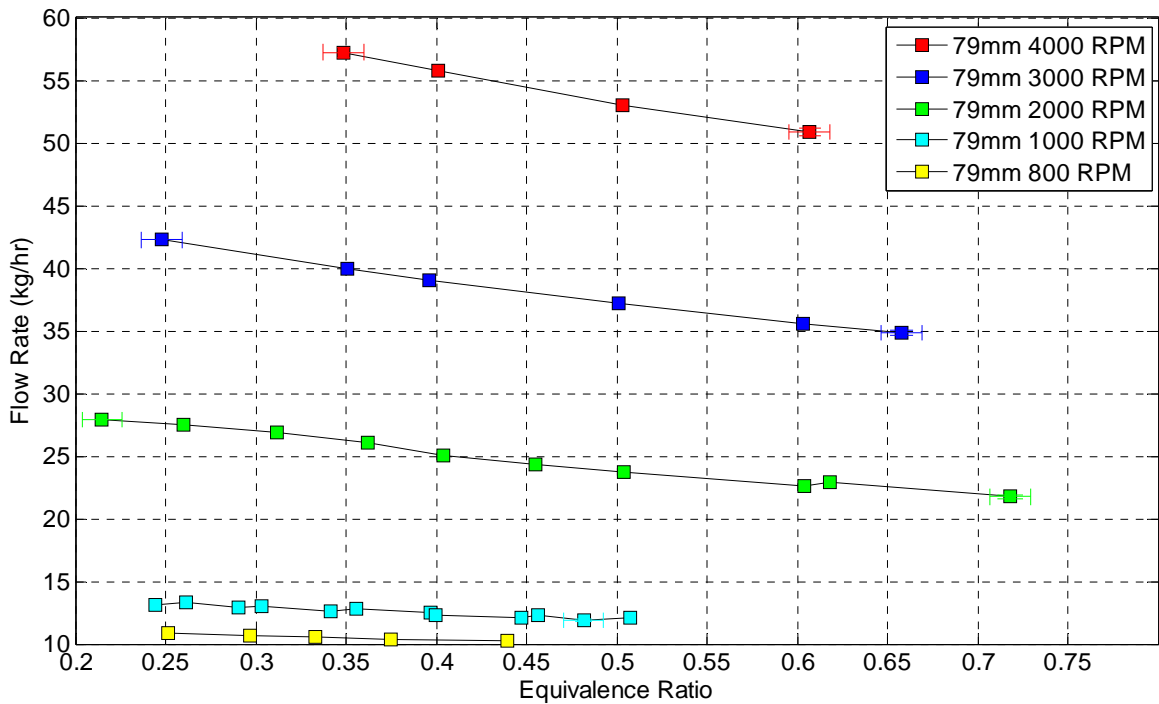


Figure 3.7: Total mass flow rate into engine as a function of equivalence ratio.

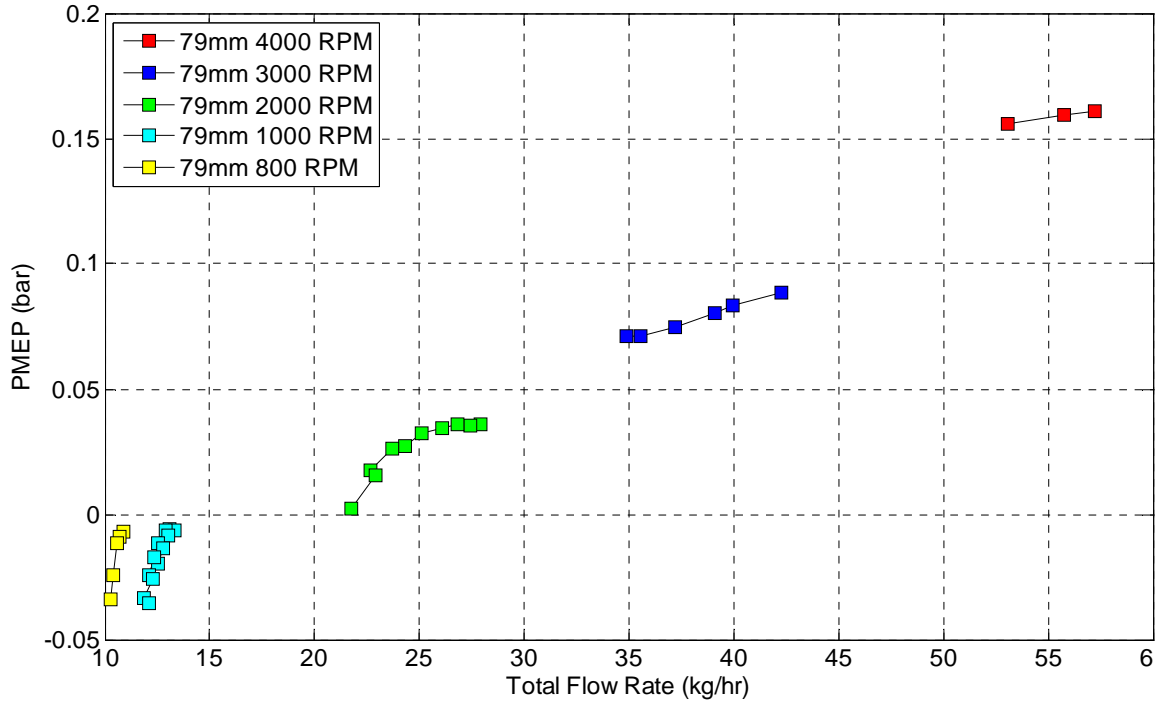


Figure 3.8: PMEP as a function of total mass flow rate into engine.

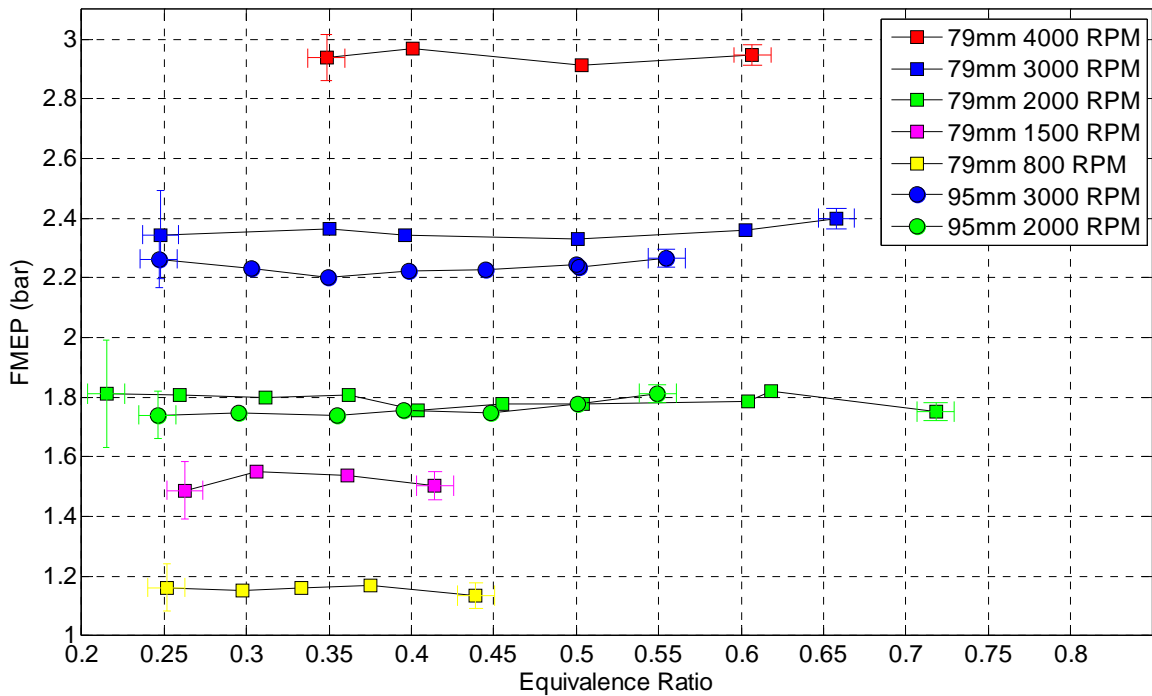


Figure 3.9: FMEP as a function of equivalence ratio.

In Figure 3.9, the friction mean effective pressure (FMEP) of the single cylinder engine is shown as a function of equivalence ratio. Recall, the FMEP was determined by subtracting the observed brake mean effective pressure from the net IMEP. The FMEP was approximately constant with equivalence ratio, but varies dramatically with engine speed. For all engine speeds, the friction was high due to the single-cylinder balancing mechanism, and as such the friction should not be considered indicative of a multiple-cylinder implementation.

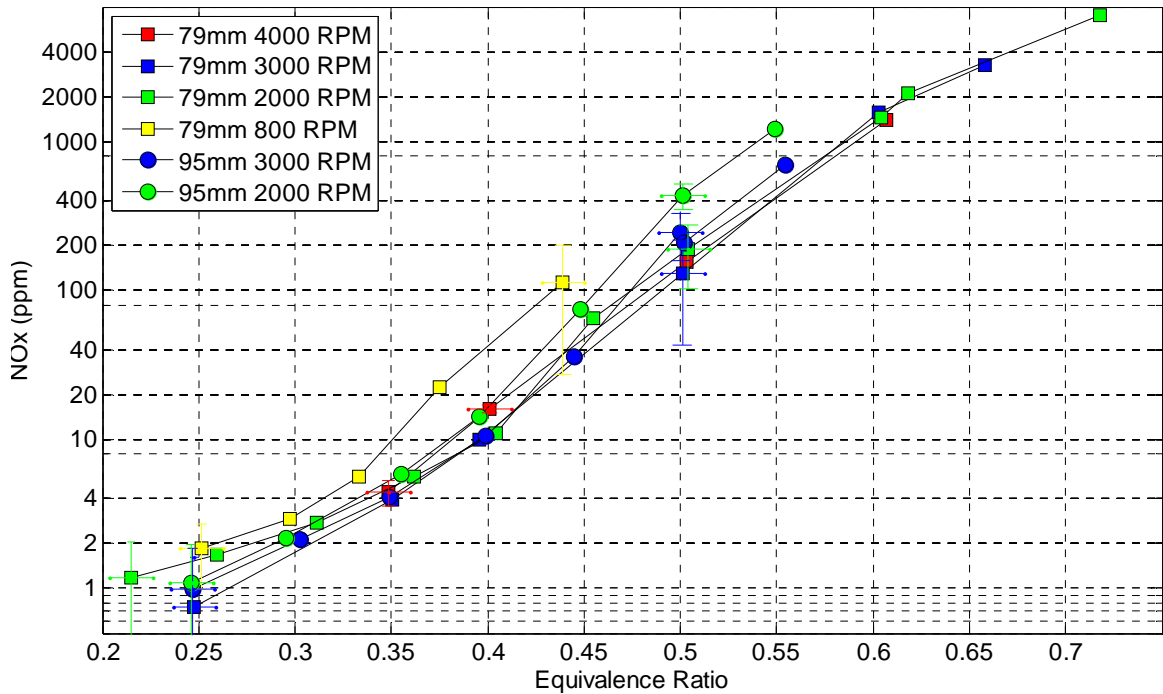


Figure 3.10: NO_x as a function of equivalence ratio.

Figure 3.10 presents the NO_x data for the different engine speed and stroke tests. The NO_x emissions increase by over two orders of magnitude as a function of equivalence ratios. As the in-cylinder temperature varies widely with large changes in equivalence ratio, the amount of NO_x emitted was strongly a function of equivalence ratio. In the range of $\phi = 0.35$ to 0.6, the logarithm of NO_x has a roughly linear trend with equivalence ratio. There was some reduction in NO_x with the faster characteristic times of the higher engine speeds.

3.3 PI Engine Efficiency as a function of Compression Ratio

With a high autoignition temperature, hydrogen-fueled engines are expected to use higher compression ratios than similar gasoline engines. The efficiency of a fuel-air cycle with constant-volume combustion is shown for varying compression ratios and equivalence ratios in Figure 3.11. Equilibrium chemistry and gas properties were predicted using the Canterra software package and the GRI 3.0 reaction mechanism as published by Smith et al. [33]. Although the reaction rate coefficients for that software package were optimized for natural gas, the instantaneous combustion shown here would be unaffected. The efficiency at any given compression ratio decreases as equivalence ratio increases; primarily due to the inferior ratio of specific heats encountered at higher temperatures.

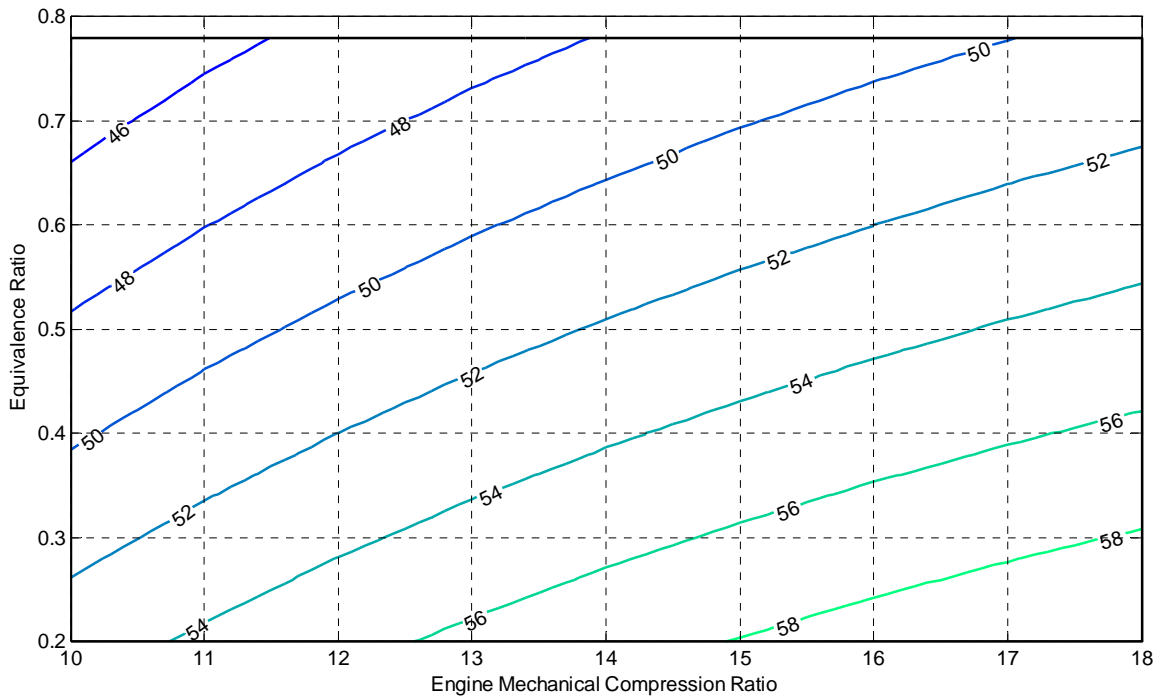


Figure 3.11: Efficiency of theoretical Otto-cycle engine with varying equivalence ratios and compression ratios.

In such an analysis, higher compression ratios will unequivocally prove superior; however, in actual implementation, factors such as autoignition limits, combustion chamber geometry, engine friction, and engine mechanical constraints will all limit the highest practical compression ratio. In order to understand some of these limits, several experiments were conducted where the compression ratio was varied by changing the deck height of the engine. Details of the engine configuration and operating parameters are shown in Table 3.2.

	Value	Unit
Engine Speed	2000	RPM
Intake Manifold Pressure	100	kPa
Exhaust Manifold Pressure	100	kPa
Equivalence Ratio	0.2-0.6	Phi
Bore	89.04	mm
Stroke	95	mm
Compression Ratio	12-15.7	
Ignition	Dual Side	
Injector	PFI	

Table 3.2: Engine Design and Operating Parameters for PI Compression Ratio Studies.

The ideal thermal efficiency is contrasted with the observed gross indicated thermal efficiency in Figure 3.12. The expected theoretical efficiency gain from increasing compression ratio from 12.0:1 to 13.7:1 or from 13.7:1 to 15.7:1 is approximately 1.5%. However, at $\phi = 0.4$, increasing from a compression ratio of 12.0:1 to 13.7:1 improved the observed ITE by 1.2%. Increasing the compression ratio from 13.7:1 to 15.7:1 improved the observed ITE by 0.5%.

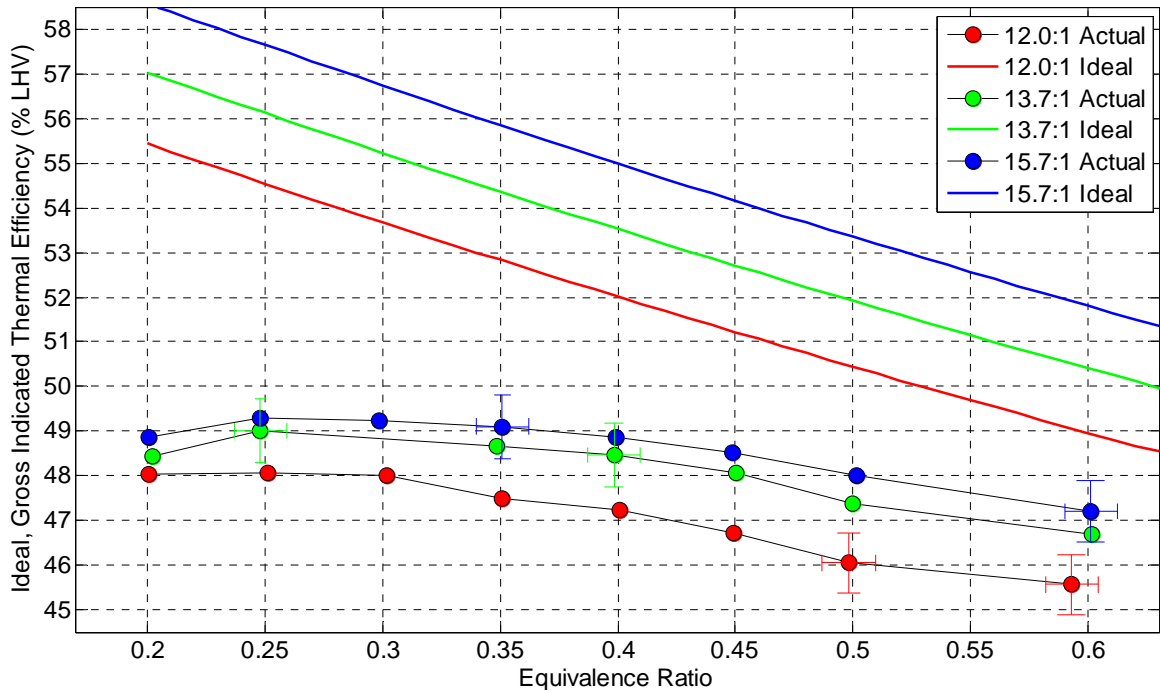


Figure 3.12: Comparison of ideal and actual data for thermal efficiency gains with increasing compression ratio as a function of equivalence ratio.

Figures 3.13 and 3.14 present the combustion phasing (crank angle timing of 50% burn) and 10-90% burn duration, respectively. At the conditions tested, the 12.0:1 and 13.7:1 engines were not knock limited, and the 15.7:1 engine was only knock limited at higher equivalence ratios. In addition to the issues that were listed above, some of the other factors that cause the efficiency gain to be less than ideal are poorer combustion phasing at higher compression ratio, shown in Figure 3.13, and slower burn rate, shown in Figure 3.14. Higher equivalence ratios result in faster burn rates, and the higher pressures associated with higher compression ratios result in slower burn rates. The sub-optimal combustion phasing at higher compression ratios occurs when spark timing is retarded in order to avoid autoignition.

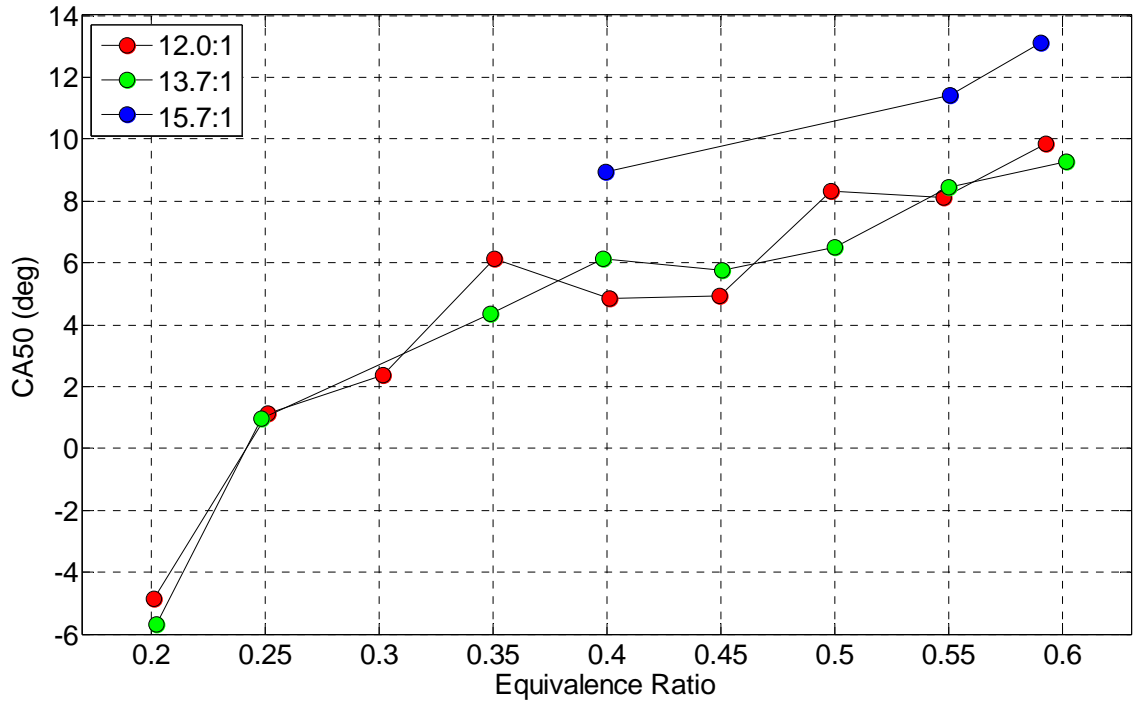


Figure 3.13: Crank angle of 50% burn as a function of equivalence ratio.

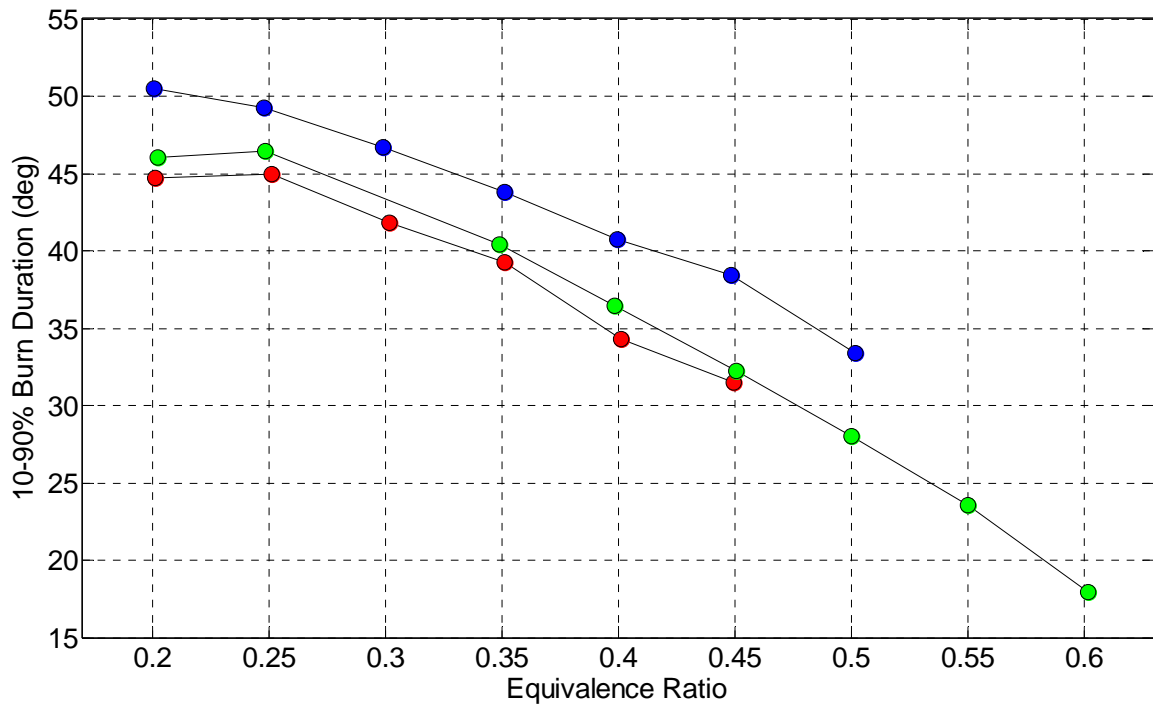


Figure 3.14: 10-90% burn duration as a function of equivalence ratio.

Figure 3.15 shows the effect of pumping on the indicated efficiency by comparing the gross and net ITE. The experiments used unthrottled air, and the pumping losses varied from approximately 1.5% to 2.5%.

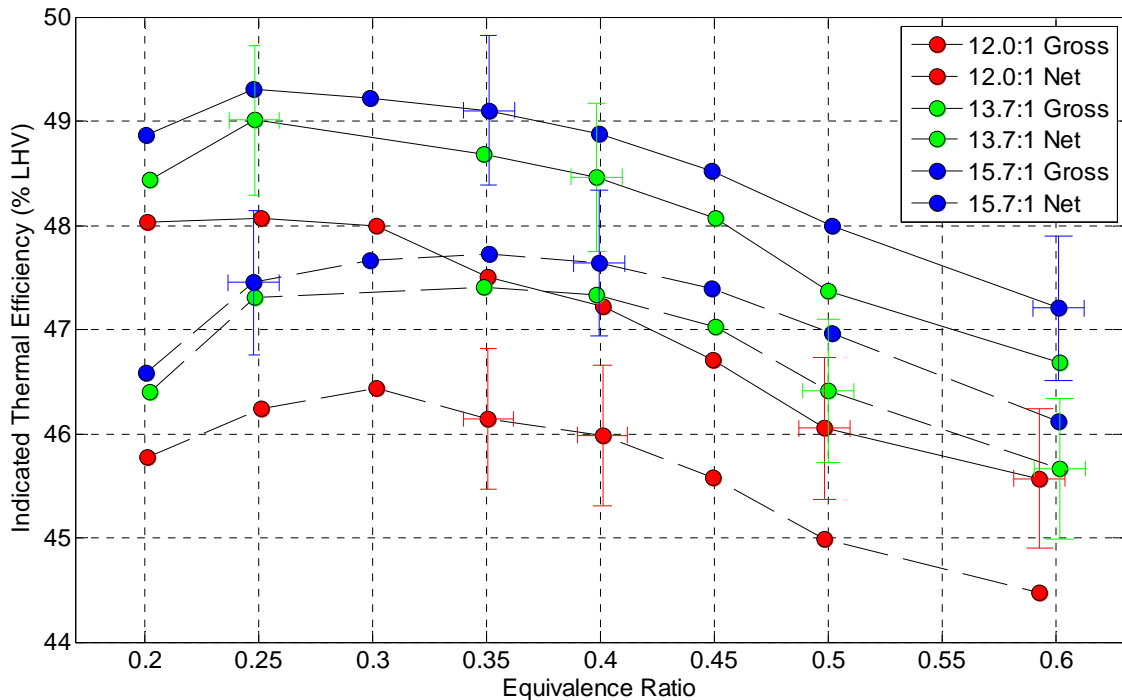


Figure 3.15: Gross and Net Indicated Thermal Efficiency as a function of Equivalence Ratio.

Figure 3.16 shows the brake thermal efficiency (BTE) as a function of equivalence ratio. Care should be taken when interpreting these data, as the FMEP of the single cylinder engine and auxiliary balancing mechanism under these conditions was quite high; as seen in Figure 3.21. The FMEP was 2 bar for the 12.0:1 case, but increased with higher equivalence ratios and higher compression ratios by as much as 0.15 bar. In engines where friction has been optimized, FMEP might be as low as 0.5 bar for the 12.0:1 engine, but would be expected to increase with the higher compression ratios. As the balancing mechanism was fairly isolated from the cylinder loads, it would be expected that the friction of the 15.7:1 engine would increase by approximately 0.15 bar in a multi-cylinder engine. This would result in an engine with a 13.7:1 compression

ratio having slightly superior BTE when compared to a 15.7:1 engine, even though the ITE of the 13.7:1 engine was slightly inferior.

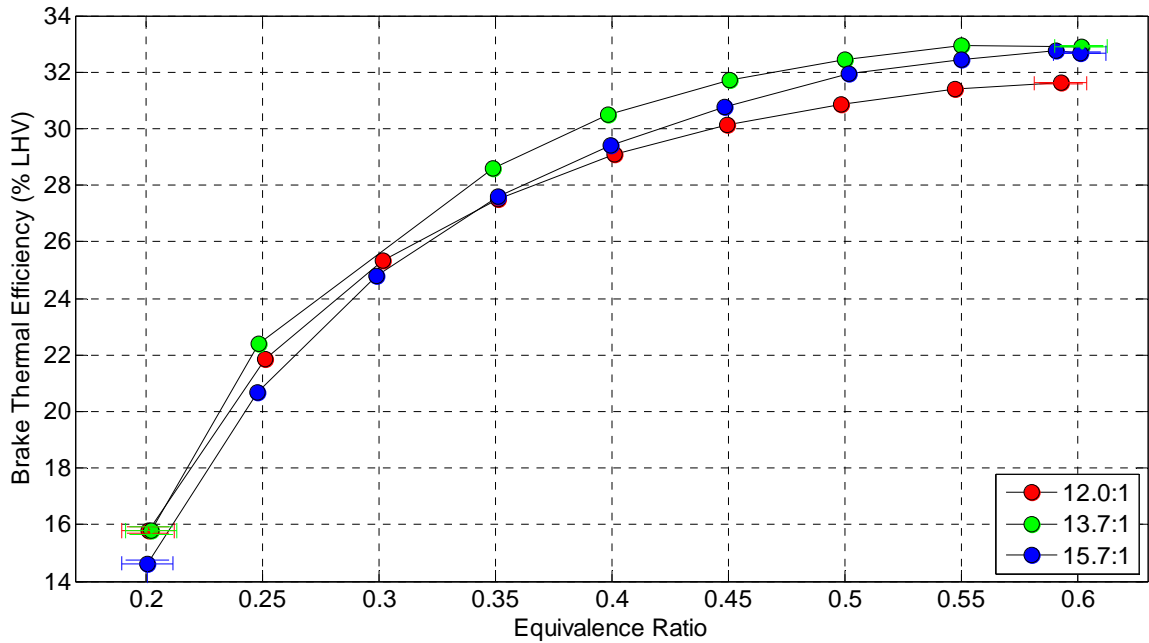


Figure 3.16: Brake thermal efficiency as a function of equivalence ratio.

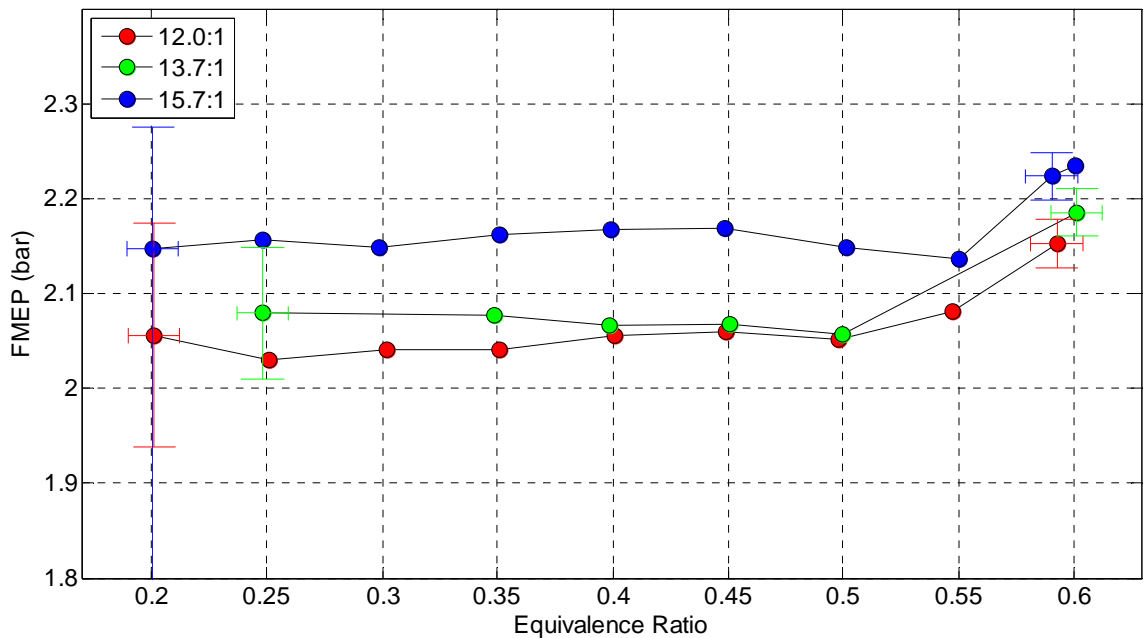


Figure 3. 17: FMEP as a function of equivalence ratio.

3.4 DI Engine Efficiency of as a function of Intake Manifold Pressure

Maximizing specific power will allow smaller displacements and the reduction in friction that accompanies engine downsizing. If the inlet pressure is increased, the ratio of surface area to cylinder charge mass is improved as well, which minimizes heat transfer to the cylinder wall. Since hydrogen engines have very high autoignition temperatures, they are particularly well suited to turbocharged operation.

In these experiments the effects of varying intake manifold pressure are presented. The engine design and operating parameters are shown in Table 3.3. The engine speed was fixed at 3000 RPM. Intake manifold pressure varied from 35 to 200 kPa, and exhaust manifold pressure varied from 100-200 kPa. All pressures above atmospheric resulted from artificial pressurization of the intake system or artificial restriction of the exhaust system. For all of the tests in this section, the 13H direct in-cylinder injector was used to fuel the engine.

	Value	Unit
Engine Speed	3000	RPM
Intake Manifold Pressure	35-200	kPa
Exhaust Manifold Pressure	100-200	kPa
Equivalence Ratio	0.4	Phi
Bore	89.04	mm
Stroke	79	mm
Compression Ratio	11.7	
Ignition	Central	
Injector	13H	

Table 3.3: Engine Design and Operating Parameters for DI Boosting Studies.

The operating conditions tested were separated into three groups, which are shown in Figure 3.18. In order to generate low intake manifold pressures, the engine was heavily throttled. Above 100 kPa, two pressure schedules were tested. In the first, referred to as the 'high backpressure (BP) turbo', a standard

turbocharger was approximated, and the intake manifold pressure was equal to exhaust manifold pressure. In the second, referred to as the 'low backpressure (BP) turbo', a variable geometry turbocharger was approximated, and the exhaust backpressure imposed on the engine was 20 kPa less than the intake manifold pressure imposed. Near atmospheric pressures, this schedule is optimistic, but at higher loads it approximates the results seen on a 2.3L turbocharged engine with variable geometry turbine (VGT).

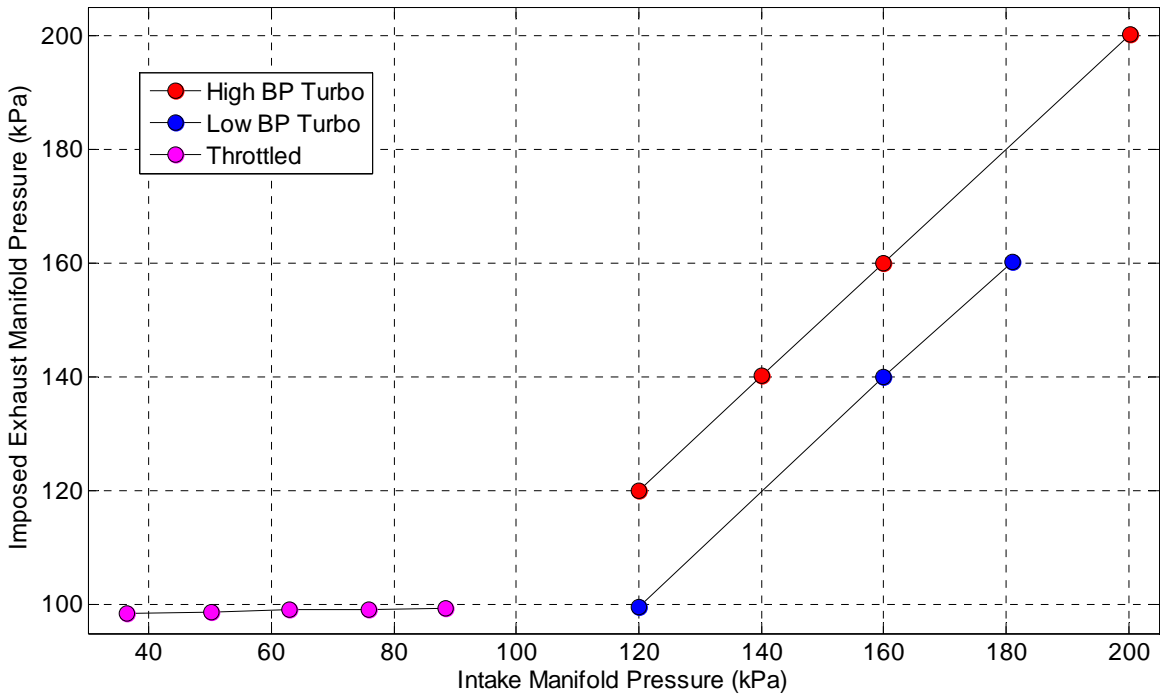


Figure 3.18: Pressure schedule used in boosting studies of DI hydrogen engine.

The results for gross and net ITE are shown in Figure 3.19. With the pressure schedule that approximates a higher backpressure turbo, the pumping losses resulted in a loss of about 1% in absolute efficiency. With the pressure schedule that approximates a VGT, there was no loss due to pumping. As expected, there was a large discrepancy between gross and net efficiency in the throttled condition. In general, between 3.5 bar and 14 bar, increasing manifold

pressure improved the gross thermal efficiency of the engine by approximately 0.21% per bar IMEP.

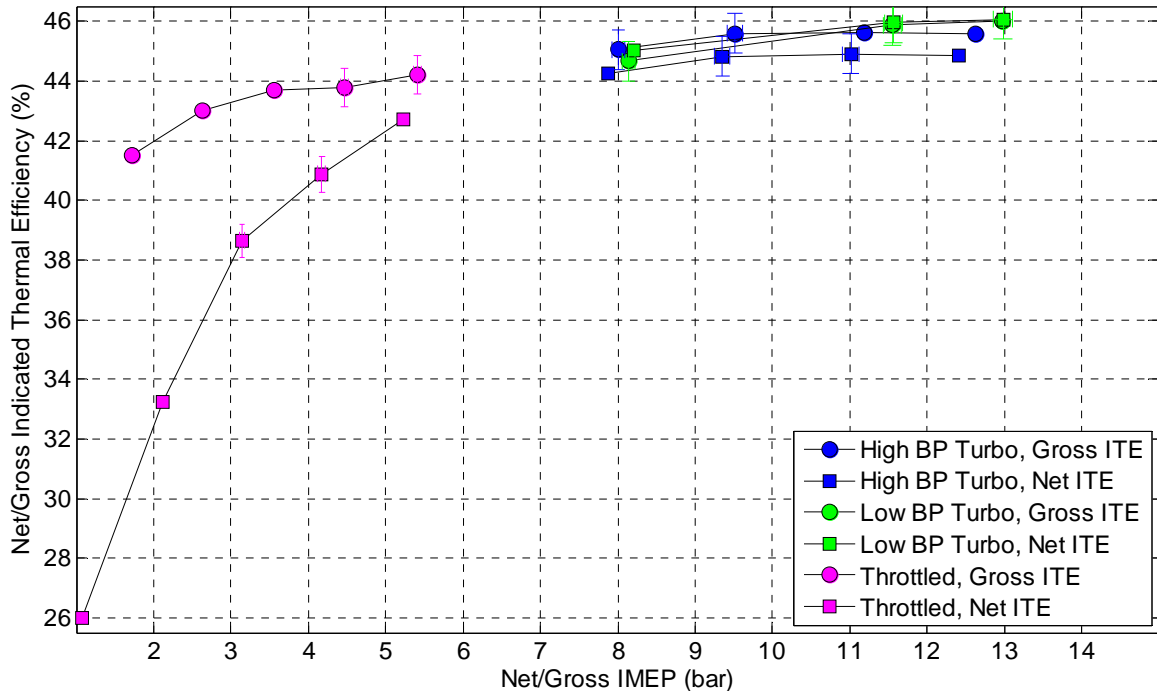


Figure 3.19: Gross and net ITE as a function of IMEP.

The 10-90% combustion duration data are shown in Figure 3.20. The burn duration required for optimal operation increased as the inlet/combustion pressure increased. This is expected, because at lower pressures, hydrogen reacts with oxygen in a two-term, fast reaction; and at higher pressures, hydrogen reacts with oxygen in a three-term, slower reaction. The peak pressures, including average peak pressure and the sum of the peak pressure and three standard deviations, are shown in Figure 3.21. Peak pressure increased from 18 bar at a 35 kPa inlet pressure, to 105 bar with a 200 kPa inlet pressure.

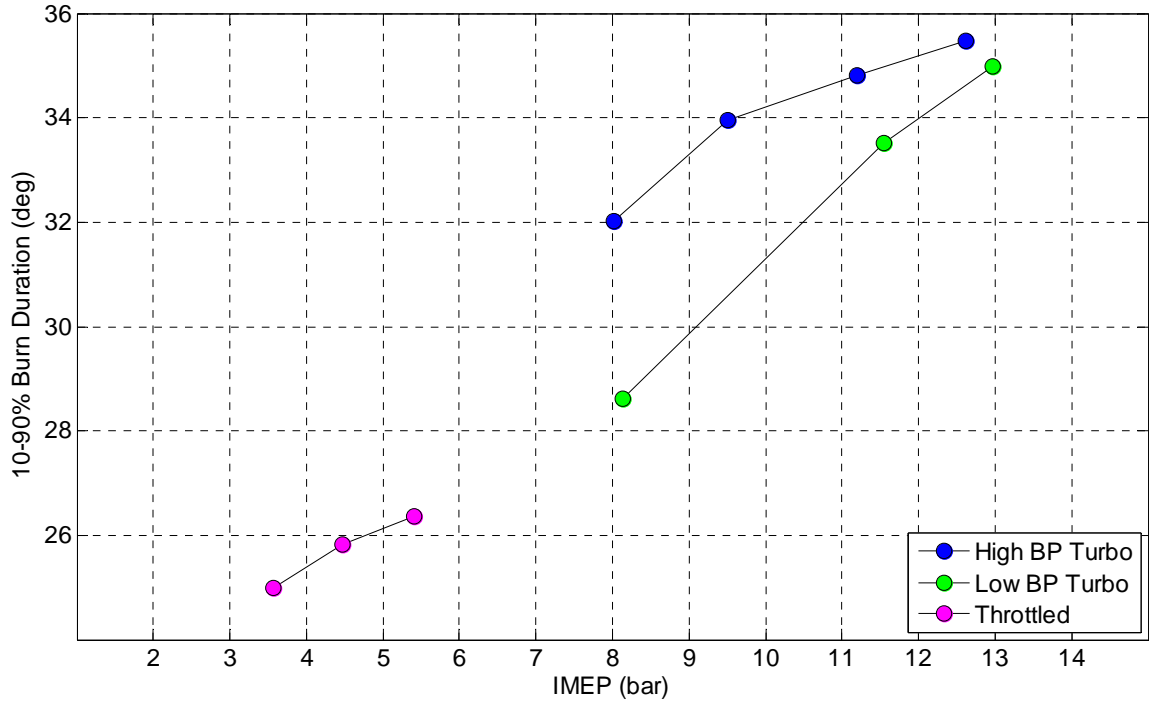


Figure 3.20: Burn duration as a function of IMEP.

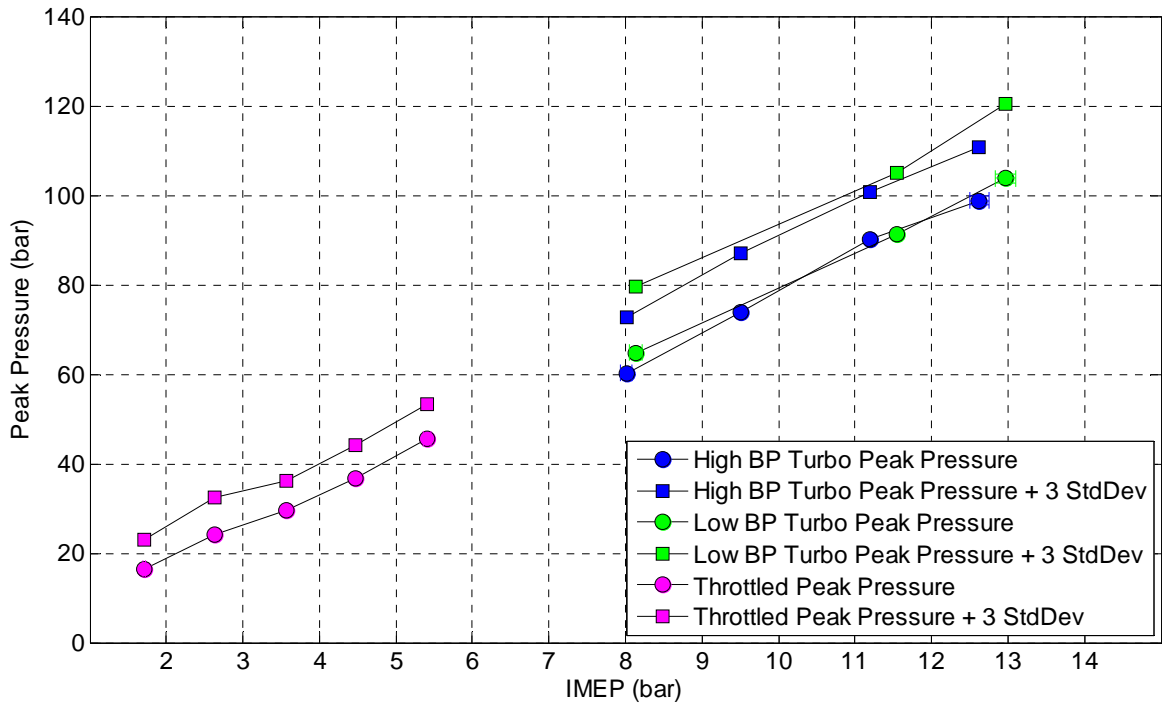


Figure 3.21: Peak pressure as a function of IMEP.

3.5 Theoretical Potential for Pneumatic Recovery in a DI Hydrogen Engine

Many implementations of hydrogen engines are envisioned to store the hydrogen in a high-pressure tank. Late injection of fuel into the cylinder can allow for some conversion of the energy stored pneumatically in the fuel tank into shaft work. The tests conducted in this work never exceeded an injection pressure of 120 bar, and tests were generally conducted at 110 bar. At 110 bar, the energy that could be extracted by an ideal turbine is 2.7% of the LHV of the fuel. Although the magnitude of the pressure recovery effect is expected to be smaller than the advantage found in controlling fuel distribution via optimal injection timing, it would still be instructive to separate and compare the efficiency gain due to the two effects.

It is difficult, however, to experimentally determine the magnitude of the pressure recovery effect. The timing of the fuel injected affects the local fuel distribution and local temperature of the mixture. Fuel injection timing also affects the work done on the mixture by the piston during the compression stroke. These factors, in turn, affect combustion speed, combustion temperature, and pressure during the expansion stroke.

To provide a preliminary understanding of these effects, a model was created of the engine cycle to determine the maximum expectation of pressure recovery. As the model was intended to be interpretive, rather than predictive, many simplifying assumptions were invoked. The equivalence ratio assumed was $\phi = 0.4$. Injection was treated as adiabatic (i.e. Joule-Thomson expansion) and no consideration was given to mixing time – i.e. the fuel-air charge was assumed to instantaneously mix to a homogeneous condition.

Combustion was modeled as a constant volume process. For the purpose of estimating pneumatic recovery, there was negligible difference between a

model of complete combustion, a model of reaching chemical equilibrium at each timestep, and a model which reached equilibrium at TDC only and maintained species concentration through the expansion stroke. The results shown here modeled equilibrium at TDC only.

Engine dimensions, when required, were set to those in the experimental engine. Injection pressure and temperature of the hydrogen was 110 bar and 298 K, respectively. Although these assumptions are not adequate for a predictive model, they are of sufficient fidelity to approximate the maximum recoverable pneumatic energy.

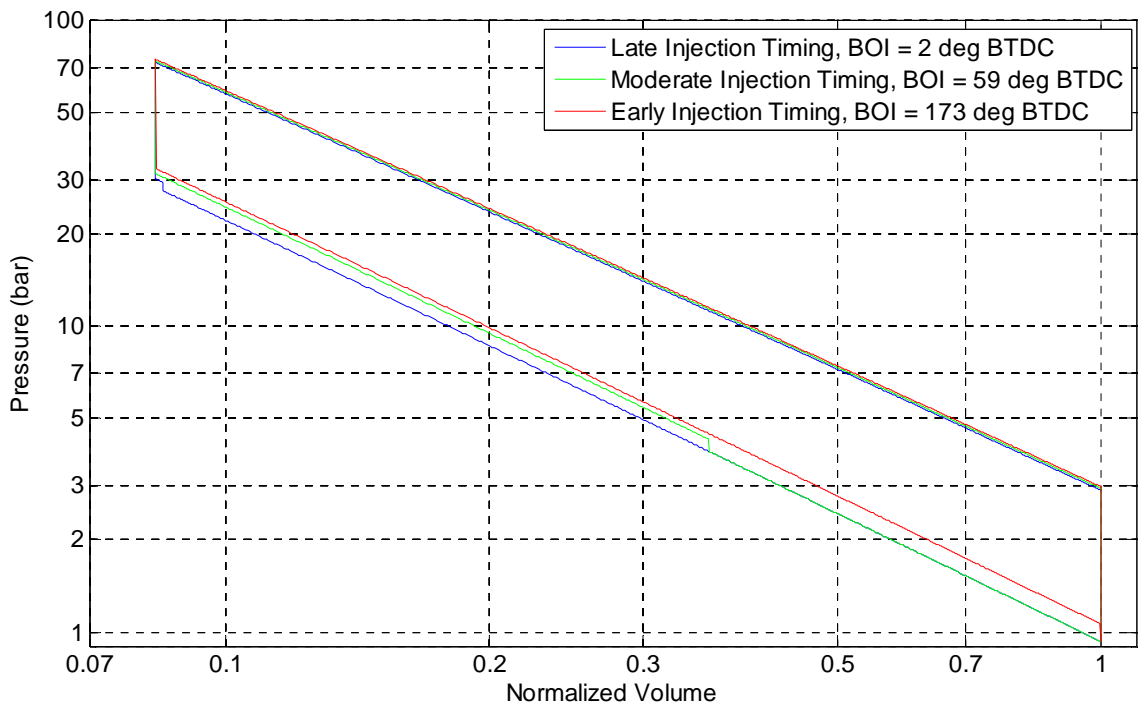


Figure 3.22: pV diagrams for theoretical constant volume combustion with direct injection of hydrogen at different injection timings.

Three pressure-volume (p-V) diagrams correlating to these assumptions are shown in Figure 3.21. The conditions are shown to illustrate the differences seen in the cylinder pressure due to in-cylinder injection of hydrogen at $\phi = 0.4$.

The late, moderate and early injection timings correspond to 2 degrees BTDC, 59 degrees BTDC, and 173 degrees BTDC, respectively.

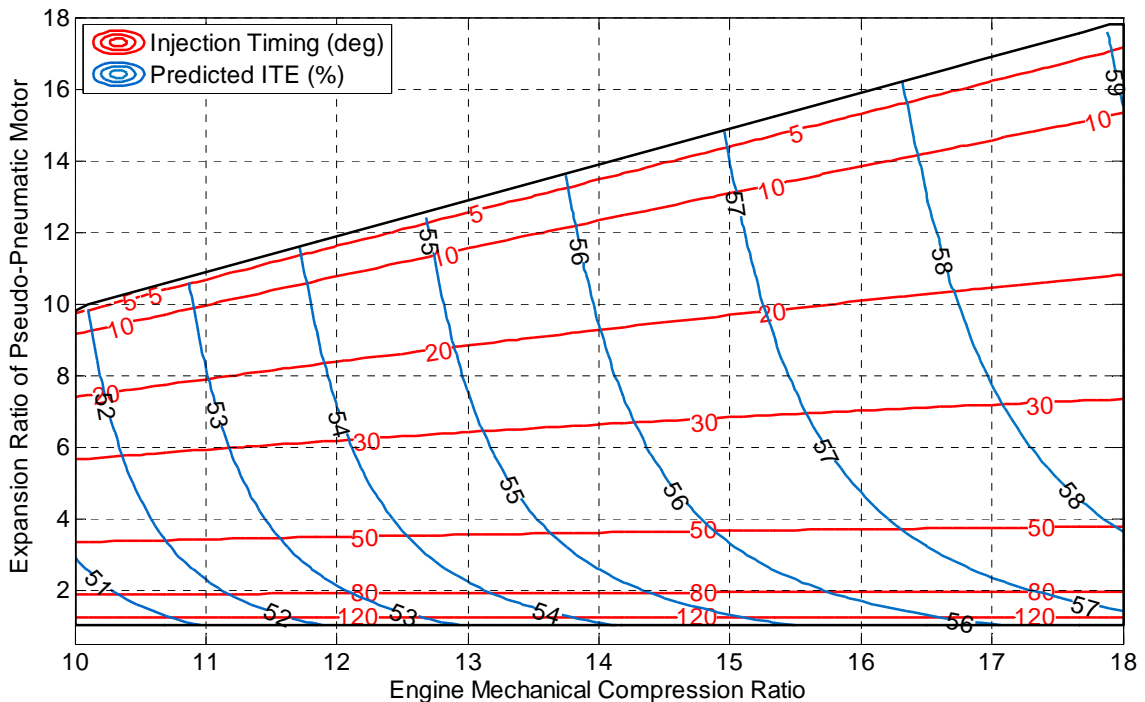


Figure 3.23: Efficiency of a modified fuel-air Otto-cycle that accounts for post-IVC injection of hydrogen fuel.

The expected efficiency with these assumptions is shown in Figure 3.22, charted as a function of both the mechanical compression ratio of the engine and the effective expansion ratio of the 'pneumatic motor'. The expansion ratio (ER) is defined as

$$ER = \frac{V_I}{V_{BDC}} \tag{Equation 3.1}$$

Where V_I is the injection volume and V_{BDC} is the total volume when injection occurs. For convenience, the corresponding injection timing is also shown. At 12:1 compression ratio, the efficiency of the engine when injecting fuel at top dead center (TDC, 0 CAD) is 54.3%. When the fuel is injected at bottom dead center (BDC, 180 CAD), the efficiency of the engine is reduced to 52.2%. When

the fuel is injected at 90 BTDC, with an expansion ratio of a little less than 2, the efficiency only rises to 52.8%. In other words, at typical compression ratios, the pneumatic energy of the hydrogen injected has a maximum effect on ITE of approximately 2% in absolute efficiency units.

3.6 Overview of the Effects of Nozzle Design on DI Engine Efficiency

Of course, the energy benefit from pneumatic recovery is accompanied by advantages in fuel distribution and combustion characteristics. Tests were designed to quantify the effects of combustion characteristics via changes in fuel injection timing. The engine design and operating parameters are shown in Table 3.4. All experiments were conducted at approximately 11.7:1 compression ratio. The injection pressure remained constant at 110 bar. The equivalence ratio was varied from $\phi = 0.2$ to 0.6. Two crankshaft strokes were tested: 79 mm and 95 mm.

	Value	Unit
Engine Speed	3000	RPM
Intake Manifold Pressure	100	kPa
Exhaust Manifold Pressure	100	kPa
Equivalence Ratio	0.2-0.6	Phi
Bore	89.04	mm
Stroke	79, 95	mm
Injection Pressure	110	bar
Injector	Varies	
Compression Ratio	11.7	
Ignition	Central	
Injector	Varies	

Table 3.4: Engine design and operating parameters for DI studies of the effects of hydrogen injector nozzle design.

The design features of the hydrogen fuel injector nozzles considered are provided in Table 3.5. The number of holes varied from 5 to 17. The total flow area was either 1.0 mm² or 1.4 mm².






					
Pattern	5H	12H	17H	17H	13H
Hole Angle wrt Cyl Axis	0/35	40	0/25/40	0/25/40	30
Nozzle Diameter (mm)	0.597	0.326	0.274	0.324	0.313
Total Flow Area (mm ²)	1.4	1.0	1.0	1.4	1.0

Table 3.5: Key Features of the Fuel Injector Nozzles Tested.

The net ITE is shown in Figure 3.24. For the 79 mm crankshaft stroke, efficiencies were determined for the 12H, two 17H, and the 13H injectors. The 12H nozzle had the lowest efficiency, marginally lower than the two 17H injectors. The 13H injector had the highest efficiency for the nozzles tested with the 79 mm stroke. The 13H injector was also tested on the engine with a 95mm stroke at a variety of injection timings. The change in stroke resulted in an improvement in peak efficiency of 1.8%. Compared to the 13H injector, the 5H injector equaled or slightly improved the efficiency throughout the range tested. The peak efficiency of the 5H injector was 0.2% higher than that of the 13H injector.

Figure 3.25 shows the same data plotted against the distance of the piston from TDC. When plotted in this manner, the efficiency trend is closer to linear, and the location of peak efficiency is closer for the 79 mm and 95 mm conditions.

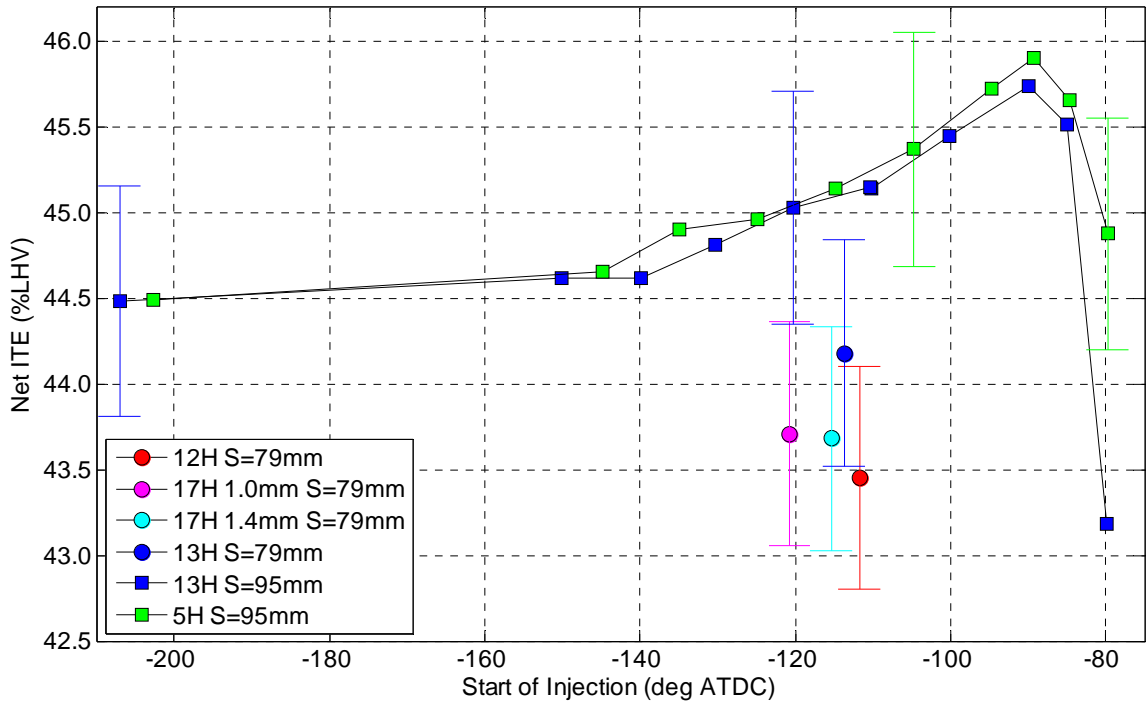


Figure 3.24: Net ITE as a function of start of injection for different H2 fuel injector designs.

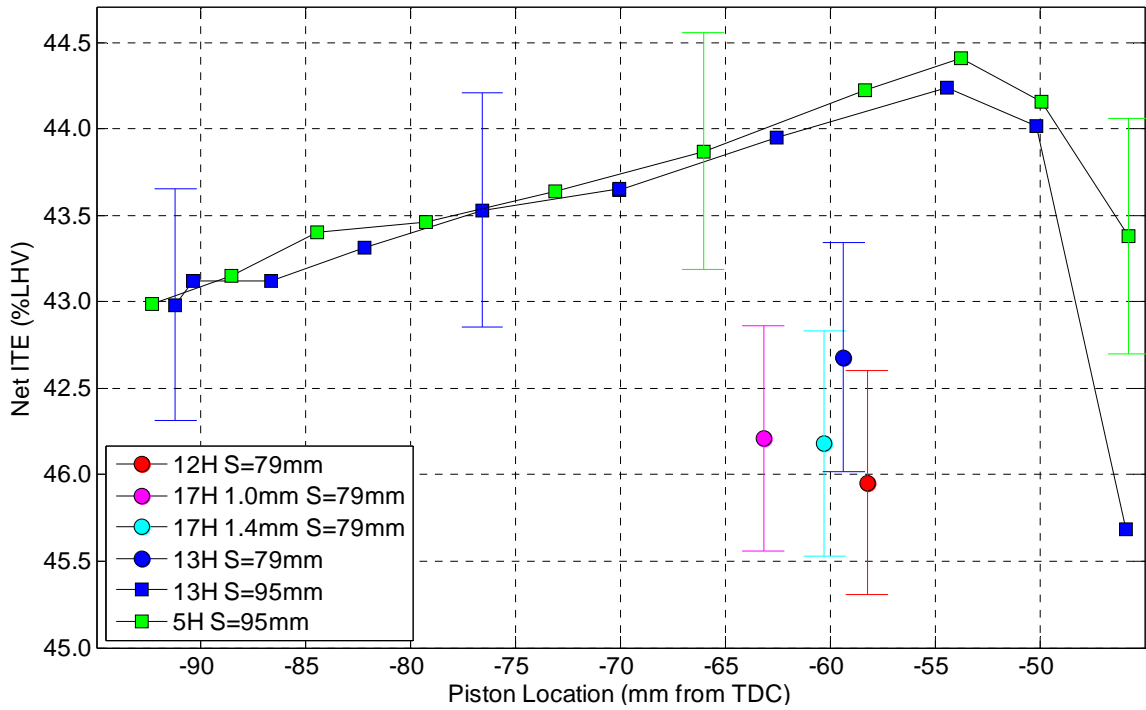


Figure 3.25: Net ITE as a function of piston distance from TDC for different H2 fuel injector designs.

The expected maximum pneumatic recovery of the engine at 90 degrees BTDC injection was expected to be 0.6% (see Figure 3.23). For the 13H injector, the difference in efficiency seen near BDC and that seen at 90 degrees BTDC is 1.12%. The fuel distribution is expected to be advantageous at the 90 degrees BTDC condition. Similarly, for the 5H injector, the difference observed experimentally, 1.25%, is higher than predicted solely based on pneumatic recovery.

The fast decline in efficiency after 90 degrees BTDC can be explained in part by the combustion stability observed. Figure 3.26 shows the coefficient of variation (COV) of IMEP as a function of injection timing. Combustion was quite stable when injection began before 90 degrees BTDC. After 90 degrees BTDC, the fuel distribution was presumably poorly mixed and/or poorly located in the combustion chamber, causing a decrease in ITE.

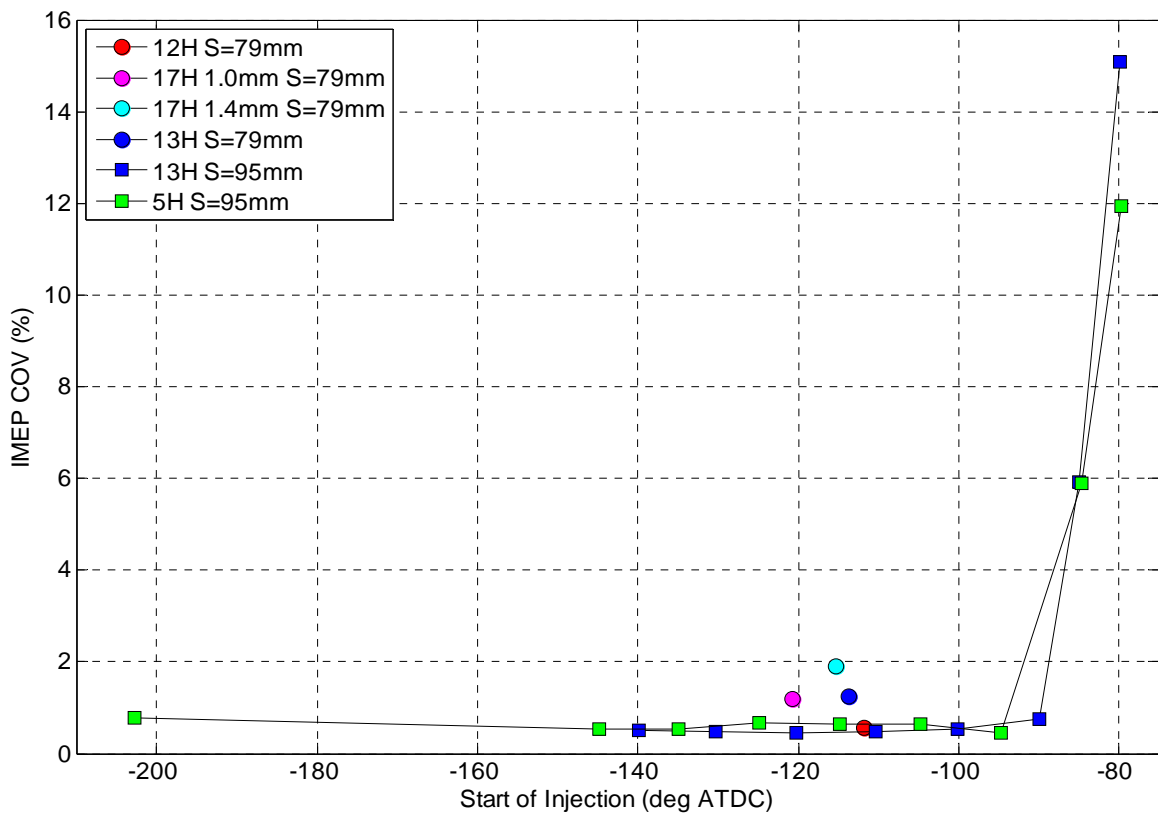


Figure 3.26: Combustion stability as a function of injection timing.

3.7 Summary

The performance results for a single cylinder engine with many iterations of engine design were presented in this chapter. Fuel injection strategies included port and direct fuel injection and 6 different DI nozzles. Engine efficiency data were determined for two crankshaft strokes and three compression ratios. The results for engine efficiency for a range of equivalence ratios, injection timings, and engine speeds were also reported. In general, it was found that:

- The highest net thermal efficiency was found at lean fuel-to-air equivalence ratio conditions of $\phi \cong 0.4$
- Net ITE increased with increasing engine speed by 0.3% of LHV per 1000 RPM from 2000 to 4000 RPM
- A 95 mm stroke compared to a 79 mm stroke improved efficiency by approximately 2% of LHV
- Efficiency was improved by 1.2% of LHV when increasing compression ratio from 12.0:1 to 13.7:1 (out of a maximum anticipated gain of 1.5%)
- Efficiency was improved by 0.5% of LHV when increasing compression ratio from 13.7 to 15.7 (out of maximum anticipated gain of 1.5%)
- While operating at $\phi = 0.4$, increasing manifold pressure improved efficiency by 0.2% of LHV per bar of net IMEP
- With DI injectors, maximum efficiency was reached when injecting between 70 degrees and 120 degrees before TDC
- At the best injection timing of about 90 degrees, efficiency with DI injectors improved by approximately 1.4% of LHV over near-BDC injection

- At an injection timing of 90 degrees and an equivalence ratio of 0.4, the theoretical efficiency gain due to pneumatic recovery is expected to be 0.6% of LHV

These results for engine performance and for the sensitivity of the H₂ engine to operating conditions and combustion chamber design are the baseline for the results of the studies presented in the subsequent chapters of this thesis. The lessons learned from the metal engine studies dictated the best practices for improving H₂ engine performance (Chapter 6), for minimizing NO_x emissions with water injection strategies (Chapters 4 and 5) and motivated the optical engine studies (Chapter 7) to provide direct information on the fuel/air mixing properties at conditions relevant to the metal engine studies.

Chapter 4

Direct In-cylinder Injection of Water into a PI Hydrogen Engine

4.1 Introduction

In order to maximize the hydrogen engine efficiency over a broad range, as for a traditional automobile engine, it is likely that the entire operating regime will remain at equivalence ratios much leaner than stoichiometric. As has been shown, operation at these loads is characterized by high concentrations of both oxygen and NO_x . The NO_x may be difficult to reduce to acceptable levels without increased cost and/or increased fuel consumption; for example, eliminating 50% of NO_x through retarding combustion phasing via ignition invokes a 3% fuel consumption penalty.

As engine displacement and corresponding friction are often scaled by the maximum specific power of an engine, highly loaded regions have an indirect effect on efficiency throughout the operating range of the engine. Since highly loaded points are rarely reached in normal customer operation, increasing maximum load possible, even with a fuel penalty at that load, can decrease overall fuel consumption. For example, Blaxill, et al., estimated that a 20% reduction in engine friction would result in a 4% improvement in EU drive-cycle fuel consumption [34]. The amount of fuel burned at over 90% of full engine load is typically much less than 5% and as such any minor change in fuel

efficiency at high loads can be negligible. Thus, increasing the maximum load possible by 10% would improve drive-cycle fuel consumption by roughly 2%.

In order to allow this type of equivalence ratio increase, the NO_x emitted must be mitigated by some means. One potential strategy is to inject liquid water into the cylinder of an engine. There are several means through which water injection may improve the NO_x emissions of the engine:

1. The water has a large thermal inertia, due to both the evaporative cooling of the water and the large specific heat of water.
2. If the water is injected late into the intake stroke, the evaporation of water will cool the intake charge, which in turn will allow draw more air into the cylinder and further dilute the charge.
3. In addition, there is potential chemical energy storage, as water may decompose at high temperatures and pressures.

A quick analysis of the third subject shows that, at expected pressures and temperatures (2100 K and 50 bar), the dissociation of water at equilibrium is small – with an equivalence ratio of $\phi = 0.4$, the Canterra program predicts that the OH radical will be 0.13% of the mixture. All other radicals are anticipated to be several orders of magnitude less abundant. As a consequence, this work assumes the effect of water dissociation is small and is ignored. The potential of water injection to reduce combustion temperatures, NO_x emissions, peak cylinder pressures, and cylinder pressure maximum rise rates is considered in this work.

4.2 Overview of Experiments

4.2.1 Injectors

For these experiments, hydrogen was injected into the intake port and water was injected directly into the combustion chamber. Some details of the

hardware used are shown in Table 4.1. The hydrogen injector operated at 40 PSI and the water injector was operated at 100 bar.





Cylinder Head	Piston	Hydrogen Injector	Water Injector
Dual Side Ignition, Central Water Injection	15.7:1 with slight dome	Port Injector	Six Hole Symmetric, Direct In-Cylinder
			

Table 4.1: Cylinder head, piston, fuel and water injectors used in in-cylinder water injection studies.

4.2.2 Equivalence Ratio

As was previously discussed, hydrogen engines are usually limited to a maximum equivalence ratio much lower than stoichiometric. The actual equivalence ratio reached is generally dictated by NO_x production, peak cylinder pressure, pressure rise rates, and (the possibility of) anomalous combustion. Current PI hydrogen engines commonly operate at an equivalence ratio at or below $\phi = 0.45$. This operating condition combines minimum fuel consumption and acceptable levels of NO_x, which can be seen in Figures 4.1 and 4.2. Unfortunately, this limits the engine to a net IMEP of approximately 5.3 bar, as can be seen in Figure 4.3. This is a low maximum load when compared with conventional gasoline engines, and many hydrogen-fueled engine designs incorporate large displacement and/or boost systems to improve the MEP.

Higher equivalence ratios would likely require NO_x aftertreatment to meet automotive emissions standards. In order to determine whether operation at higher equivalence ratios without aftertreatment would be possible, the engine was operated with hydrogen injected into the intake port at $\phi = 0.50$. As can be

seen in Figures 4.1 and 4.2, this strategy would consume roughly 64.9 grams/kW-hr (indicated) of fuel and would emit approximately 730 ppm of NO_x.

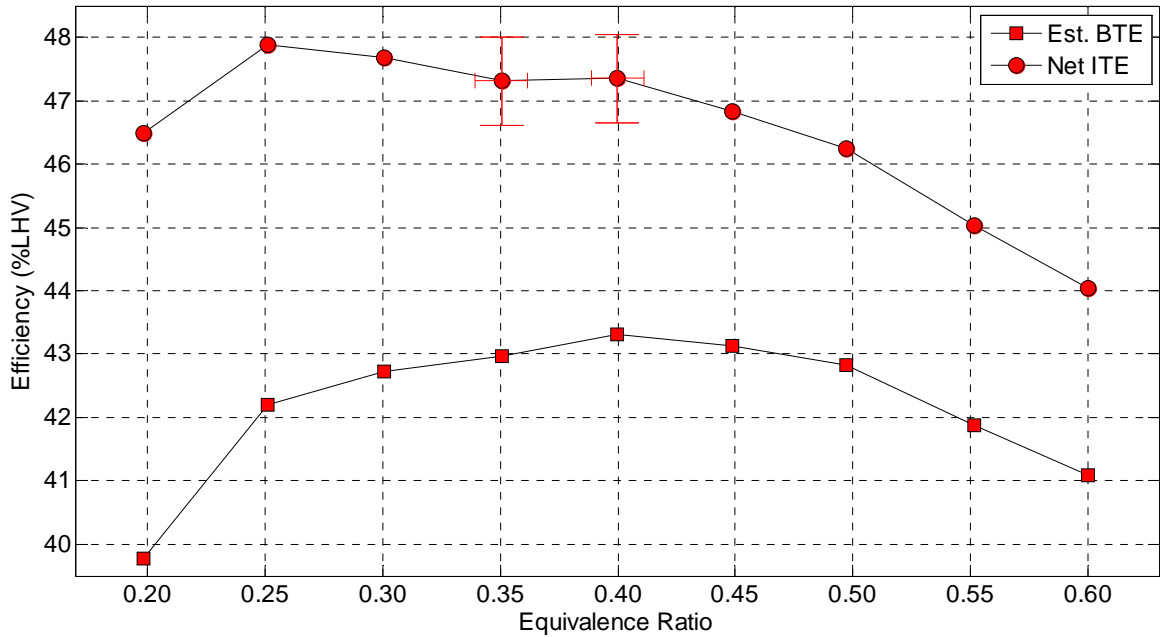


Figure 4.1: Efficiency tradeoff for PI H₂ operation: no water injection.

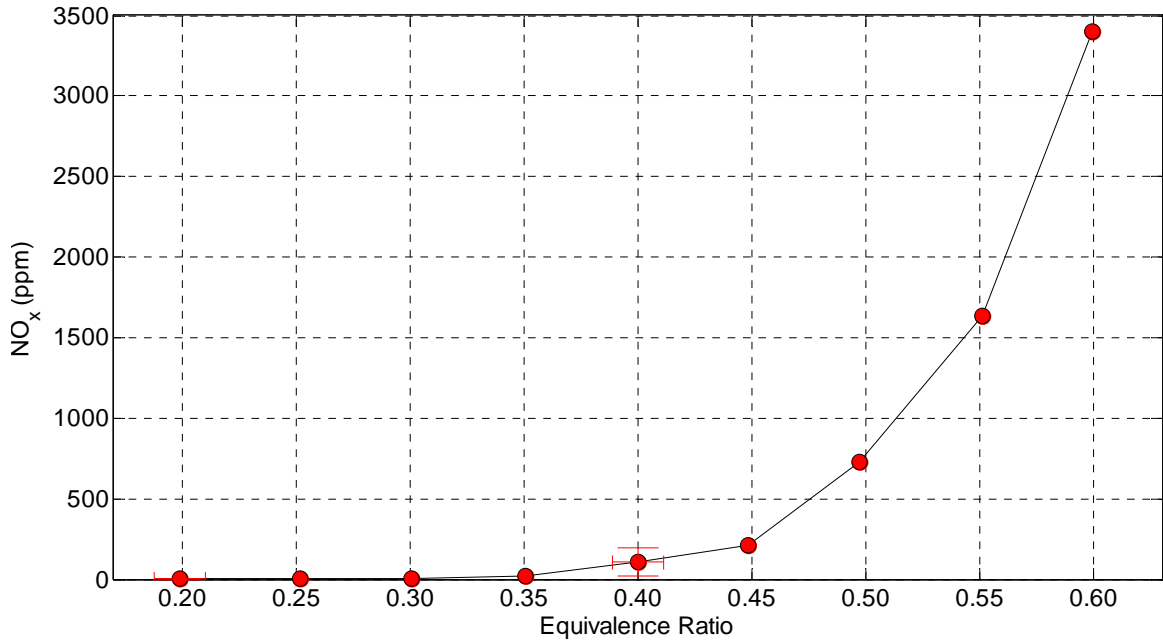


Figure 4.2: NO_x produced during PI H₂ operation: no water injection.

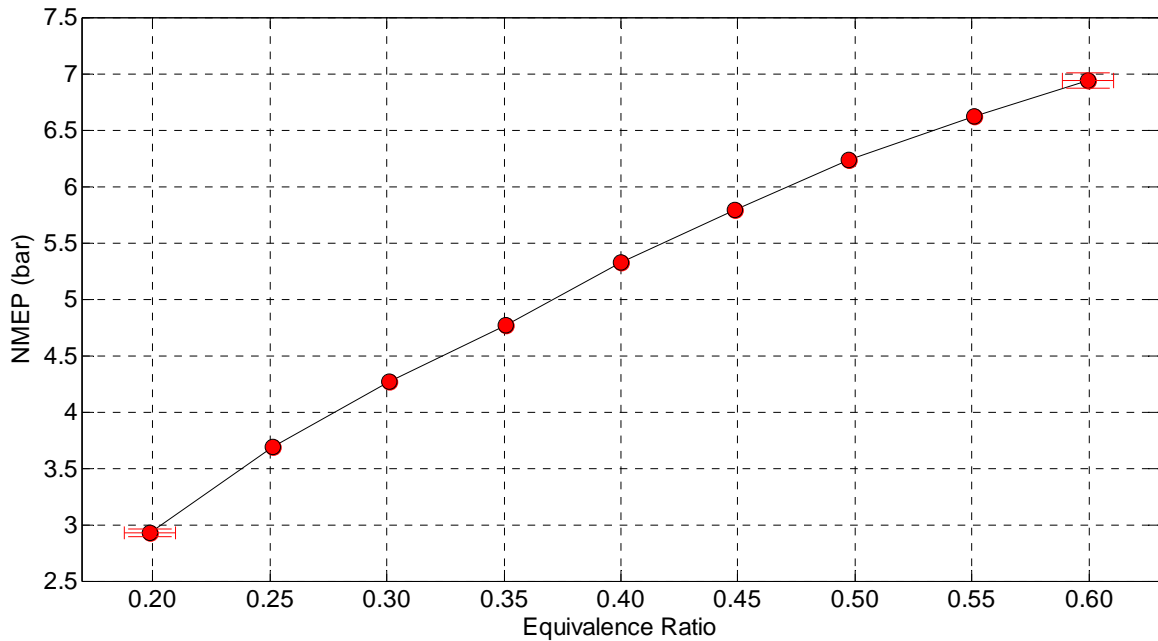


Figure 4.3: Net IMEP as a function of Equivalence Ratio: no water injection.

4.2.3 Experimental Procedure

For each test, the engine was operated at a constant engine speed of 2000 RPM. Air flow was controlled to establish the desired intake manifold pressure. All tests referenced in this chapter were conducted at 100 kPa. Fuel injection pulsewidth was initially set to obtain the desired equivalence ratio. As water was added, minor variations in airflow were observed; nevertheless, the pulsewidth/mass of fuel injected was held constant throughout the test. The amount of water injected was varied by changing the water-injection pulsewidth. The target values for water injection pulse-width were 0, 21, and 35 mg per cycle. The effects of changing the mixing time and evaporation time were investigated by changing the timing of the water injection. At both 21 mg/cycle and 35 mg/cycle, for the majority of the points studied, spark timing was held constant. As the water injection had significant impact on the combustion characteristics, two points of significant interest (-188 and -228 degree SOI with 21 mg/cycle of H₂O) were repeated with a full range of spark timing. Note the

calculations for combustion characteristics do not take into account the introduction of water into the system. The small amount of water (4% of total cylinder mass) is anticipated to have a small effect on the calculations.

4.3 Experimental Results

The performance of the system was strongly dependent on the timing of the water injection into the combustion chamber. Figure 4.4 and 4.5 present the results for the NO_x production and net indicated thermal efficiency (ITE) as a function of the timing for water injection. As is expected, water injection had the largest impact when it was injected prior to combustion. When water was injected during the intake stroke or compression stroke, particularly during the latter parts of the intake stroke, there was a substantial impact on NO_x and ITE. When water was injected during the compression stroke, the NO_x reduction was relatively unaffected by small changes in injection timing. When the water was injected between 45 and 180 degrees ATDC, the majority of the NO_x had already been generated and the effect of water injection on NO_x emissions was minimal. Fuel consumption at these points was relatively unaffected as well. When fuel was injected later in the exhaust stroke (after 270 degrees ATDC), the amount of NO_x produced decreased. This suggests that a substantial portion of the water remains in the residual gas fraction of the next engine cycle, and decreases NO_x generated in the next engine cycle.

At 21 mg/cycle, the NO_x production was reduced to a minimum of 34 ppm when the injection timing was 220 deg BTDC of combustion, suggesting that this injection timing allowed a reasonably homogenous charge of water, fuel, and air when ignition occurred. The net indicated thermal efficiency associated with this point was found to be 43.1%. At 35 mg/cycle, the NO_x production was reduced even further to approximately 13 ppm. The net indicated thermal efficiency associated with this point was 44.5%.

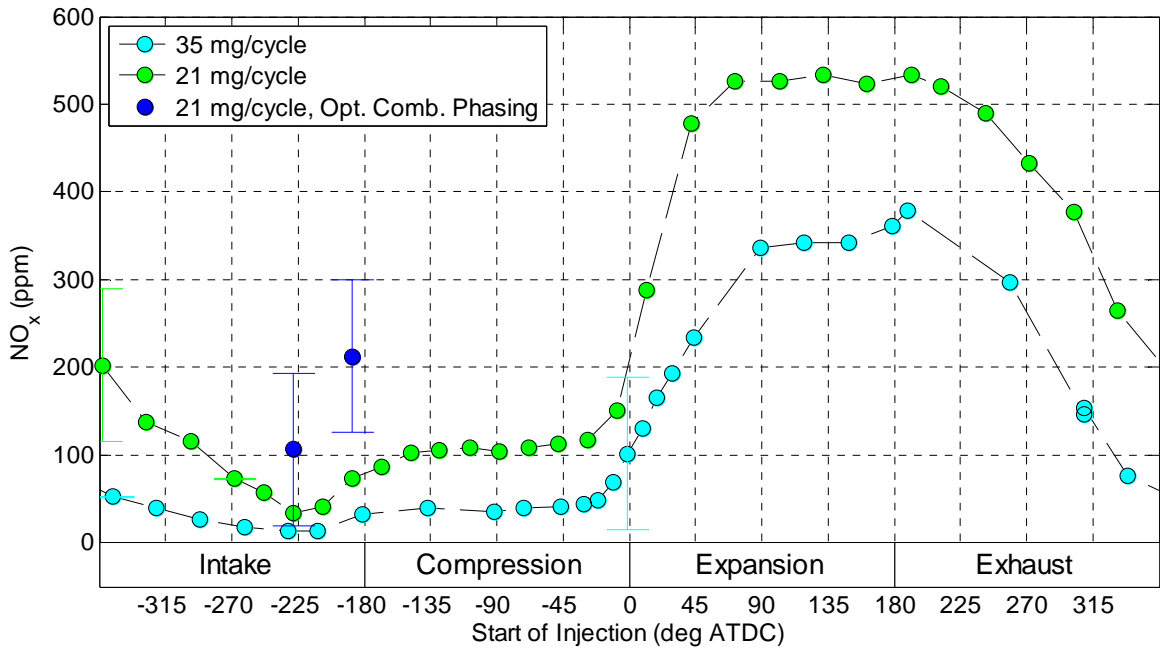


Figure 4.4: NO_x production and net indicated specific fuel consumption as a function of water injection timing.

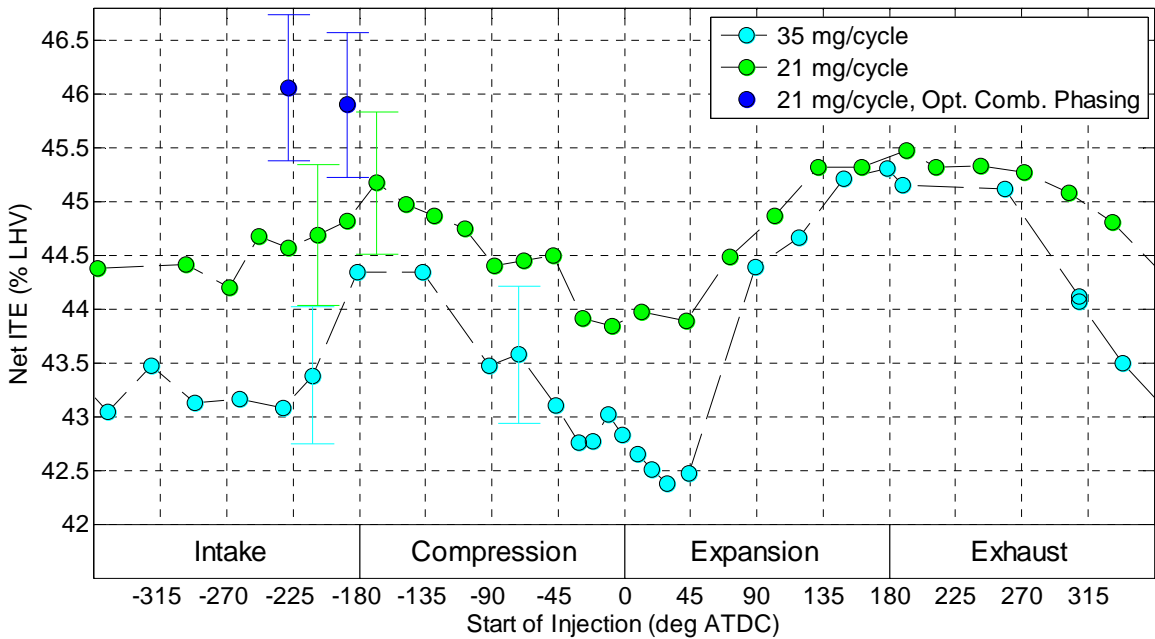


Figure 4.5: Net ITE as a function of H₂O injection angle.

Water injection substantially impacted the calculated 10-90% burn duration and combustion phasing, as shown in Figures 4.6 and 4.7. Recall that no attempt was made to correct the burn rate calculations for the additional

water mass injected into the system. As the spark timing was optimized, the phasing penalty of water injection was substantially reduced and the location of 50% burn was reduced from 22 deg ATDC to 10 deg ATDC. At this condition the specific fuel consumption was reduced to the best observed during the study, but NO_x emissions increased slightly.

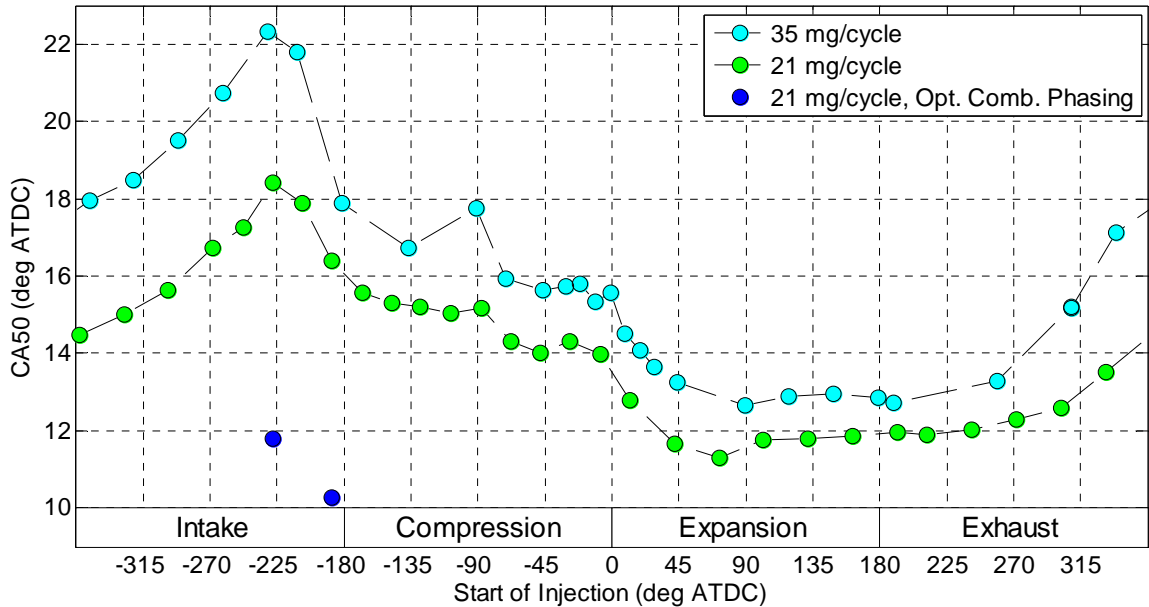


Figure 4.6: CA50 as a function of water injection timing.

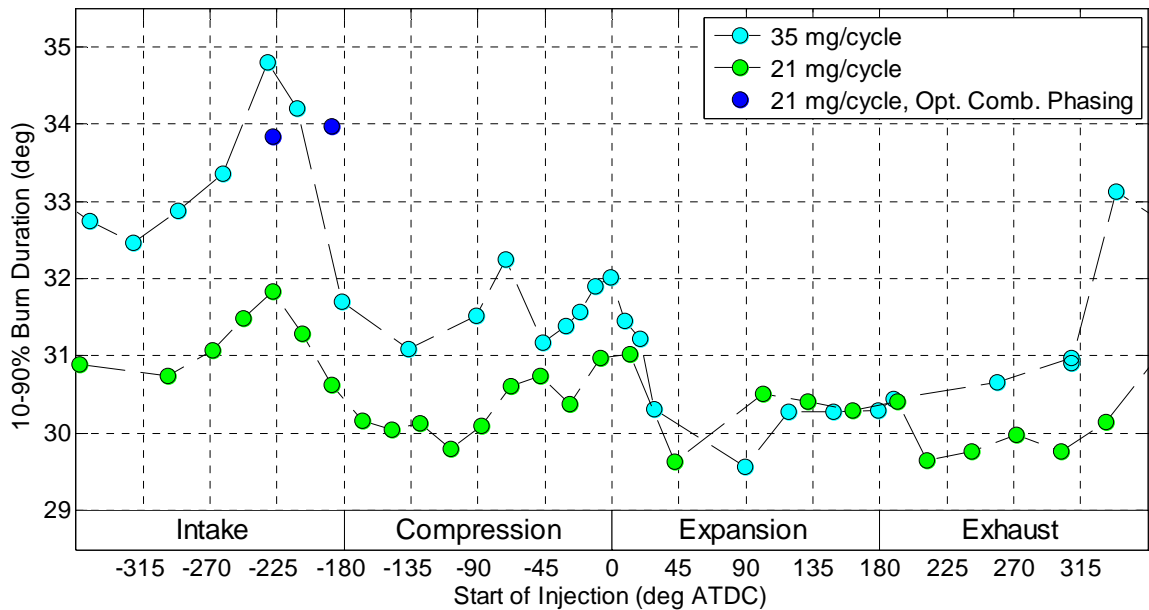


Figure 4.7: Burn duration as a function of water injection timing.

4.4 Analysis and Normalization

Although comparison of these results to similar points without water injection would be enlightening, the small changes in average IMEP with water injection makes it tedious to test all necessary points for direct comparison. The challenge is highlighted in Figure 4.8, in which the specific fuel consumption is charted as a function of IMEP for the conditions previously shown, and is contrasted with a sweep of equivalence ratio when no water was injected. The use of water injection generally reduces IMEP from 6.2 bar to as low as 5.8 bar. Also note that ITE decreases by 0.7 – 4.5 %, depending upon the injection phasing, spark timing, and mass of water injected.

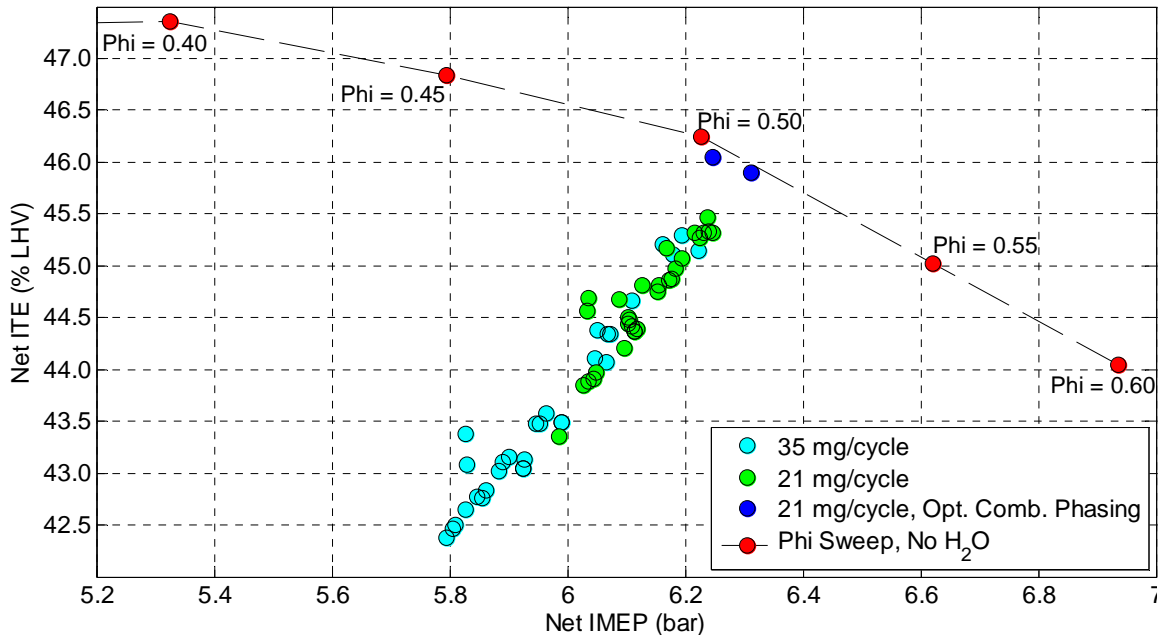


Figure 4.8: Net ITE vs. Net IMEP, comparison of Water Injection and Non-Water Injection.

In Figure 4.9, the results for NO_x emissions are presented as a function of IMEP for the 21 mg and 35 mg water injection conditions. The performance of the engine with varying equivalence ratio is also provided for reference. In almost all cases, the water injection reduces NO_x substantially. It is also clear that comparing the performance of the water injection at a single equivalence

ratio of $\phi = 0.5$ would over-estimate the ability of water injection to minimize NO_x production. As such, the appropriate methodology is to compare NO_x production at equivalent IMEP.

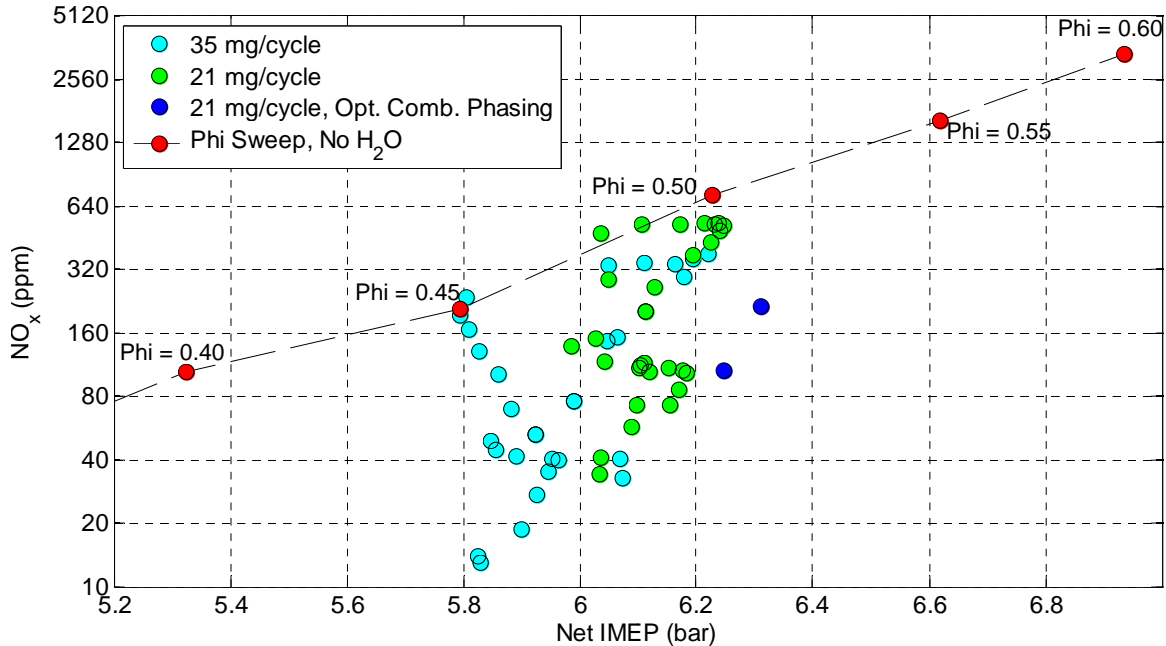


Figure 4.9: NO_x emissions as a function of IMEP for water injection conditions and baseline conditions with no water injection (labeled Phi Sweep).

In order to compare the data with and without water injection using IMEP as the reference variable, we need to understand the correlations between NO_x and IMEP and ISFC and IMEP. The engine data without water injection was used to develop the correlations. For the case of NO_x an exponential was used of the form:

$$NO_x = A \cdot e^{B \cdot IMEP} \quad \text{Equation 4.1}$$

Error was minimized when A was set to $6.5252 \cdot 10^{-4}$ and B was set to 2.2252. These values resulted in an R² value of 0.990. Comparisons between the regression and the experimental data are shown in Figures 4.10 and 4.11, on logarithmic and linear scales, respectively.

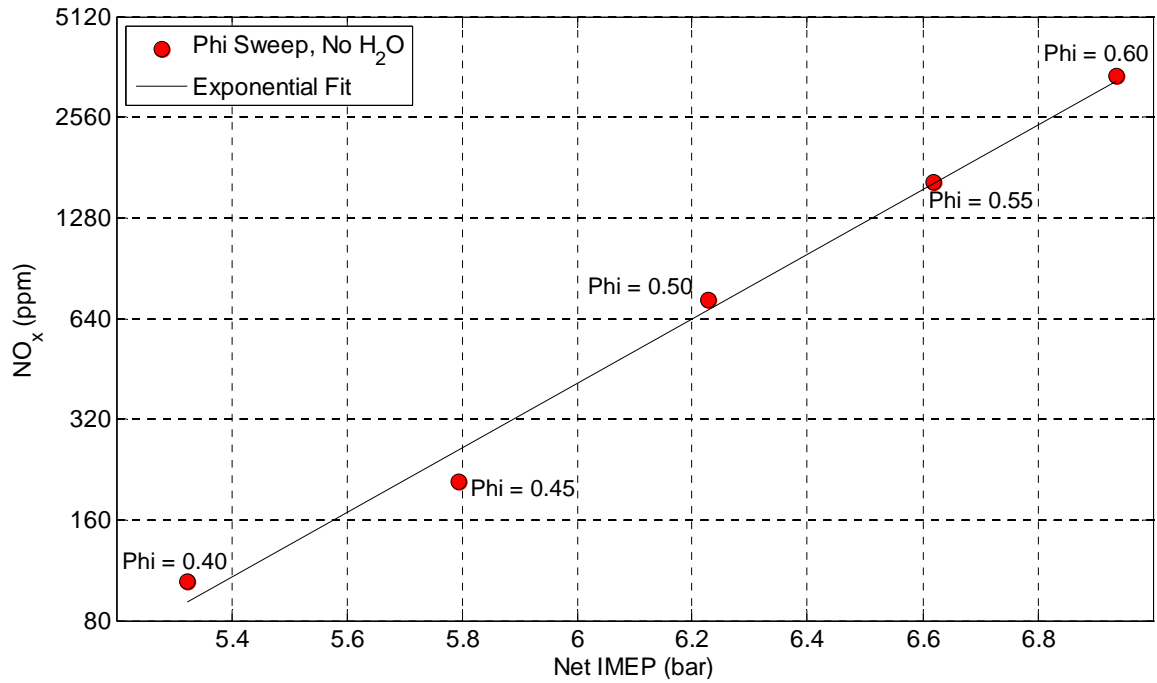


Figure 4.10: NO_x as a function of IMEP for conditions without the use of water injection (logarithmic scale). Symbols are experimental data. Solid line is the fit of Equation 4.1.

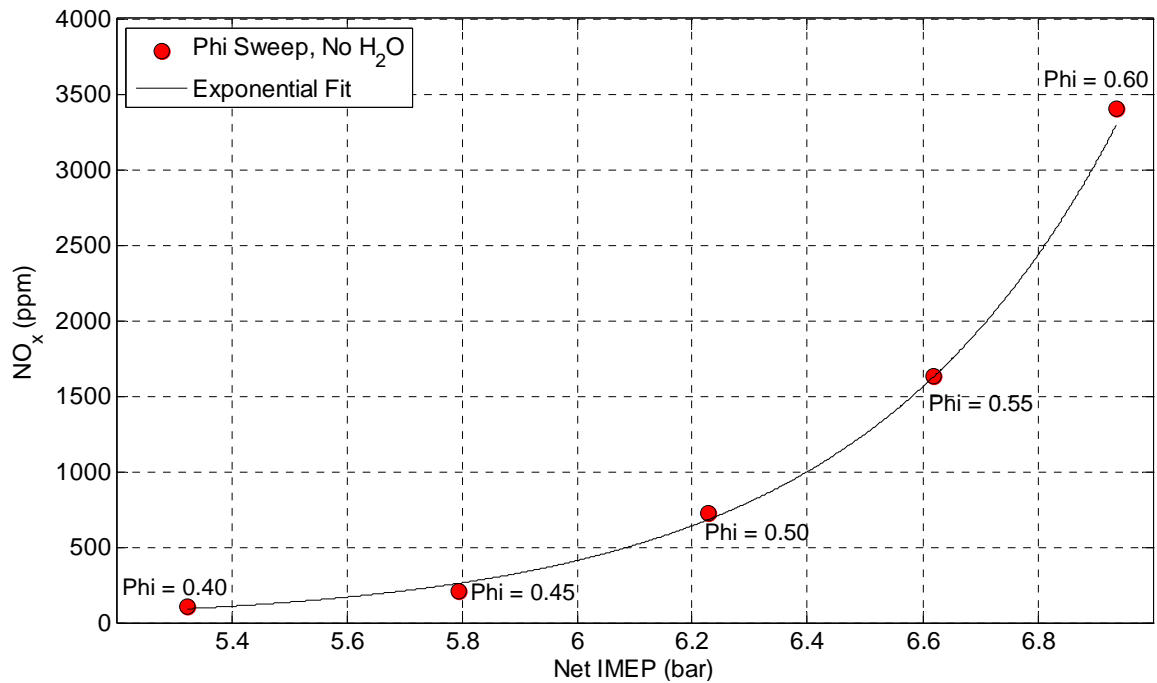


Figure 4.11: NO_x as a function of IMEP for conditions without the use of water injection (linear scale). Symbols are experimental data. Solid line is the fit of Equation 4.1.

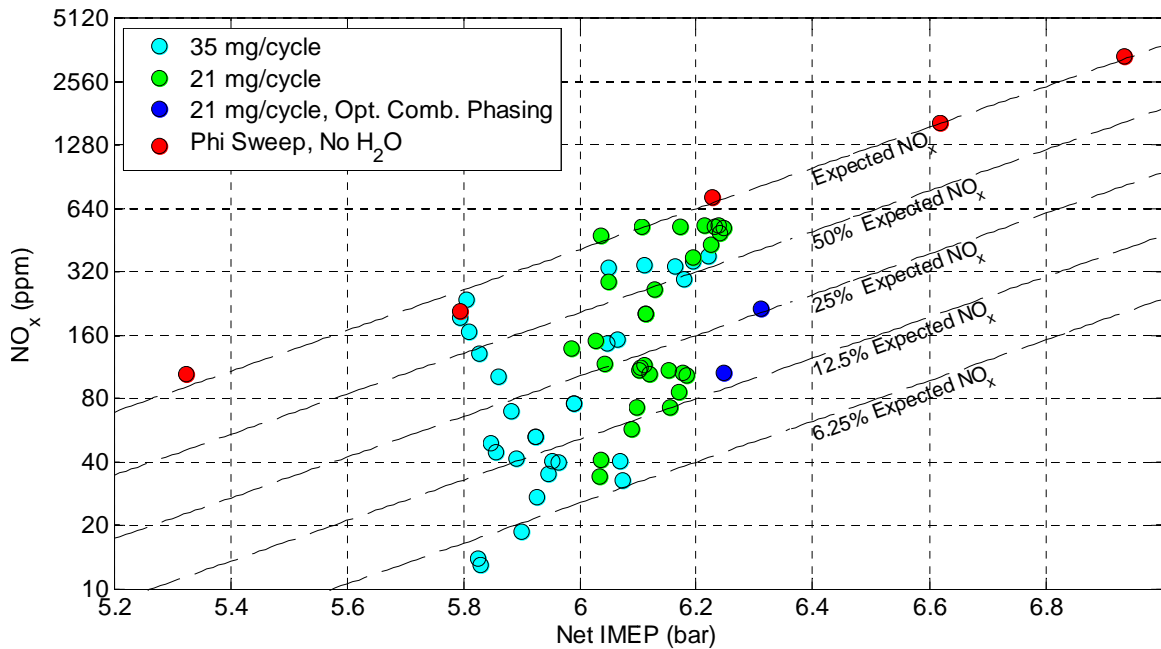


Figure 4.12: Predicted and Actual NO_x levels, with and without water injection.

Figure 4.12 shows predicted NO_x emissions as a function of net IMEP for the conditions with and without water injection. Figure 4.12 also shows trend lines for 50%, 25%, 12.5%, and 6.25% of the NO_x levels expected using the no-water-injection conditions as the baseline. As seen in Figure 4.12, there are several water injection timings (i.e. SOI) that achieve better than 87.5% reduction in the reference NO_x emissions, using either level of water injection.

A similar analysis was conducted for fuel consumption, and the results for the regression are provided in Figure 4.13. For ITE, a second order polynomial was used to fit the data:

$$ITE = A \cdot IMEP^2 + B \cdot IMEP + C \quad \text{Equation 4.2}$$

Error was minimized when $A = -0.9682$, $B = 9.8393$, and $C = 22.34$, with IMEP in units of bar. For the best-fit values, the R^2 was 0.996. As seen in Figure 4.10, injecting water decreases IMEP. As fuel injected was held constant, the ITE decreased approximately linearly with decrease in IMEP. The points where spark

was optimized show almost no penalty in specific fuel consumption. The least fuel-efficient points used approximately 11% more fuel than would be predicted for combustion without water injection.

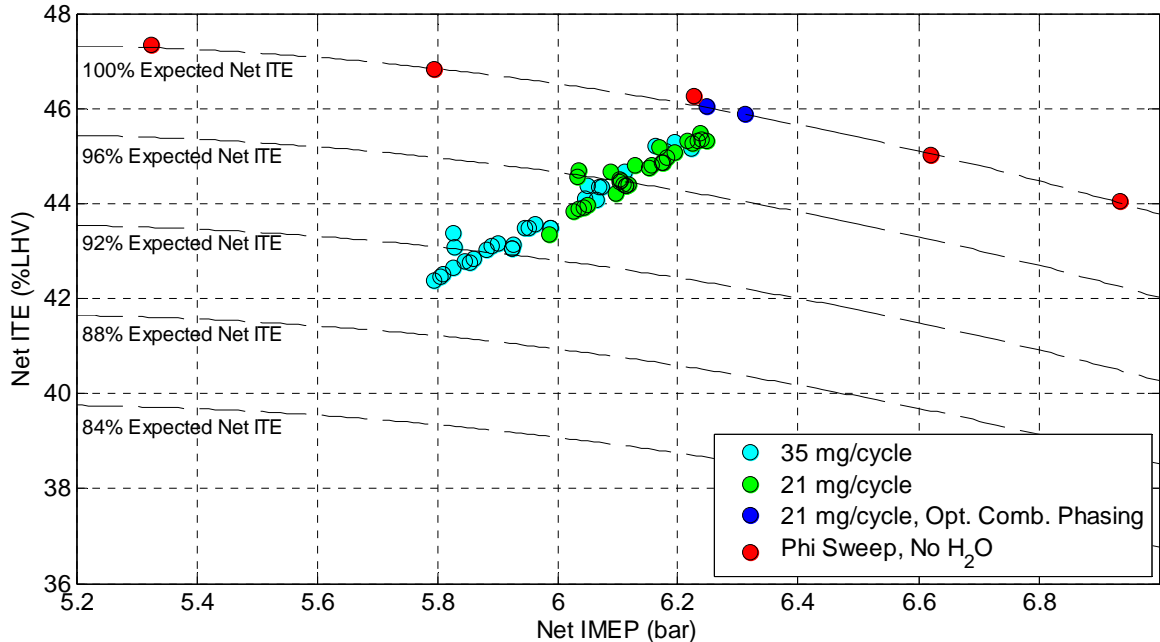


Figure 4.13: Net ISFC as a function of Net IMEP.

Figure 4.14 presents the normalized NO_x (where the NO_x emissions with water injection are normalized to the estimated NO_x emissions if water was not injected using the equivalent IMEP) as a function of normalized fuel consumption (where the ITE with water injection is normalized to the estimated ITE if water was not injected using the equivalent IMEP). Figure 4.15 presents the normalized fuel injection as a function of injection phasing. Figure 4.16 presents NO_x as a function of injection phasing. The conditions with MBT combustion phasing reduced NO_x by 73% and 85% with no increase in fuel usage.

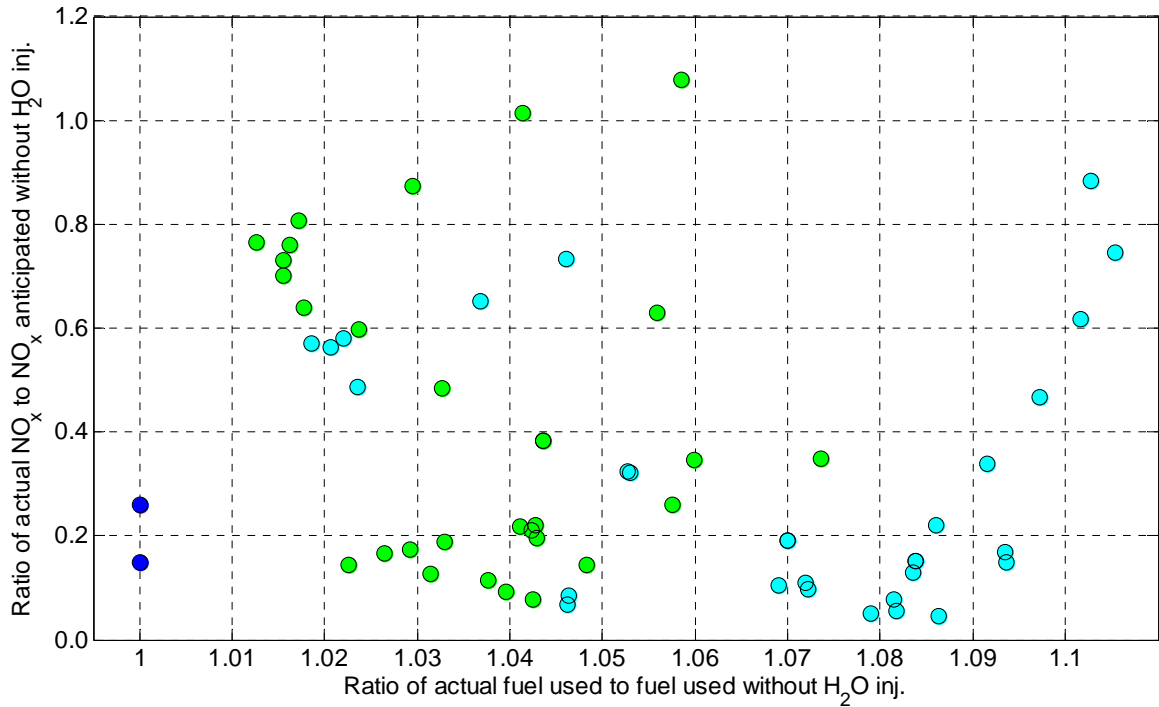


Figure 4.14: Estimated effects of water injection on NO_x and fuel consumption.

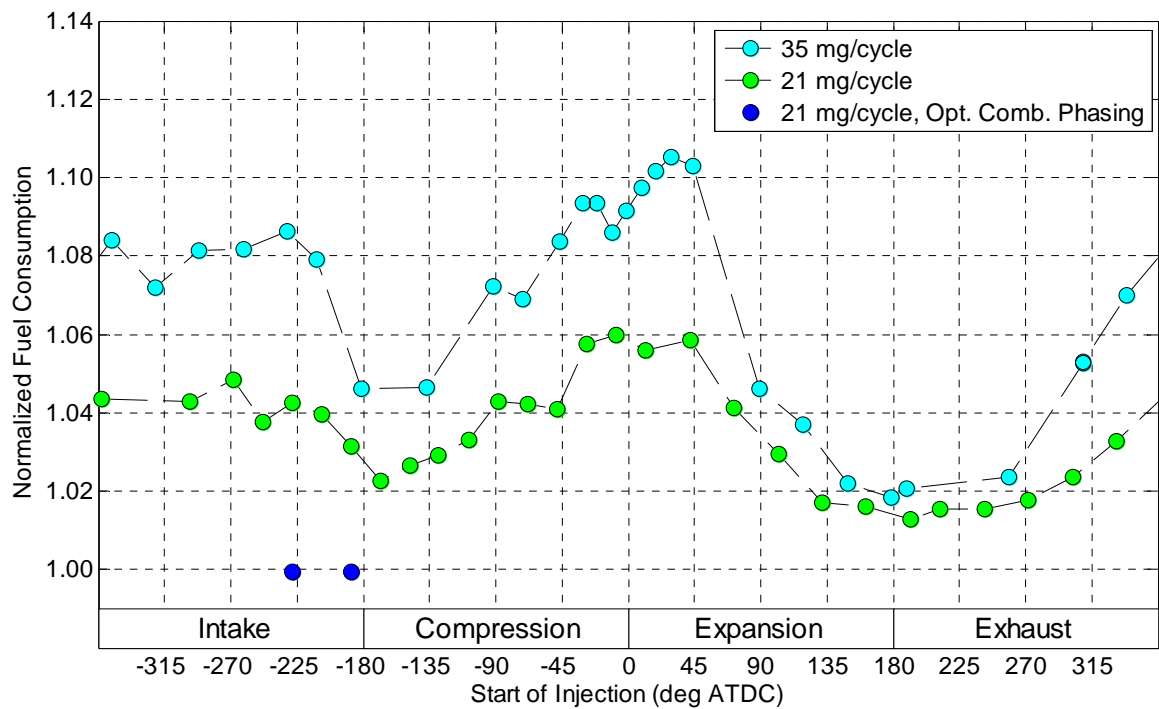


Figure 4.15: Normalized fuel consumption as a function of injection timing.

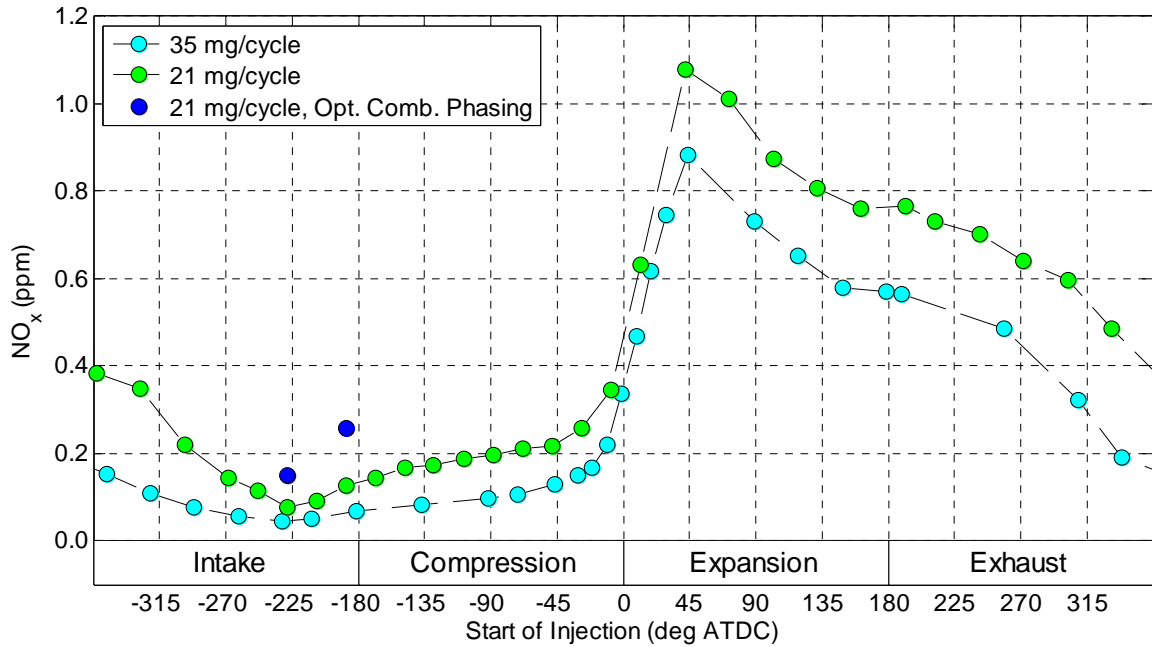


Figure 4.16: Normalized NO_x as a function of injection timing.

Figure 4.17 summarizes the tradeoff between Net IMEP and NO_x production. When water is injected at 21 mg/cycle and MBT timing is used, the load developed slightly exceeds the load seen when $\phi=0.5$ and no water is injected. NO_x production is reduced from 725 ppm to 106 ppm, which equals the NO_x production seen when $\phi=0.4$ and no water is injected. Compared to the baseline $\phi=0.4$ experiment, the water injection improved load developed by 17.3%.

The minimum NO_x production with water, 13 ppm, is approximately the same as would be expected under baseline operation when $\phi=0.33$ and NMEP = 4.6 bar. If the maximum permissible NO_x production were 13 ppm, water injection would improve maximum load by 26.7%.

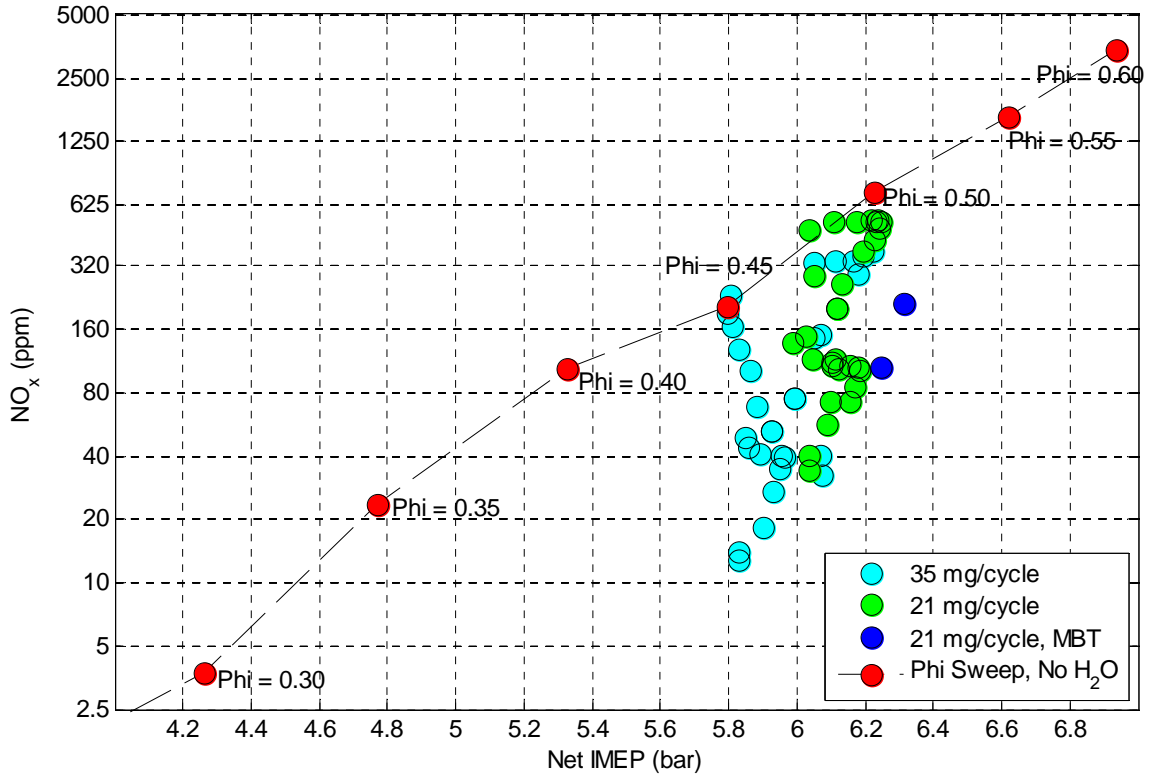


Figure 4.17: NO_x as a function of Net IMEP.

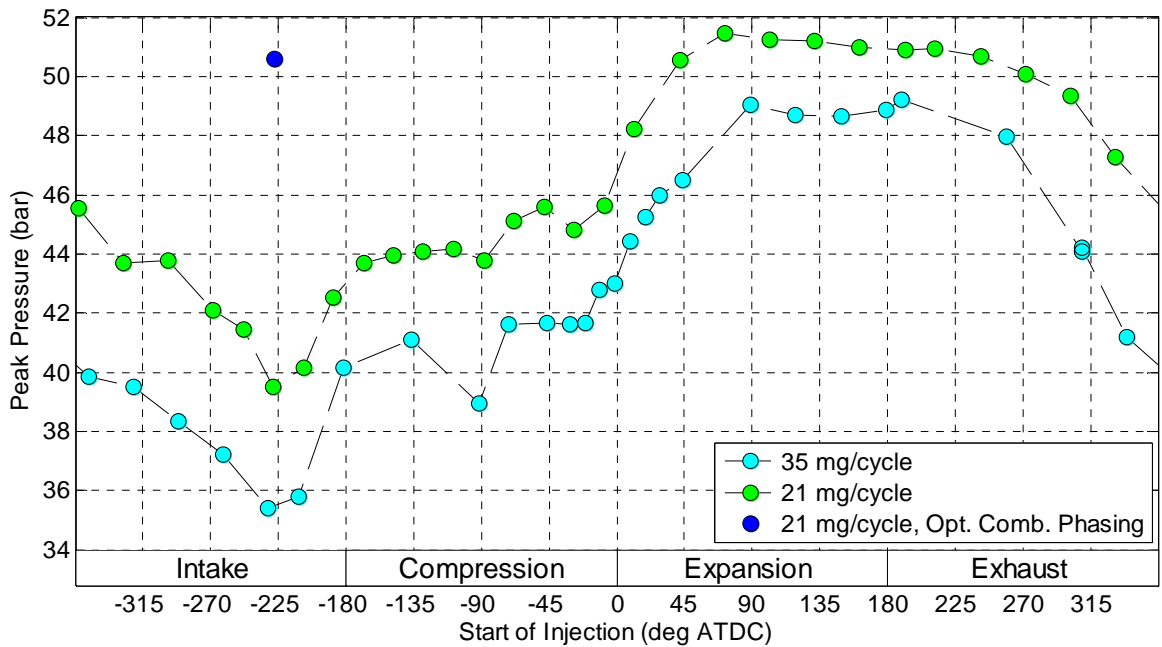


Figure 4.18: Peak pressure as a function of water injection phasing.

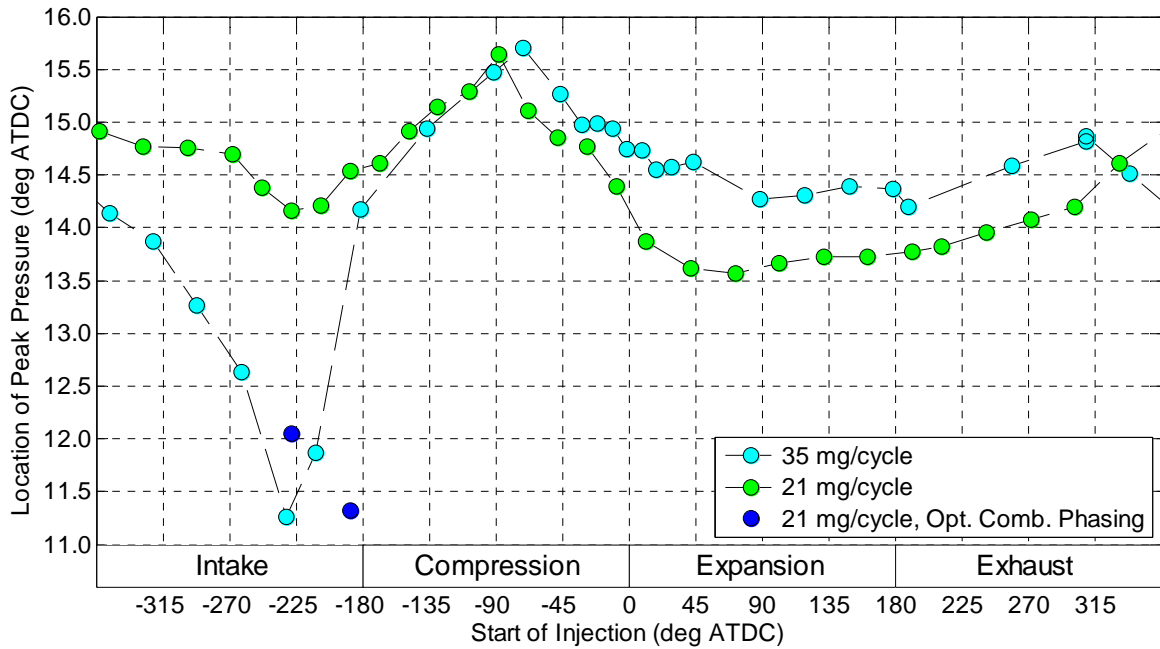


Figure 4.19: Timing of peak pressure (relative to TDC = 0°) as a function of water injection phasing.

Peak cylinder pressure is shown in Figure 4.18, and location of peak pressure is shown in figure 4.19. Figure 4.20 and 4.21 contrasts these same values to those anticipated without water injection. The test points where spark timing is not optimized have peak pressure 2-6 degrees later than expected. When combustion phasing is optimized, the location of peak pressure returns to that anticipated by a standard, no-water-injected case. Optimal combustion phasing also eliminates most of the advantage seen in peak cylinder pressure.

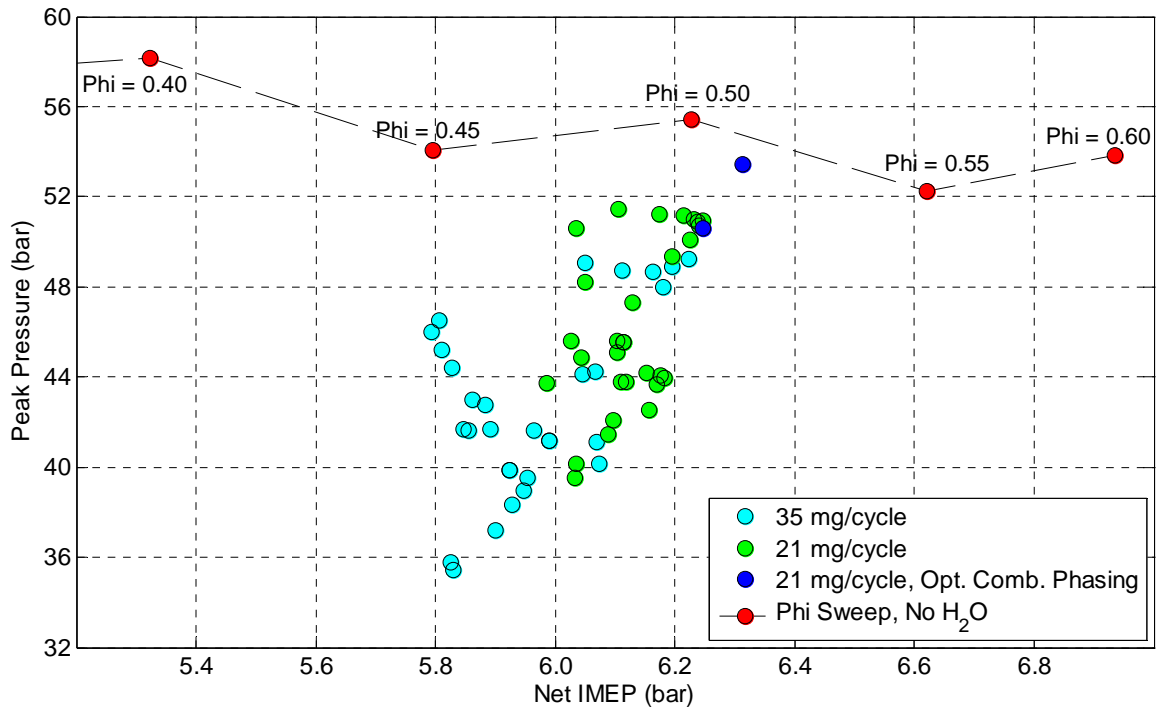


Figure 4.20: Peak pressure as a function of net IMEP.

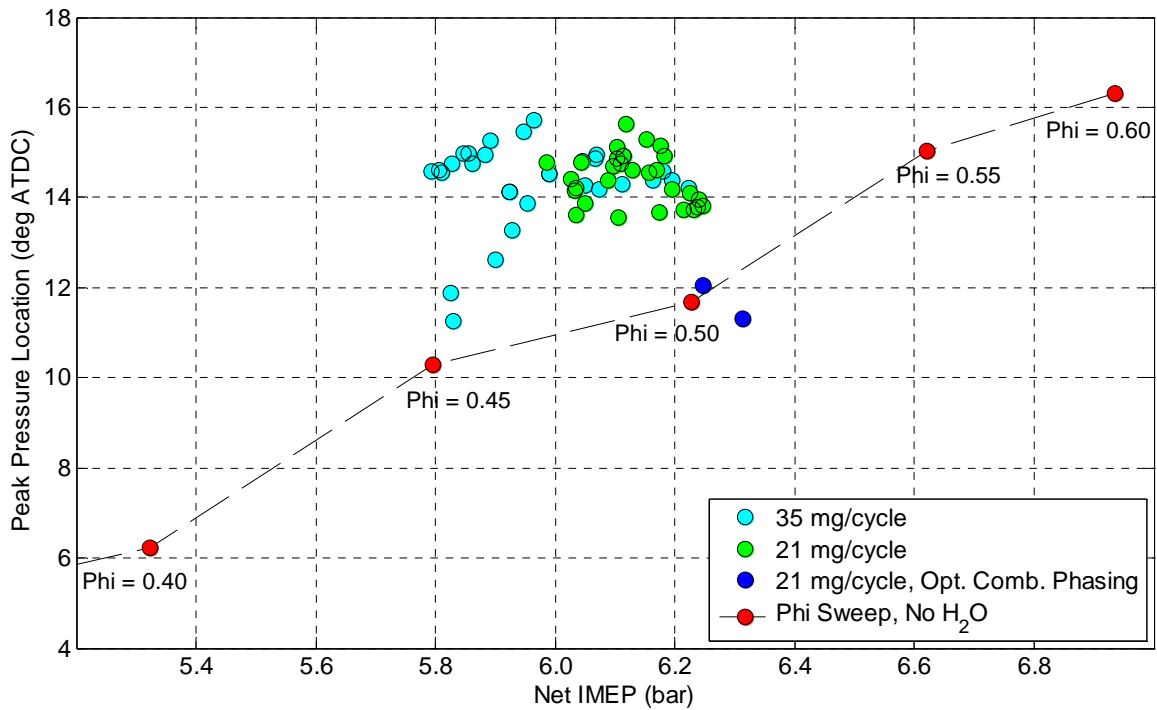


Figure 4.21: Time in CAD of peak pressure as a function of net IMEP.

The advantages of peak cylinder pressure and disadvantages of burn rate are summarized in Figure 4.22 and Figure 4.23. These figures show the pV diagram and cylinder pressure for three conditions: as a function of crank angle for the reference case with no water injection, a water injection case with the same ignition time as the reference case, and the water injection case with re-optimized spark timing. The optimized water injection condition lowers peak pressure, but at the expense of slower burn rates.

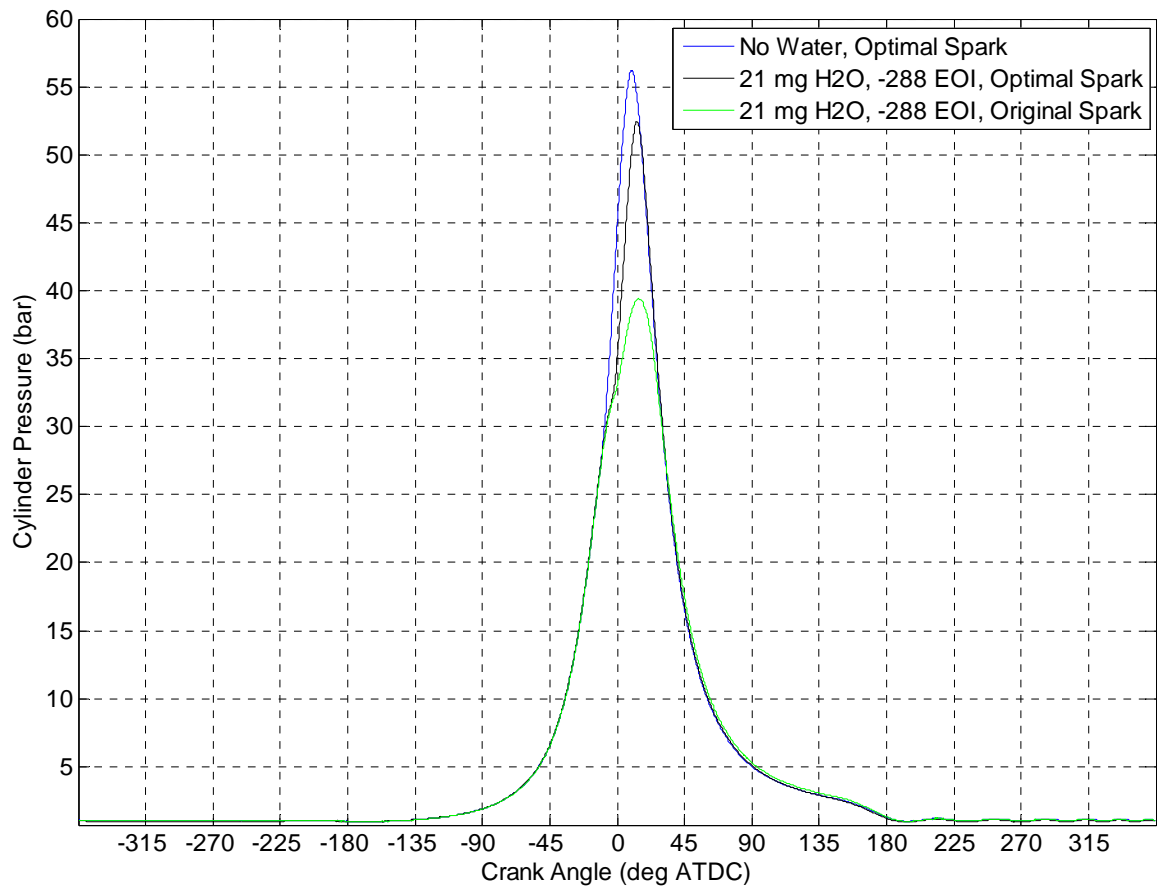


Figure 4.22: Pressure as a function of crank angle.

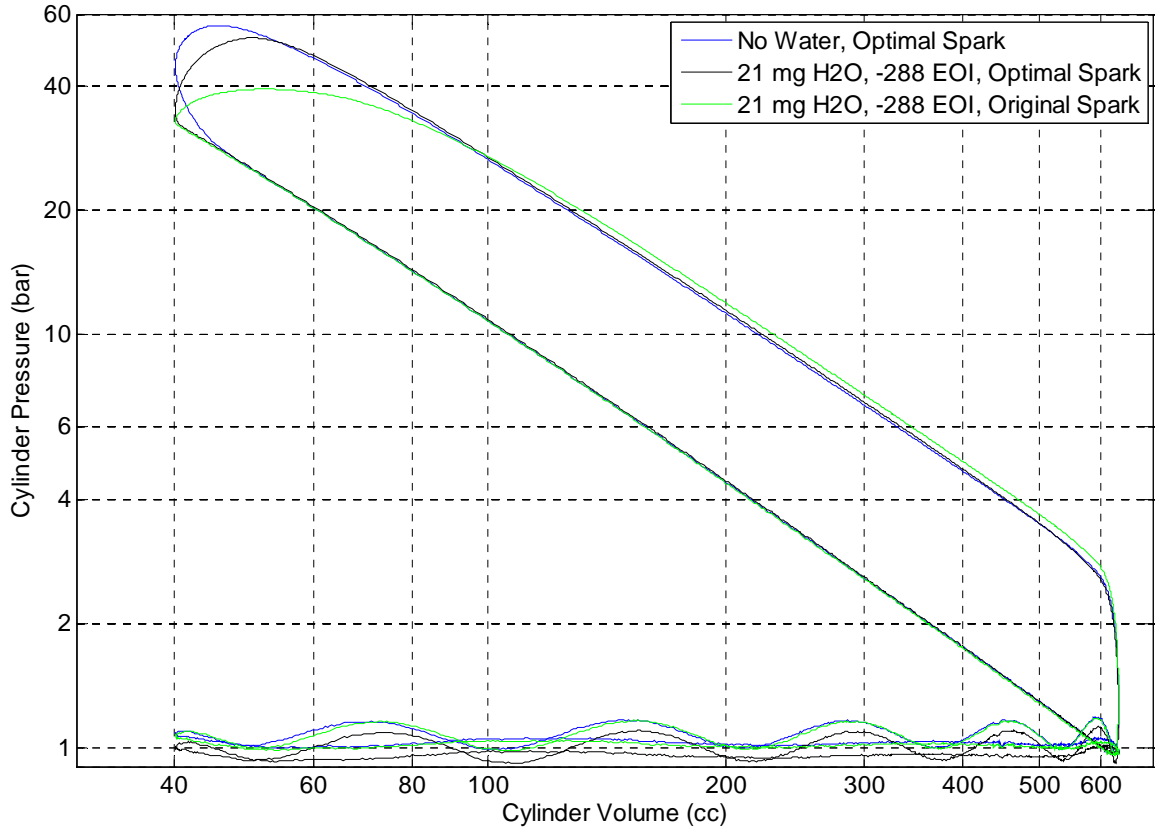


Figure 4.23: pV Diagram.

4.5 Conclusions

Hydrogen engine experiments were conducted using an engine with port fuel injection and direct in-cylinder water injection. The effects on engine performance, including fuel consumption and NO_x emissions were determined. The results were compared to 'baseline' conditions which did not have water injection. The system was effective at reducing NO_x emissions; where 21 mg/cycle water injection reduced NO_x by 93%, and 35 mg/cycle water injection reduced NO_x by 95%, albeit with an increase in fuel consumption of 8%. When operated in a manner that did not reduce fuel consumption, the direct injection of water decreased the NO_x production by 85%. If the maximum NO_x permissible is limited to 106 ppm, water injection would be able to improve

NMEP developed by 17.3%. If the threshold was reduced to 13 ppm, water injection would improve maximum NMEP by 26.7%.

As such, direct water injection can be expected to increase the specific power of emissions-controlled hydrogen engine applications and enable a reduction in engine displacement. The reduction in friction associated with the smaller engine is anticipated to improve system-level fuel efficiency in a normal automotive drive cycle.

Chapter 5

Water Injection into the Intake Port of a DI Hydrogen Engine

5.1 Introduction

In Chapter 4 the justifications and purposes for testing water injection were introduced. Water injection, when combined with hydrogen combustion, can allow operation at higher equivalence ratios, which in turn can allow engine downsizing and an associated benefit in engine friction. Chapter 4 introduced experiments done on a PI hydrogen engine with DI water injection. Although the results were promising, fueling via PI has several drawbacks when compared to DI fueled engines. Among the disadvantages is a greater possibility of aberrant combustion, increased fuel consumption at a given load, and lower peak load. DI operation eliminates the possibility of pre-intake-valve-closing (IVC) autoignition, and the short mixing time often drastically decreases the possibility of post-IVC autoignition as well. Further, by injecting fuel directly in the chamber, fuel temperature at top dead center (TDC) can be controlled, controlling NO_x emissions. Optimizing the injection timing also allows for a degree of fuel distribution control, which in turn allows DI engines to reach higher loads than PI engines. The drawbacks to DI operation include economic considerations and injector durability concerns. The many advantages of DI operation motivate the study of water injection to further improve DI hydrogen engines. Specifically, the work in this chapter evaluates PI water injection combined with DI fuel injection.

5.2 Experimental Approach

For this study, water was injected into the intake port and hydrogen fuel was injected directly into the combustion chamber. Some details of the hardware used are shown in Table 5.1.

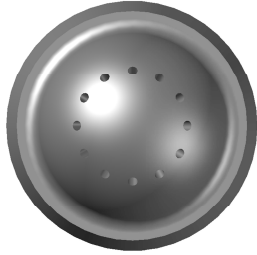


Cylinder Head: Gen III	Fuel Injector	Piston	Water Injector
			No Picture Taken
Central Ignition/Central Injection Cylinder Head	Westport 12H 40 deg Inj; 110 bar operating pressure	11.7:1 Domed Piston (modified 10.4:1)	Gasoline 6H Bosch Injector, 40 PSI operating pressure

Table 5.1: Engine and fuel injector hardware used in DI water injection studies.

The choice of a representative equivalence ratio for an automotive engine depends on the fueling strategy. The advantages inherent to DI hydrogen operation allow for higher equivalence ratios to be used during normal operation. One potential strategy that is quite promising is to split the fuel charge into multiple injection pulses. One or more of the pulses would likely occur after ignition, which allows for combustion well after TDC and correspondingly, lower peak temperatures and lower NO_x for a given equivalence ratio/load. Of course, this strategy reduces the effective expansion ratio of the fuel injected after ignition, thus, specific fuel consumption is increased. Nevertheless, the increase in maximum load that can be developed makes this tradeoff worthwhile.

A typical graph of this NO_x/fuel consumption tradeoff is shown in Figure 5.1 for $\phi = 0.6$ conditions. As seen in Figure 5.1, even a split injection strategy results in several hundred ppm of NO_x. In most automotive applications, this level of NO_x would not be permissible. In order to evaluate the ability of water

injection to improve the maximum load possible with DI H₂, all points for this study were conducted at $\phi = 0.6$. For each test, the engine was operated at a constant speed of 1500 RPM. Manifold pressure for all data was 100 kPa.

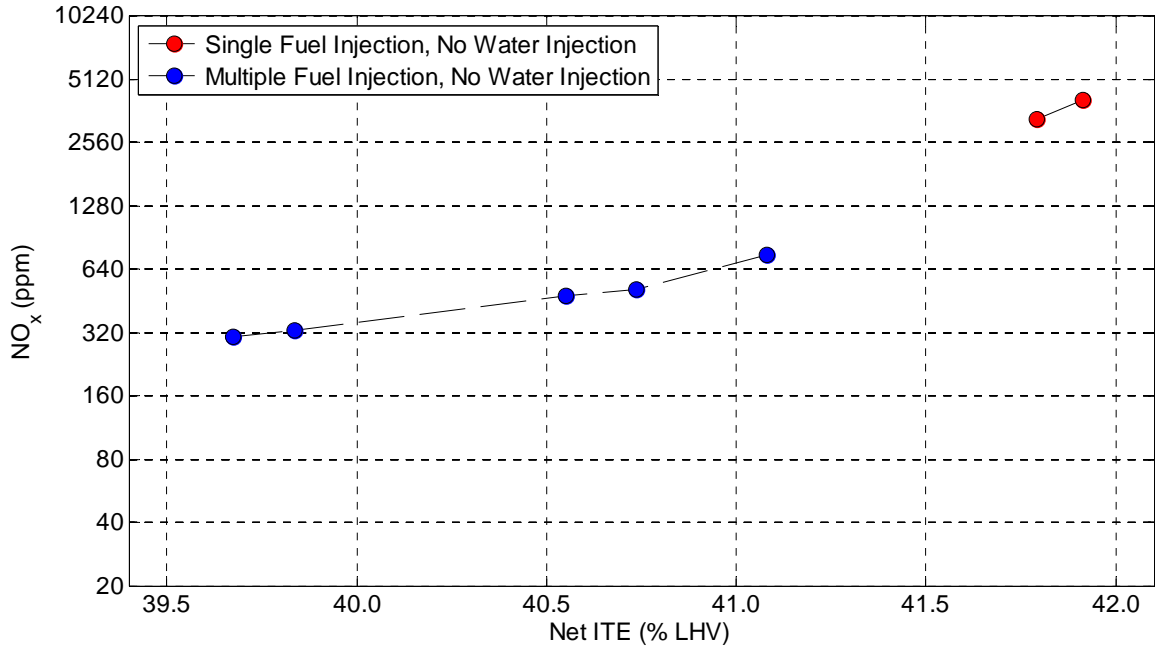


Figure 5.1: Tradeoff between NO_x and ISFC for $\phi = 0.6$ single and split injection strategies.

As in the PI water injection study, the calculations of combustion characteristics do not take into account the introduction of water into the system. Given the water is introduced with the intake air charge, and the amount of water is a low percentage of the intake charge, this error is expected to be minor. Relative differences will hold true regardless of the small absolute error.

Both water injection parameters and fuel injection parameters can have a substantial effect on the performance of the engine. The amount of water injected can vary. The fuel injected into the cylinder can be split into two or more pulses; each adding two degrees of freedom – phasing of the pulse and amount of fuel in the pulse. A summary of the mechanisms used to control

engine performance and NO_x production is shown in Table 5.2. In total, there were five mechanisms through which fuel consumption, NO_x emissions, and engine performance in general were optimized.

		Low Limit	High Limit	Unit
1	Spark Timing	MBT-7	MBT+3	deg BTDC
2	Total Water Injected	0	81	mg/inj
3	EOI of initial H ₂ Injection	55	70	deg BTDC
4	EOI of second H ₂ Injection	0	10	deg ATDC
5	Percent of fuel in first injection	70	100	%

Table 5.2: Water injection parameters studied.

5.3 Experimental Results: Fuel Consumption and NO_x Emissions

Figure 5.2 presents the NO_x and indicated specific fuel consumption (ISFC) results of the PI water injection experiments. As can be seen, the baseline point is aggressive in terms of total NO_x to be reduced (with several thousand ppm of NO_x). This is expected with the high equivalence ratio tested. At every fuel injection condition, there are several points shown, because the spark timing was varied to allow another degree of freedom in the tests. Several conditions allow over 2 orders of magnitude reduction in the NO_x emissions compared to the baseline.

In Figure 5.3, a subset of the PI water injection data have been filtered to include only the most fuel efficient conditions for a given NO_x level. The tests were conducted at 27 mg/cycle, 54 mg/cycle, and 81 mg/cycle of water. It can quickly be seen that, at equivalent NO_x, using a single fuel charge resulted in improved fuel consumption when compared to splitting the fuel injection into two charges. The minimum level of NO_x seen, approximately 30 ppm, could be expected to achieve emissions compliance depending on vehicle level

assumptions.

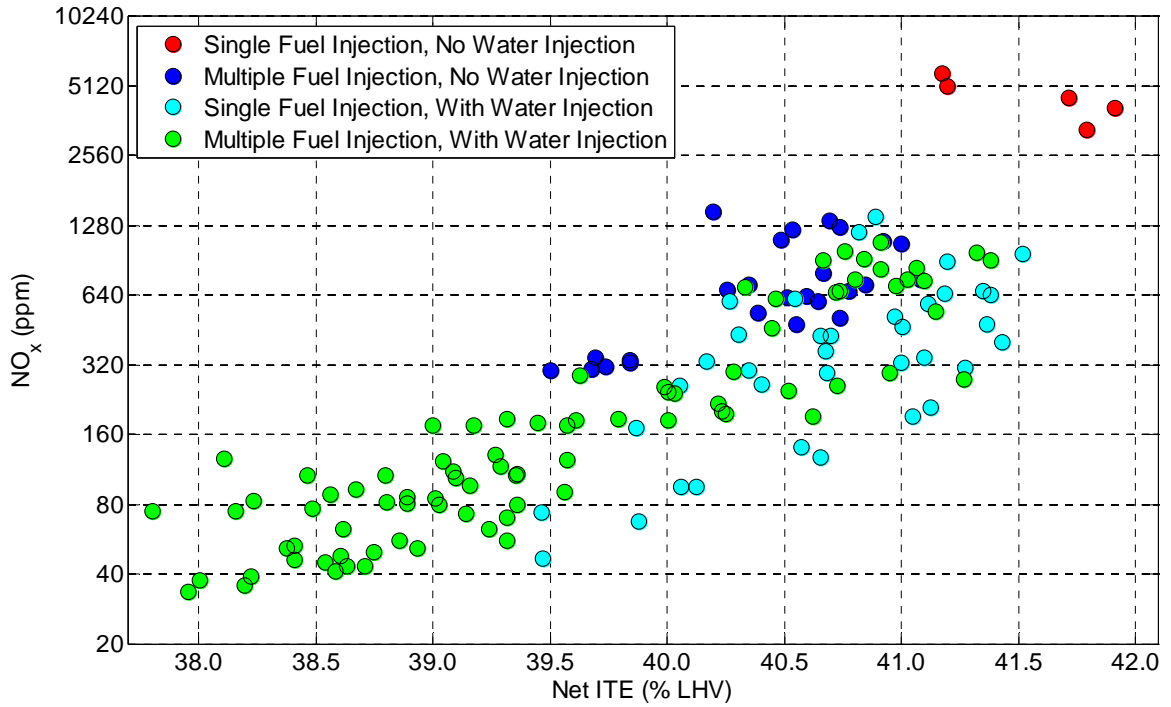


Figure 5.2: NO_x as a function of ISFC for PI water injection and DI H₂ injection.

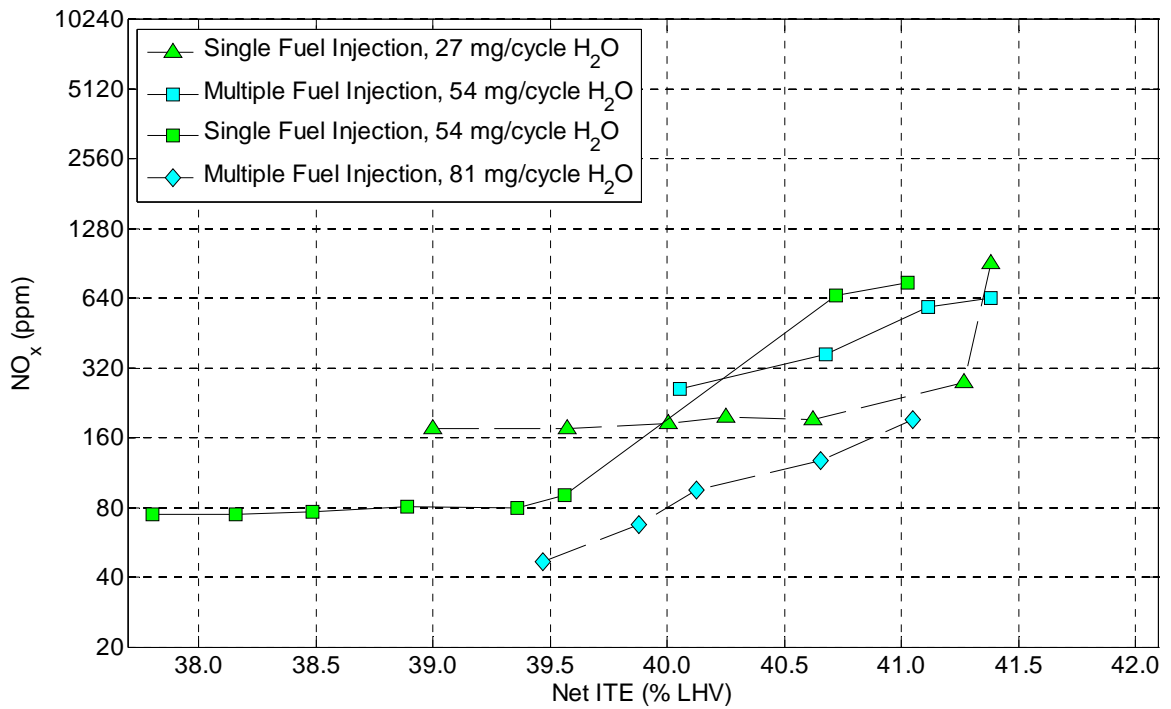


Figure 5.3: NO_x as a function of ISFC, fixed injection time.

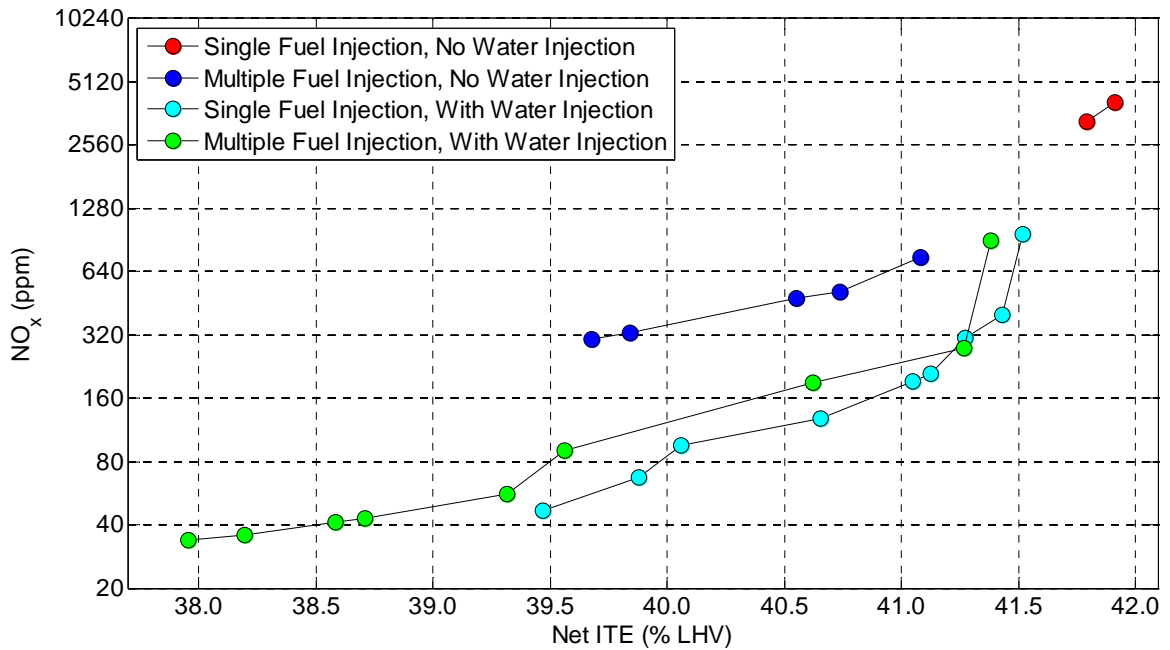


Figure 5.4: Tradeoff between NO_x and ISFC, summary of best points among all points tested.

In Figure 5.4 the data are sorted into four groups:

- single (baseline) injection without water injection
- multiple injection without water injection
- single injection with water injection
- multiple injection with water injection

All four groups were sorted and downselected to only show the lowest fuel consumption for a given amount of NO_x. As can be seen, a single-pulse injection with no additional water has the best efficiency but produces 4500 ppm of NO_x. If lower NO_x is required, then single charge fuel injection with H₂O produces the most efficient operating strategy for the entire range in which it was tested. This strategy reduces NO_x by approximately 75% compared to a multiple injection strategy without water injection.

Figure 5.5 shows the tradeoff between NO_x and Net IMEP. If the maximum permissible NO_x emissions are limited to 90 ppm, the maximum load developed with water injection possible is 7.92 bar, an increase of 23.9% over the maximum possible without water injection.

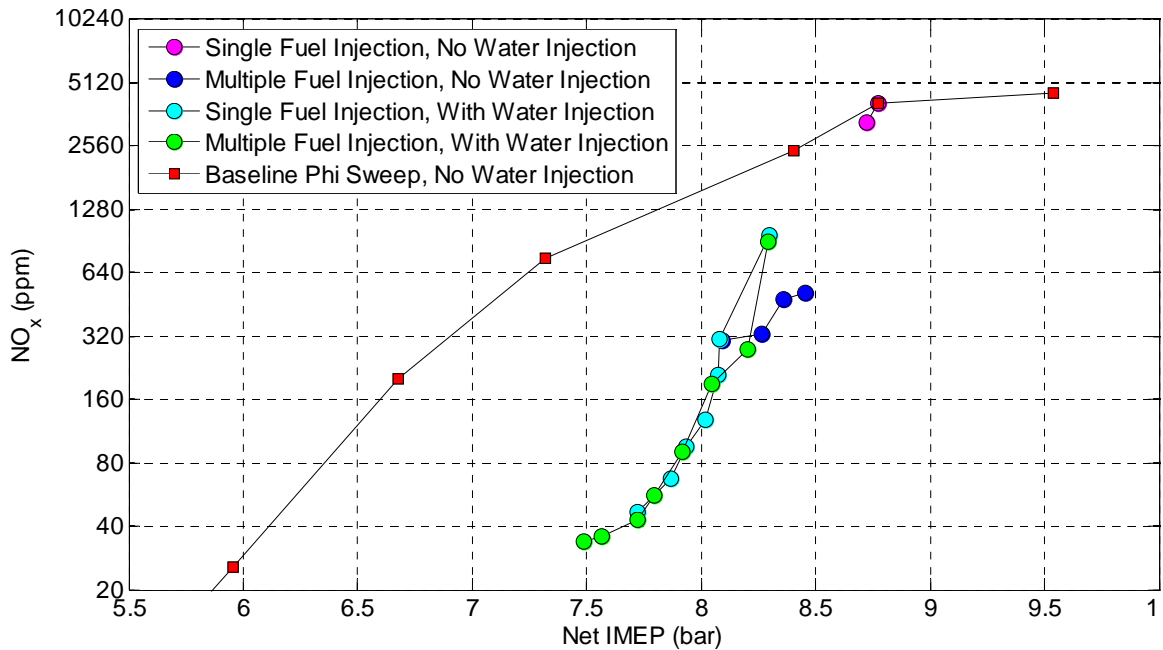


Figure 5.5: Tradeoff between NO_x and Net IMEP, summary of best points among all points tested.

5.4 Analysis of Fuel Consumption/NO_x/IMEP Compromise

Unfortunately, the addition of water to the intake charge decreases the engine output slightly. Of course, the other primary methods of decreasing NO_x, such as multiple injection strategies and lower equivalence ratios, also decrease engine output. As shown in Chapter 4, NO_x correlates well with IMEP when an exponential fit is used and the fitting coefficients are optimized to minimize error. The best-fit equation for the H₂ DI data was:

$$NO_x = A \cdot e^{B \cdot IMEP} \quad \text{Equation 5.1}$$

Error was minimized when A was set to 0.166 and B was set to 1.145. These values resulted in an R^2 value of 0.996. Using this NO_x/IMEP correlation, any IMEP can be compared to an expected value.

Figure 5.6 compares some of the strategies possible to the baseline case of single injection with variable equivalence ratio using the NO_x/IMEP correlation. The spark strategies decreased NO_x by 21%. The multiple injection strategies reduced NO_x production by 85%. Single injection with water injection reduced NO_x production by 96%, and split injection combined with water injection reduced NO_x production by close to 97%.

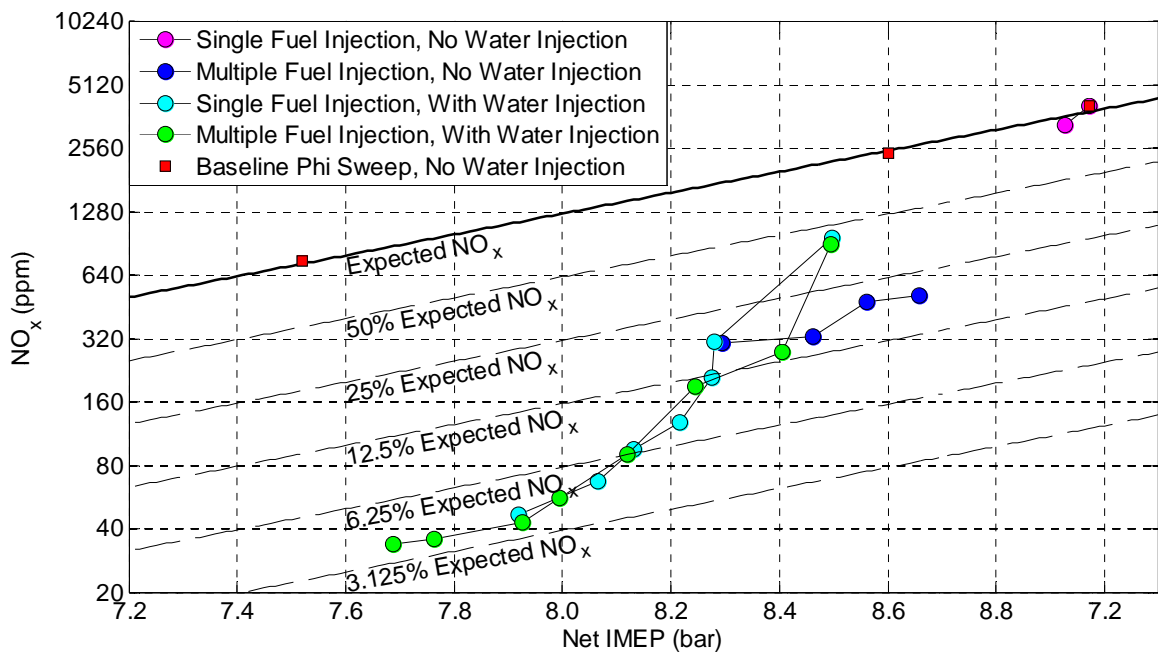


Figure 5.6: Comparison of NO_x production as a function of IMEP for water injection and baseline (no water injection) conditions.

The H_2 DI fuel consumption data are correlated with IMEP as well, yielding the following best-fit expression:

$$ITE = A \cdot \text{IMEP}^2 + B \cdot \text{IMEP} + C \quad \text{Equation 5.2}$$

Error was minimized when A was set to -0.127, B was set to 1.234, and C was set to 40.84. These values resulted in an R^2 value of 0.99. The effects of PI water injection on ISFC are shown in Figure 5.6. As is expected, the strategies used to mitigate NO_x have a corresponding penalty in fuel consumption. In the cases tested, the penalty varied between 2% and 12%.

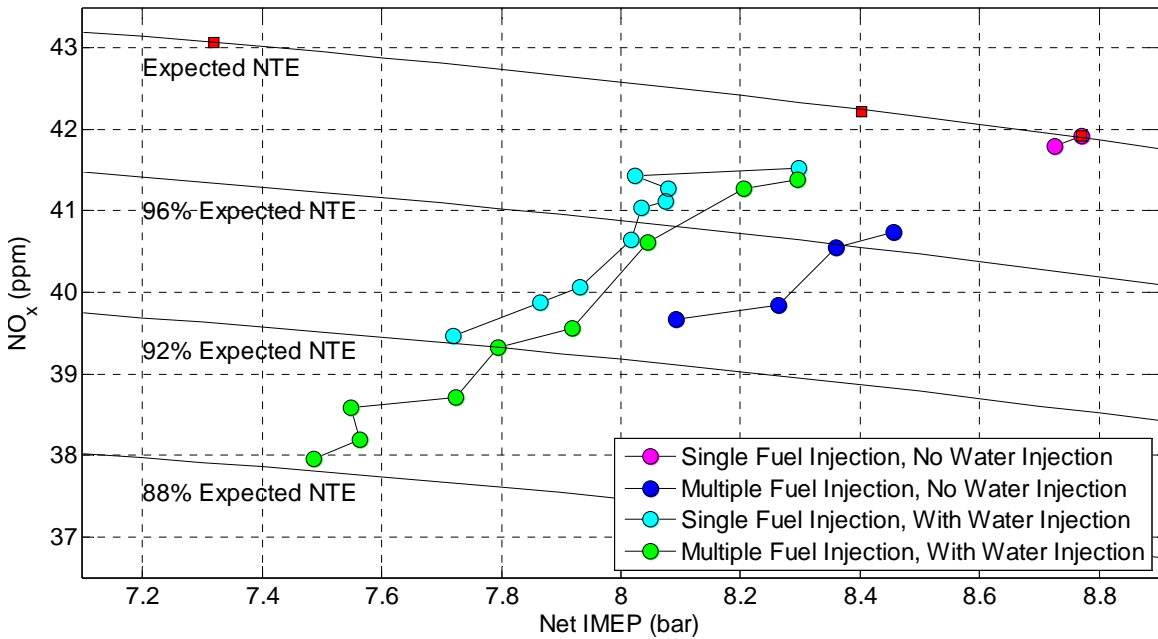


Figure 5.7: Comparison of ISFC as a function of IMEP for water injection and baseline (no water injection) conditions.

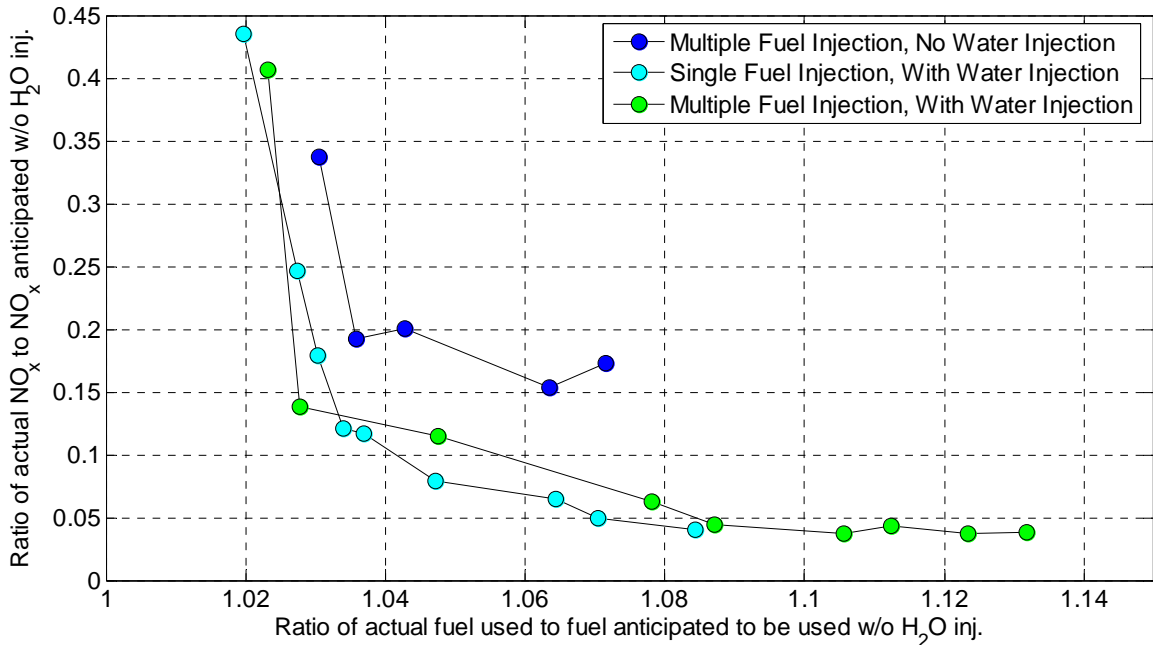


Figure 5.8: Normalized NO_x mitigation as a function of fuel consumption penalty.

The tradeoff between fuel consumption and NO_x is presented in Figure 5.8. The three strategies all reduce NO_x substantially. With a 2% fuel consumption penalty, the split fuel-injection case without water injection decreases NO_x by 68%. Single fuel injection with water injection decreases NO_x by 83%, and split injection combined with single injection reduces NO_x by 87%. When the fuel consumption penalty is 10%, NO_x production is reduced by over 96%.

The NO_x mitigation methods also reduce the peak cylinder pressure, which is shown in Figure 5.9. All NO_x mitigation strategies reduce peak cylinder loads by at least 5 bar, and in some cases cylinder pressures are reduced by 30 bar.

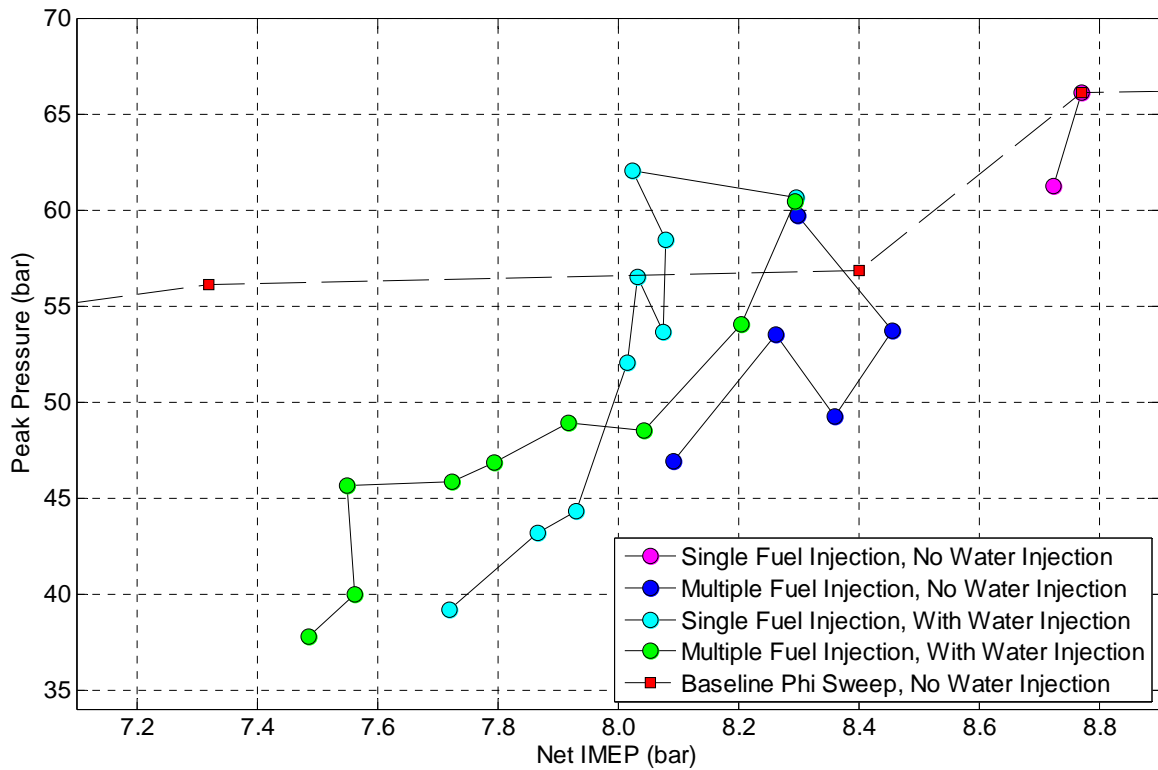


Figure 5.9: Peak pressure as a function of IMEP.

Figure 5.10 shows the extent to which water injection reduces peak pressure rise rate. The conditions with minimal increase in fuel consumption show no reduction in peak pressure rise rate. The conditions with a 12% increase in fuel consumption decrease the peak pressure rise rate from 2.2 bar/deg to 0.8 bar/deg.

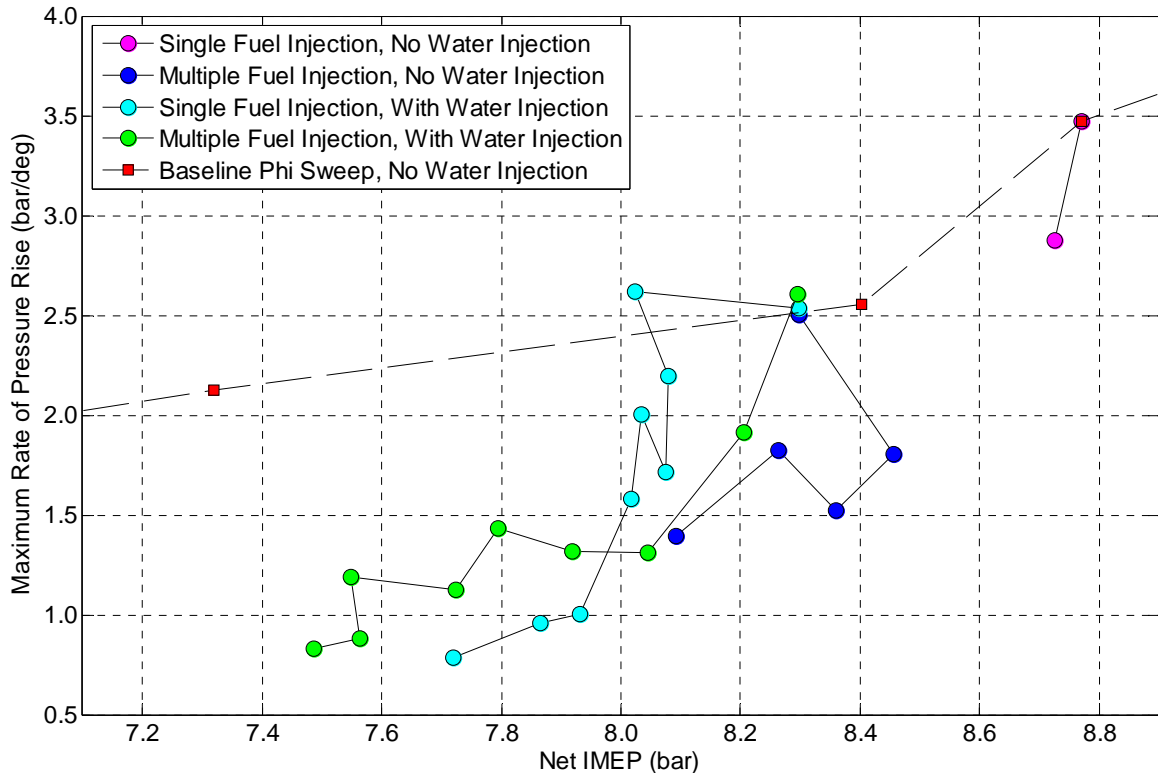


Figure 5.10: Maximum pressure rise rate as a function of IMEP.

5.5 Conclusions

Intake port water injection was investigated as a means to decrease NO_x emissions from an H₂ engine with direct in-cylinder fuel injection. The experiments considered an equivalence ratio of 0.6. The results were compared to baseline conditions which did not use water injection. The water injection strategy was demonstrated as effective at reducing NO_x emissions. An 87% reduction in NO_x emissions was achieved with only a 2% fuel consumption penalty. The comparable NO_x mitigation strategy of multiple injections was less advantageous, only achieving a 68% reduction in NO_x emissions. The minimum NO_x achieved with water injection was roughly 30 ppm, albeit with a 12% increase in fuel consumption. As this condition is anticipated to be the peak load of the engine, it is reasonable to assume this condition could be used in a drive

cycle that complies with emissions regulations. In contrast, the multiple injection strategies tested were not able to reduce NO_x below 125 ppm.

A strategy including water injection can be expected to increase the specific power of emissions-controlled applications. At a threshold emissions level of 90 ppm of NO_x, water injection is able to increase Net IMEP by 23.9%. The addition of water injection, in an appropriately downsized engine, is expected to reduce fuel consumption in a normal automotive drive cycle.

Chapter 6

Dual Zone Combustion System: Metal Engine

Experimental Results

6.1 Introduction

Although the efficiencies of combustion systems tested to this point have been promising, the high fuel costs of operating an engine on hydrogen warrant attempts to reduce the combustion and heat transfer losses further. It was hypothesized that using two ignition sites, on the side of the chamber, would help reduce the losses due to combustion delay. Furthermore, a dedicated injector, designed to direct fuel towards the spark plugs while entraining air, was designed and tested.

6.2 Experimental Setup

All tests were conducted on the single cylinder engine at Ford Motor Company discussed in Chapter 2. The cylinder heads used for these experiments are shown again in Table 6.1, and the injectors chosen for this study are shown in Table 6.2. The 5H injector was chosen because it had shown superior efficiency to all other injectors tested to date.


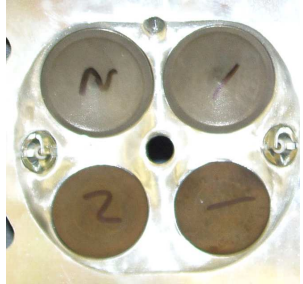
		
Name	Single Central Ignition Head	Dual Side Ignition Head
Injector Location	Central	Central
Spark Plug Location	Central	Dual Side
Designer	"Production"	Younkins/Boyer

Table 6.1: Cylinder heads and injectors tested.

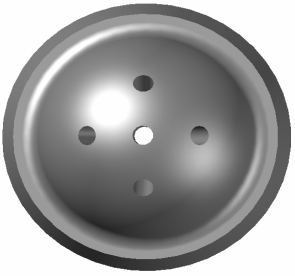

		
Pattern	5H	3+3
Spray Angle	0/35	45/70
Nozzle Diameter (mm)	0.597	0.545
Nozzle Area (mm ²)	0.280	0.233
Total Flow Area (mm ²)	1.4	1.4

Table 6.2: Fuel injector nozzle designs tested.

Although many tests were conducted using this hardware (detailed in Appendix A) the results shown here were conducted at $\phi = 0.4$. The injection timing was varied to determine the manner in which the fuel distribution and mixing time affected the performance of the engine.

6.3 Experimental Results and Discussion

6.3.1 Comparison of 5H and 3+3H Injectors operated with central ignition and dual-side-ignition spark plugs for fixed engine speed

Figure 6.1 compares the fuel consumption and NO_x production of the four cylinder head and injector configurations.

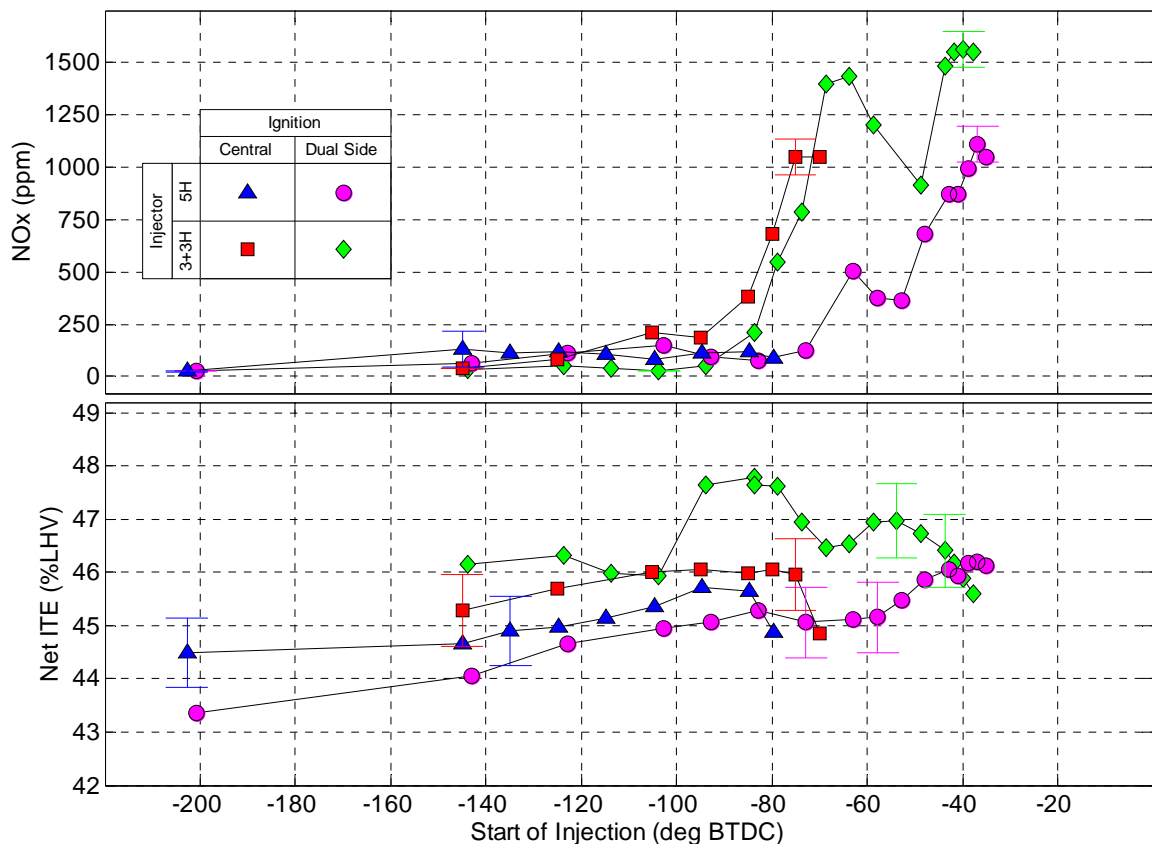


Figure 6.1: Indicated specific fuel consumption and NO_x emissions as a function of SOI.

At the conditions tested:

- ▲ When the baseline 5H injector was paired with the baseline Gen III central ignition cylinder head, the best thermal efficiency observed was 45.7% at an SOI timing of 95 degrees.
 - ▲ The NO_x production at that condition was 115 ppm.
 - ▲ More mixing time (yielding presumably more homogenous combustion conditions) decreased NO_x, but decreased efficiency.
 - ▲ When injection timing was advanced past 80 degrees, combustion stability suffered, specific fuel consumption increased, and data were not taken.
-
- When the 3+3H injector was paired with the baseline central ignition cylinder head, efficiency increased to 46.1% at an SOI timing of 95 degrees.
 - The NO_x production at that condition was 190 ppm.
 - The range of stable combustion was increased; data were taken until SOI reached 70 degrees BTDC.
-
- When the 5H injector was paired with the new dual-side-ignition head, the efficiency increased to 46.2% at an SOI timing of 37 degrees.
 - However, at this highly stratified condition there was a substantial NO_x penalty, exceeding 1100 ppm.
 - Stability immediately improved at all points and data were taken until the SOI timing reached 35 degrees BTDC.

- Throughout most of the injection timings, the thermal efficiency decreased slightly to consumption increased slightly when compared to either of the previous two cases.
- ◆ When the 3+3 injector was paired with the dual plug cylinder head, efficiency improved to 47.8 at 83 degrees SOI.
- ◆ The NO_x production at this condition was 208 ppm.
- ◆ Increasing the mixing time slightly to 94 degrees decreased efficiency to 47.7% but also decreased NO_x to 52 ppm.
- ◆ Decreasing mixing time further decreased efficiency until a local maximum was found at 70-64 degrees BTDC. This NO_x was found to have local maxima.
- ◆ Decreasing mixing time to 60-50 degrees BTDC resulted in local minima of NO_x and local maxima of efficiency.
- ◆ Mixing times below 50 degrees reduced efficiency and increased NO_x production.

Figure 6.2 plots the NO_x emissions as a function of fuel consumption for the data of Figure 6.1. When compared to the baseline central-ignition/5H pairing, the dual-side-ignition/5H and central-ignition/3+3H pairings made minor improvements in fuel consumption with substantial NO_x penalties. When the 3+3H was paired with the dual-side-ignition head, improvements were made in both fuel consumption and NO_x simultaneously. For example, at 47.7% ITE, only 51 ppm of NO_x was produced.

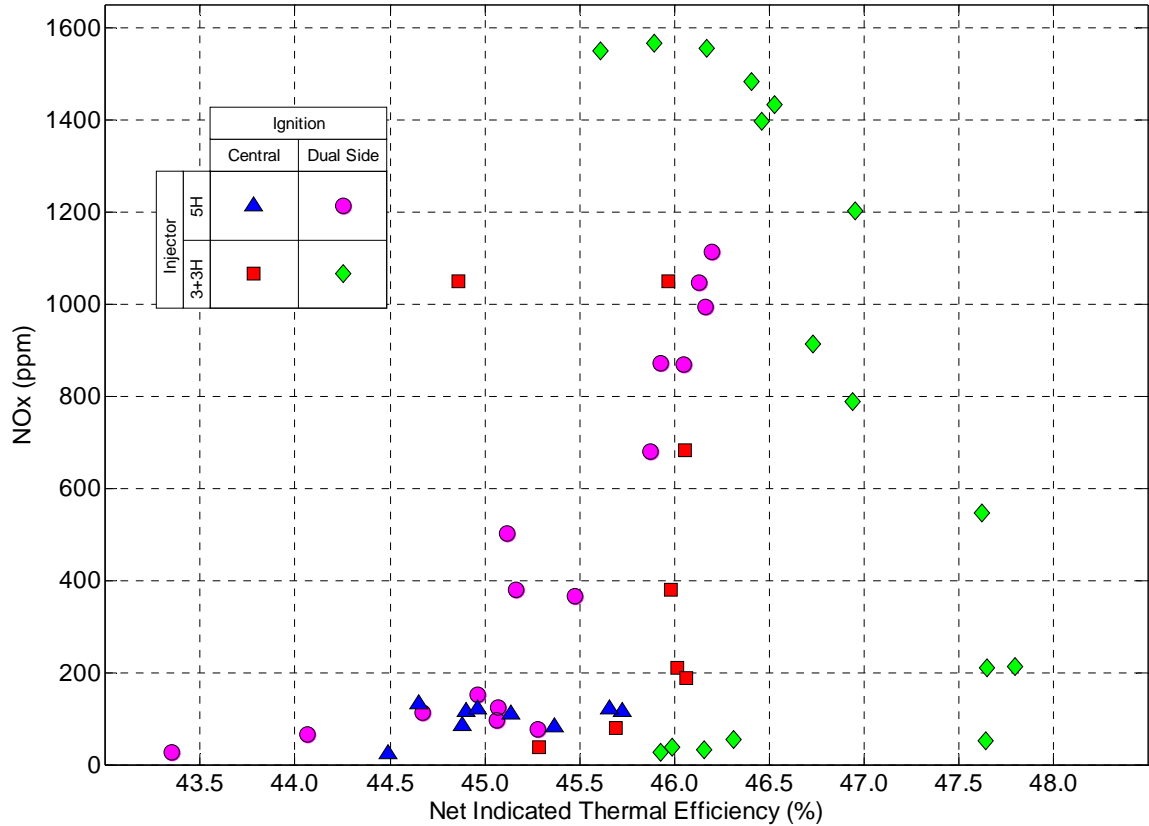


Figure 6.2: NO_x production as a function of fuel consumption for the different cylinder head and fuel injector combinations.

In Figures 6.3 and 6.4, data for the crank-angle duration of 10 to 90% burn and 0 to 10% burn are shown. The central ignition with 5H injector combusted slowly, taking 40-47 degrees to burn 10 to 90% of fuel. The burn rate improved somewhat with the central ignition/3+3H injector, with burn duration taking between 38 and 41 degrees. The improvement was more dramatic when either fuel injector was paired with the dual-side-ignition cylinder head. In particular, the dual-side-ignition/3+3H with late injection timing reduced 10-90% burn duration to 8 degrees. Over the entire range of operating conditions, the 3+3H 10-90% burn rate results were equivalent or improved when compared to the 5H results.

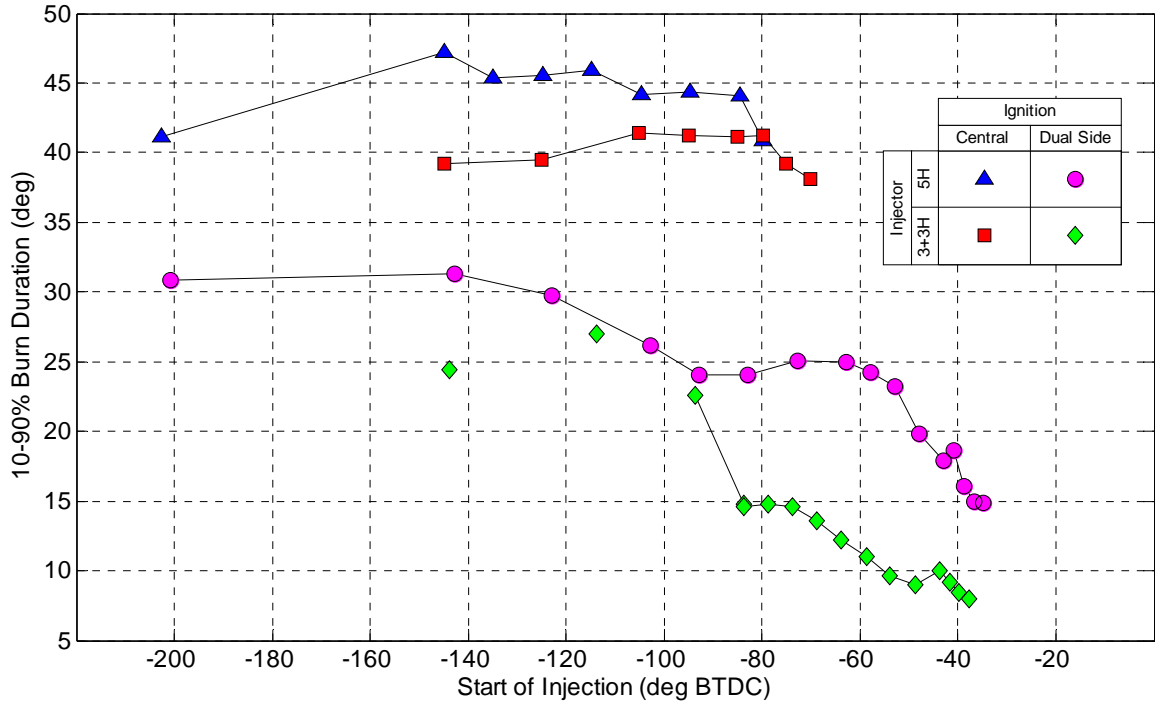


Figure 6.3: 10-90% burn duration as a function of end of injection timing for the different cylinder head and fuel injector combinations.

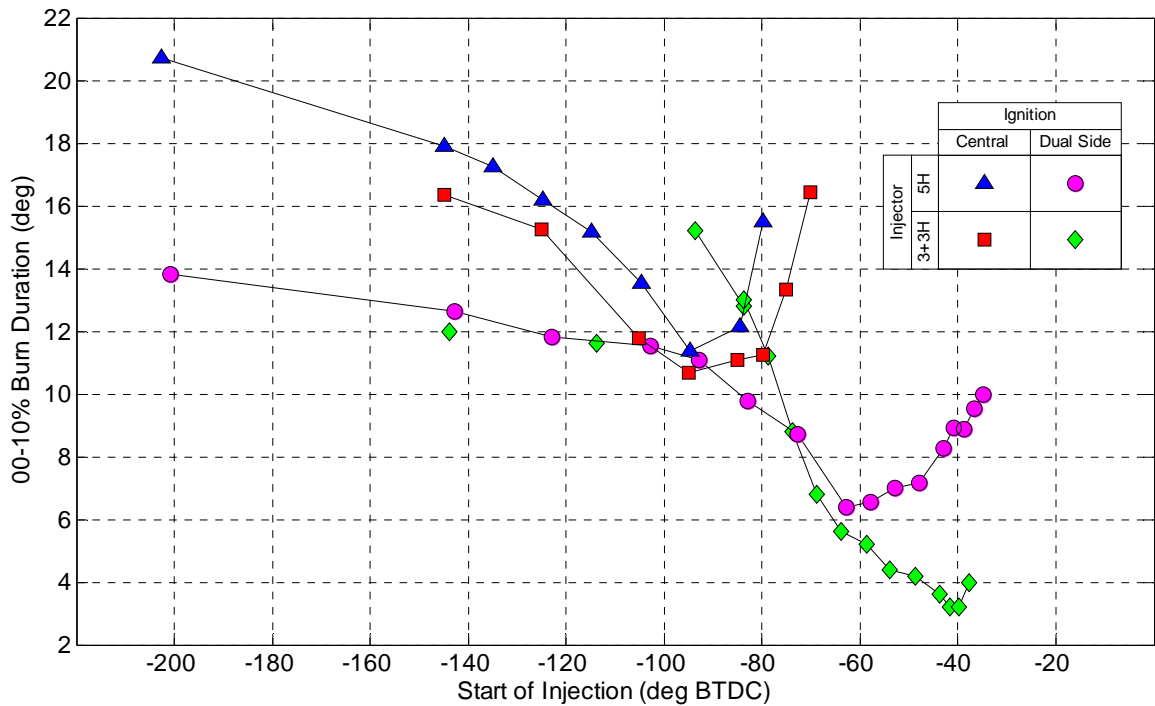


Figure 6.4: 0-10% burn duration as a function of end of injection timing for the different cylinder head and fuel injector combinations.